

# MSC OF INDUSTRIAL ENGINEERING MSC OF SMART INDUSTRY

#### **MASTER'S THESIS**

# SENSOR DESIGN FOR CHARACTERIZATION OF METALLIC NANOPARTICLES

Author: Álvaro Martín Martín

**Supervisors:** 

Romano Giannetti

Francisco Javier Herraiz Martínez

Madrid July 2025 Declaro, bajo mi responsabilidad, que el Proyecto presentado con el título ....SENSOR DESIGN FOR CHARACTERIZATION

OF METALLIC NANOPARTICLES... en la ETS de Ingeniería - ICAI de la Universidad Pontificia Comillas en el

curso académico ...2024/25. es de mi autoría, original e inédito y

no ha sido presentado con anterioridad a otros efectos. El Proyecto no es plagio de otro, ni total ni parcialmente y la información que ha sido tomada

de otros documentos está debidamente referenciada.

Fdo.: Álvaro Martín Martín

Fecha: 14/07/2025

Signed by MARTIN MARTIN ALVARO - \*\*\*2369\*\* on 14/07/2075 with a a P Usuarios certificat

Autorizada la entrega del proyecto

LOS DIRECTORES DEL PROYECTO

Fdo.: Romano Giannetti Fecha: ..15./ .07./ 2025

Firmado por GIANNETTI ROMANO \*\*\*\*3425\* el día 15/07/2025 con un
certificado emitido por AC FNMT Usuarios

Fdo.: Francisco Javier Herraiz Martínez

Fecha: ...15./ .07./ 2025

Firmado por HERRAIZ MARTINEZ FRANCISCO JAVIER -el día 15/07/2025 \*\*\*1376\*\* con, un ido por AC certificado FNMT Usi



# MSC OF INDUSTRIAL ENGINEERING MSC OF SMART INDUSTRY

#### **MASTER'S THESIS**

# SENSOR DESIGN FOR CHARACTERIZATION OF METALLIC NANOPARTICLES

Author: Álvaro Martín Martín

**Supervisors:** 

Romano Giannetti

Francisco Javier Herraiz Martínez

Madrid July 2025

## Contents

1. State of the Art	13
1.1. Introduction	13
1.2. Nano-particles: What are they?	14
1.2.1. Classification Criteria	14
1.2.1.1. Nanomaterial classification	14
1.2.1.2. Nanoparticle classification	15
1.2.2. Nanoparticle Production Methods	16
1.2.2.1. Top-Down Approaches	16
1.2.2.2. Bottom-Up Approaches	16
1.2.2.3. Wire Explosion as a Nanoparticle Production Method	17
1.2.3. Properties of Nanoparticles	17
1.2.3.1. Physicochemical Properties of Nanoparticles	17
1.2.3.2. Mechanical Properties	17
•	18
	18
1	18
7	18
•	19
	19
	19
	20
1	21
1.3.1. Nano-particle Characterization and Classification Techniques	21
	21
	22
Č	23
	23
C	26
	26
1.4.2. Physical Principles of Metamaterial-Based Sensing	27
1.4.3. Key Applications in Chemical, Biological, and Physical Sensing	29
C	29
	30
1.4.3.3. Physical Sensing	30
1.4.4. Advances and Challenges	31
2. Sensing	33

2.1. Sensor Design Motivation and Context	33
2.2. Electromagnetic Modeling and Design Methodology	36
2.3. Resonator Tuning and Material Considerations	38
2.4. Fabrication Process and Expected Performance	39
2.5. Measurement Protocol for Sedimentation Profiling	41
3. Measurements	43
3.1. MUT Preparation	43
3.2. Sonication Time Determination	46
3.3. Material Differentiation	48
3.4. Size Differentiation	50
4. Time Constant Extraction	<b>52</b>
4.1. Time Constant Extraction Procedure	52
4.1.1. Multi-Exponential Formulation	53
4.1.2. Inverse Problem and Ill-Posedness	54
4.1.3. Regularization and Stabilization of the Solution	55
4.1.4. Implementation	56
4.2. Differentiating Between Copper Nanoparticle Samples	57
4.3. Mixing Copper Nanoparticles	59
4.4. Differentiating Between Copper and Iron Nanoparticle Samples	61
4.5. Comparison with University of Pisa's Results	63
5. Conclusion	65
5.1. Overview of the Research and Findings	65
5.2. Relevance to Industry 4.0 and Smart Manufacturing	65
5.3. Limitations and Challenges	66
5.4. Alignment with the Sustainable Development Goals (SDGs)	67
References	68

## **Abstract**

This thesis addresses the growing need for rapid, reliable characterization of metallic nanoparticles by demonstrating the experimental validation of a compact metamaterial sensor. We employ a microwave-frequency resonator whose response shifts measurably when the local material properties change.

Copper and iron nanoparticles (synthesized via controlled wire-explosion methods) are suspended in a liquid medium and introduced over the sensor surface. As the particles settle, they alter the effective electrical properties immediately above the resonator, producing a time-dependent change in its response. By continuously recording these shifts with a Virtual Network Analyzer, we obtain detailed frequency-vs-time curves that capture both how quickly particles sediment and the overall magnitude of their effect.

To extract meaningful parameters from these curves, we employ an established inversion algorithm. This algorithm fits the recorded data with a sum of exponential terms, yielding characteristic sedimentation time constants. The results demonstrate clear differentiation between copper and iron systems, even being able to differentiate between same-material samples given that they have sufficiently different size distributions.

By combining metamaterial resonance with data-driven inversion, this work establishes a non-destructive, optics-free methodology for real-time nanoparticle analytics. Its compact form factor and minimal sample preparation make it well suited for integration into flow-through process lines. This thesis lays the groundwork for future enhancements (including arrays of sensors for multiplexed measurements, extension to other nanomaterial types, and closed-loop control systems for autonomous process monitoring and optimization).

## Resumen

Esta tesis aborda la necesidad de caracterización rápida y fiable de nanopartículas metálicas al demostrar la validación experimental de un sensor metamaterial compacto. Empleamos un *microwave-frequency resonator* cuya respuesta se desplaza de manera medible cuando cambian las propiedades del material circundante.

Nanopartículas de cobre e hierro (sintetizadas mediante métodos controlados de explosión de hilo) se suspenden en un medio líquido y se introducen sobre la superficie del sensor. A medida que las partículas se asientan, modifican las propiedades eléctricas efectivas de la superficie del resonador, produciendo un cambio temporal en su respuesta. Al registrar continuamente estos desplazamientos con un *Virtual Network Analyzer*, obtenemos curvas detalladas de frecuencia contra tiempo que capturan tanto la velocidad de sedimentación de las partículas como su magnitud.

Para extraer parámetros significativos de estas curvas, empleamos un algoritmo de inversión. Dicho algoritmo ajusta los datos registrados como una suma de exponenciales, obteniendo las constantes de tiempo de sedimentación características. Los resultados demuestran una clara diferenciación entre sistemas de cobre y de hierro, llegando incluso a distinguir entre muestras del mismo material siempre que presenten distribuciones de tamaño suficientemente diferentes.

Al combinar la resonancia del *metamaterial* con la inversión basada en datos, este trabajo establece una metodología no destructiva y sin uso de lentes para la analítica en tiempo real de nanopartículas. Su factor de forma compacto y la preparación mínima de muestras lo hacen idóneo para su integración en líneas de proceso de flujo continuo. Esta tesis define las bases para futuras mejoras (incluyendo arrays de sensores para mediciones, extensión a otros tipos de nanomateriales y sistemas de control en lazo cerrado para la monitorización y optimización autónoma de procesos).

## Summary

#### Introduction

Characterization of nanoparticles (NPs) is crucial in nanoscience, but traditional measurement methods (electron microscopy, light scattering, etc.) are often slow, expensive, and require laborious procedures [1, 2]. This work proposes a sensor based on a square-spiral planar resonator (SSR) coupled to a vector network analyzer (VNA) to monitor NP sedimentation in a fluid in real time. When NPs settle onto the sensor, they modify the effective permittivity near the resonator, causing a shift in the resonance frequency [3]. The magnitude of this shift depends on the permittivity and volume of nanoparticulate material interacting with the sensor [3]. By measuring the sedimentation profile (frequency change versus time), it is possible to infer NP properties quickly, serving as an alternative to slower conventional techniques [4].

#### Methodology

An SSR with a high quality factor (Q) was designed to maximize sensitivity to small dielectric changes in its vicinity [5]. The SSR was connected to a VNA that continuously monitored the resonant frequency during the experiments. As case studies, metallic nanoparticles produced by wire explosion (a physical top-down method) were used [6]. In particular, the University of Pisa fabricated three batches of copper (Cu) nanoparticles—denoted A, B, and C—using different explosion parameters to obtain distinct size distributions. Additionally, a sample of iron (Fe) nanoparticles produced by the same method was considered. All NPs were dispersed in pure paraffin oil at a concentration of 10 mg/mL, chosen to ensure an almost saturated medium in which particles would eventually sediment.

To guarantee a homogeneous dispersion of the NPs before each measurement, sonication was applied for different time intervals. A preliminary experiment revealed that 15 minutes of sonication were sufficient to achieve a stable dispersion, since longer times (e.g., 30 minutes) did not show significant improvements in the sedimentation curves obtained.

During the measurement, a fixed volume of the sonicated dispersion was poured into a small container placed on the surface of the SSR. Figure 2.1 schematically illustrates this measurement process. As the NPs sediment under the action of gravity, the SSR's resonant frequency gradually decreases until stabilizing once a layer of particles has formed on the sensor. The resonant frequency was recorded as a function of time using the VNA, thus obtaining a characteristic sedimentation curve for each sample.

#### Results

#### **Material Differentiation**

The SSR sensor is capable of detecting different responses depending on the material present, due to differences in their electrical properties. For example, pure media (air, hexane, paraffin)

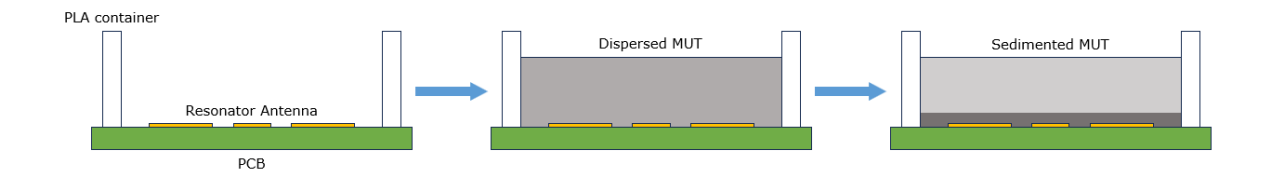


**Figure 1.** Schematic of the MUT measurement process. First (left), the SSR and container are cleaned of all liquid and solid residues to prepare the device for measurement; second (center), the dispersed MUT is poured into the PLA container; finally (right), over time the NPs sediment onto the PCB, causing a measurable shift in the MUT's resonant frequency.

exhibit distinct resonant frequencies when placed in the sensor's environment [7]. In the case of NPs dispersed in paraffin (a fixed-permittivity medium), the type of nanoparticle influences the magnitude and dynamics of the resonance shift. Comparative experiments with Cu and Fe NPs (dispersed in paraffin at the same concentration) showed clearly different sedimentation curves for each material [3].

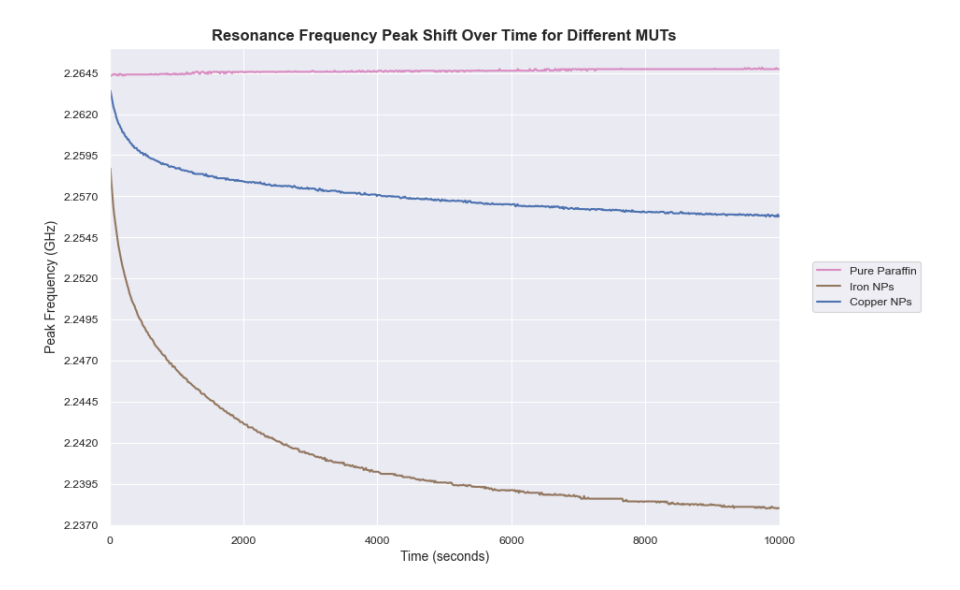


Figure 2. Resonant frequency as a function of the material under test (MUT).

Each material exhibits an exponential trend with a different time constant, reflecting that factors such as particle density and permittivity affect the sedimentation speed. This demonstrates that the sensor system can distinguish different nanoparticle materials through their sedimentation profile in a fluid.

#### **Size Distribution Differentiation**

Figure 3.8 shows the sedimentation curves (resonant frequency as a function of time) for the three Cu samples (A, B, C). All exhibit the typical exponential decay behavior, with comparable total frequency shifts between samples. At first glance, the differences between curves A, B, and C are subtle, making it difficult to classify the samples solely by direct inspection of these raw curves.

Since NP sedimentation in a fluid can be modeled as the superposition of multiple exponential processes (each associated with a particle size range), a multi-exponential decomposition analysis was applied to extract the *sedimentation time-constant distribution* of each sample [8]. This procedure is equivalent to solving an inverse Laplace transform problem with Tikhonov regularization [8, 9], yielding a distribution  $f(\tau)$  that assigns weight to different values of

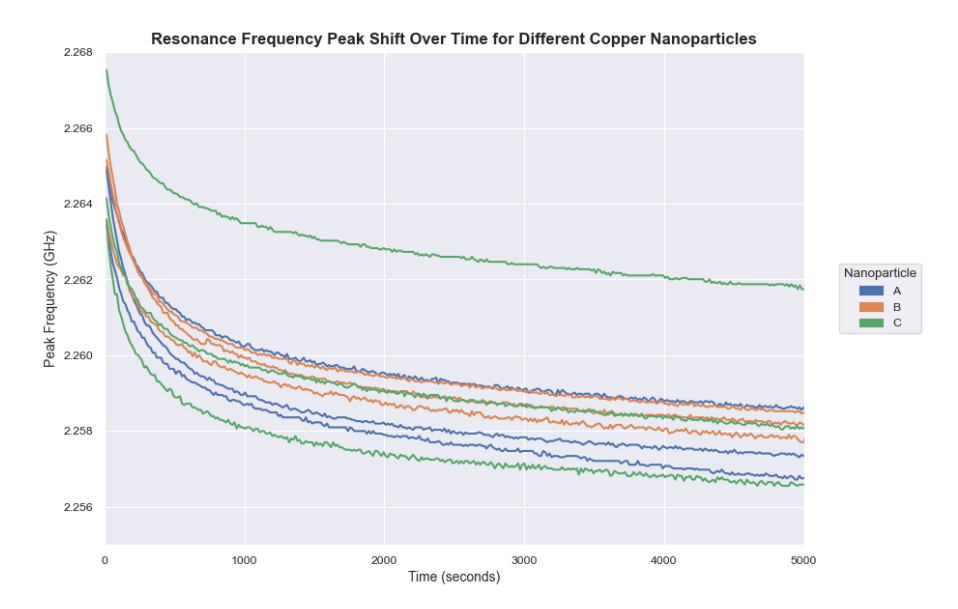


Figure 3. Resonant peak frequency as a function of time for copper nanoparticle dispersions A, B, and C.

 $\tau$  (characteristic sedimentation times) present in the signal. Intuitively,  $\tau$  relates to particle size: larger particles tend to sediment faster (smaller  $\tau$ ), while smaller particles sediment more slowly (larger  $\tau$ ).

In the experimental Cu data, Figure 4.2 shows the time-constant distribution obtained for the copper nanoparticle samples A, B, and C.

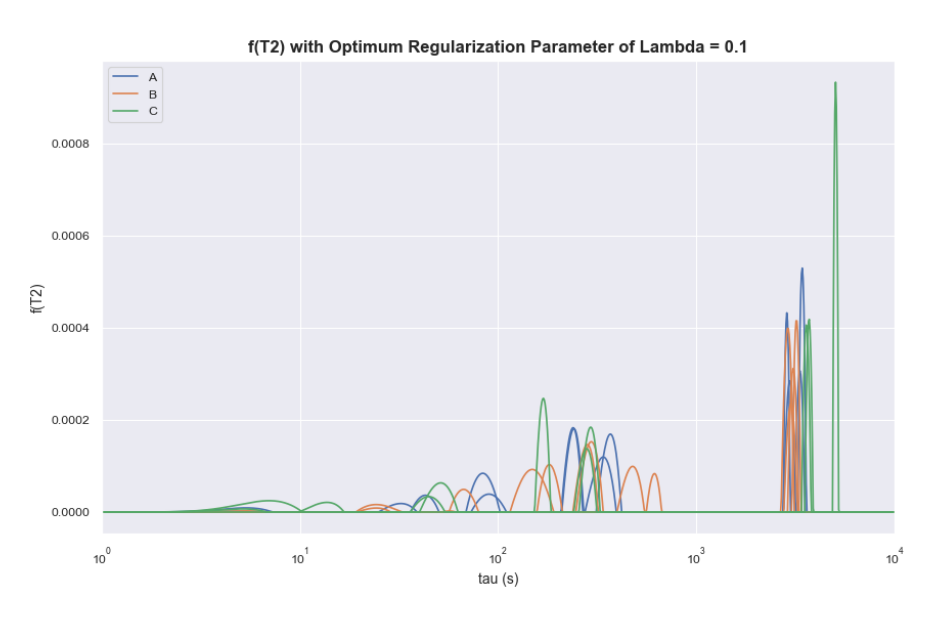
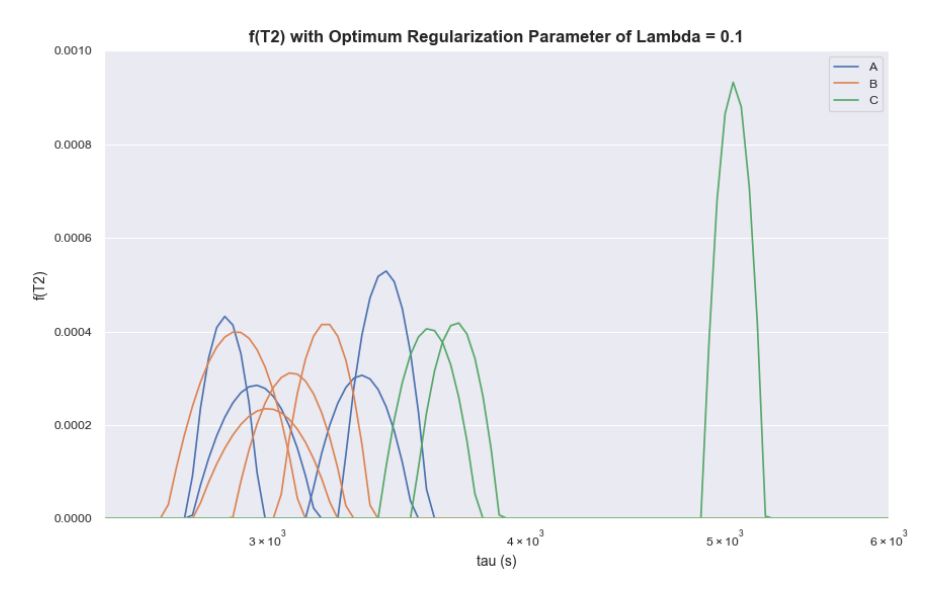


Figure 4. Time-constant distribution for copper nanoparticle samples A, B, and C.

Figure 4.3 provides a zoomed-in view of the main region where the most significant contributions are concentrated.

It can be observed that the distributions for A and B are practically indistinguishable, overlapping in the same  $\tau$  range. In contrast, sample C exhibits a different distribution, with greater weight in a different time-constant region than A/B. This indicates that the size distribution in C differs from that of A/B; for example, sample C may contain a higher proportion of larger particles than samples A and B.



**Figure 5.** Zoomed-in time-constant distribution in the main region for copper nanoparticle samples A, B, and C.

**Independent Validation by DLS** 

To corroborate this interpretation, the University of Pisa performed an independent characterization of the samples using dynamic light scattering (DLS). The results, presented in Figure 12, showed that A and B have very similar size distributions, while sample C is distinguished by containing a larger fraction of bigger particles than those in A and B.

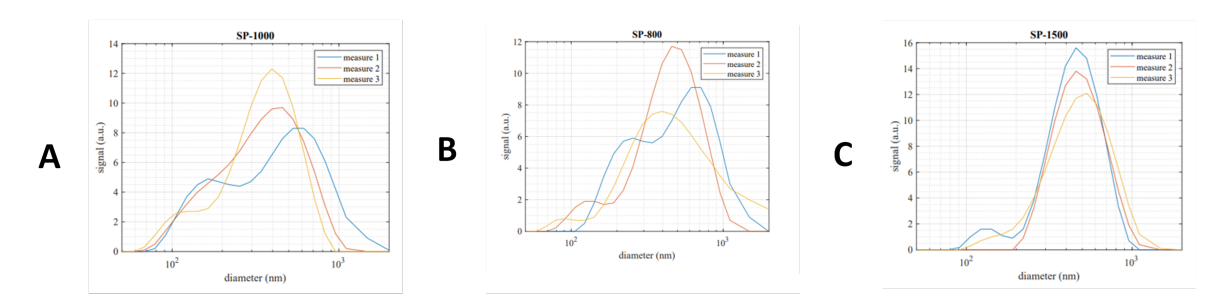


Figure 6. DLS data obtained by the University of Pisa in a double-blind analysis of the nanoparticles.

This qualitative trend agrees with the inference from the SSR sensor, providing confidence in the validity of the proposed method.

Additionally, a test was carried out by mixing nanoparticles from samples B and C in equal proportions to evaluate whether the sensor could discern a composite distribution. The sedimentation curve of this mixture was, as expected, intermediate between those of B and C alone.

It was shown that the time-constant distribution of the mixture falls between those of B and C, although skewed more toward that of C.

This suggests that in the mixture, the larger particles from C dominate the initial sedimentation (sedimenting earlier), so that the contribution of the smaller particles from B is partially masked in the overall behavior.

#### **Extension to Other Materials**

As mentioned, the method was also tested with iron (Fe) nanoparticles. The time-constant distributions for an Fe sample contrasted with those of Cu show marked differences.

Even without isolating only the main component of  $\tau$ , the full distribution for Fe is distinguishable from those of Cu, suggesting that the material's specific properties (higher density of Fe, different dielectric behavior, etc.) influence the sedimentation profile in a detectable manner. Therefore, the technique could be extended to classify nanoparticles of different materials, not just for size differences within the same material.

#### **Conclusions**

A novel sensor system based on a square-spiral planar electromagnetic resonator was presented and validated for the rapid characterization of metallic nanoparticles. By monitoring NP sedimentation in a fluid in real time, the sensor provides a "fingerprint" for each sample, enabling differentiation of both particle-size variations and material differences among the NPs.

Experiments demonstrated that the SSR sensor, combined with a network analyzer and numerical inversion techniques, can distinguish between Cu nanoparticle samples with different size distributions, aligning with results obtained by traditional methods (SEM/TEM, DLS) but in a fraction of the time and effort. It was also verified that the resonant response differentiates nanoparticles of different composition (Cu vs. Fe) under identical dispersion conditions, suggesting versatile applications in nanomaterial classification.

Advantages of this approach include its speed (results in minutes or hours instead of days), simplicity of sample preparation (simply dispersing them in a liquid), and the feasibility of automating the process for online NP production monitoring [4]. However, there are limitations: the method provides relative information and requires calibration with reference samples to translate measured parameters (e.g., time constants) into absolute size or concentration values. Resolution for distinguishing very subtle size differences may be limited by measurement noise and by signal overlap when distributions are very similar (as occurred between A and B). Additionally, for very small nanoparticles (well below 100 nm), gravitational sedimentation is very slow, which could hinder characterization in reasonable times or require acceleration (e.g., via centrifugation).

In conclusion, the planar-resonator-based sensor has proven to be a promising tool for rapid nanoparticle characterization, complementing existing techniques. With future developments—such as more robust calibrations, resonator designs with higher sensitivity, or the use of more sophisticated analysis algorithms—this methodology could be integrated into industrial environments for real-time quality control and classification of nanomaterials.

## Resumen

#### Introducción

La caracterización de nanopartículas (NPs) es crucial en la nanociencia, pero los métodos tradicionales de medición (microscopía electrónica, dispersión de luz, etc.) suelen ser lentos, costosos y requieren procedimientos laboriosos [1, 2]. Este trabajo propone un sensor basado en un resonador planar de espiral cuadrada (SSR, por sus siglas en inglés) acoplado a un analizador vectorial de redes (VNA) para monitorear en tiempo real la sedimentación de NPs en un fluido. Cuando las NPs se depositan sobre el sensor, modifican la permitividad efectiva cercana al resonador, provocando un corrimiento de la frecuencia de resonancia [3]. La magnitud de este corrimiento depende de la permitividad y el volumen de material nanoparticulado que interactúa con el sensor [3]. Al medir el perfil de sedimentación (cambio de frecuencia versus tiempo), es posible inferir propiedades de las NPs de forma rápida, sirviendo como alternativa a técnicas convencionales más lentas [4].

#### Metodología

Se diseñó un SSR de alto factor de calidad (Q) para maximizar la sensibilidad a pequeños cambios dieléctricos en su cercanía [5]. El SSR se conectó a un VNA que monitorea continuamente la frecuencia resonante durante los experimentos. Como casos de estudio, se utilizaron nanopartículas metálicas producidas mediante explosión de alambre (*Wire Explosion*, un método físico de *top-down*) [6]. En particular, la Universidad de Pisa fabricó tres lotes de nanopartículas de cobre (Cu) —denominados A, B, C— utilizando distintos parámetros de explosión para obtener distribuciones de tamaño diferenciadas. Adicionalmente, se consideró una muestra de nanopartículas de hierro (Fe) producidas con el mismo método. Todas las NPs se dispersaron en aceite de parafina pura a una concentración de 10 mg/mL, elegida para asegurar un medio casi saturado donde las partículas eventualmente sedimentan.

Para garantizar una dispersión homogénea de las NPs antes de cada medición, se aplicó sonicación por diferentes intervalos de tiempo. Un experimento preliminar reveló que 15 minutos de sonicación son suficientes para lograr una dispersión estable, ya que tiempos mayores (por ejemplo, 30 minutos) no mostraron mejoras significativas en las curvas de sedimentación obtenidas.

Durante la medición, un volumen fijo de la dispersión sonicada se vertió en un pequeño contenedor colocado sobre la superficie del SSR. En la Figura 2.1 se ilustra esquemáticamente este proceso de medición. A medida que las NPs sedimentan bajo la acción de la gravedad, la frecuencia de resonancia del SSR disminuye gradualmente hasta estabilizarse al formarse una capa de partículas sobre el sensor. La frecuencia resonante se registró en función del tiempo usando el VNA, obteniendo así una curva de sedimentación característica para cada muestra.

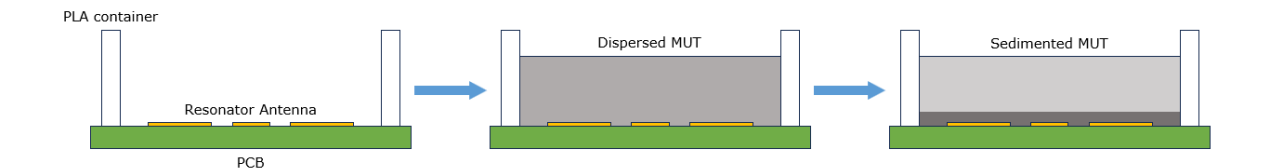


**Figure 7.** Esquema del proceso de medición del MUT. Primero (izquierda), se limpian el SSR y el contenedor, retirando todos los residuos líquidos y sólidos para dejar el dispositivo listo para la medición; Segundo (centro), se vierte el MUT disperso en el contenedor de PLA; Finalmente (derecha), con el tiempo las NPs sedimentan sobre la PCB, provocando un corrimiento medible en la frecuencia de resonancia del MUT.

#### Resultados

#### Diferenciación de materiales

El sensor SSR es capaz de detectar distintas respuestas según el material presente, debido a las diferencias en sus propiedades eléctricas. Por ejemplo, medios puros (aire, hexano, parafina) exhiben frecuencias de resonancia distintas cuando se colocan en el entorno del sensor [7]. En el caso de NPs dispersas en parafina (medio con permitividad fija), el tipo de nanopartícula influye en la magnitud y dinámica del corrimiento de la resonancia. Experimentos comparativos con NPs de Cu y de Fe (dispersadas en parafina a la misma concentración) mostraron curvas de sedimentación claramente diferentes para cada material [3].

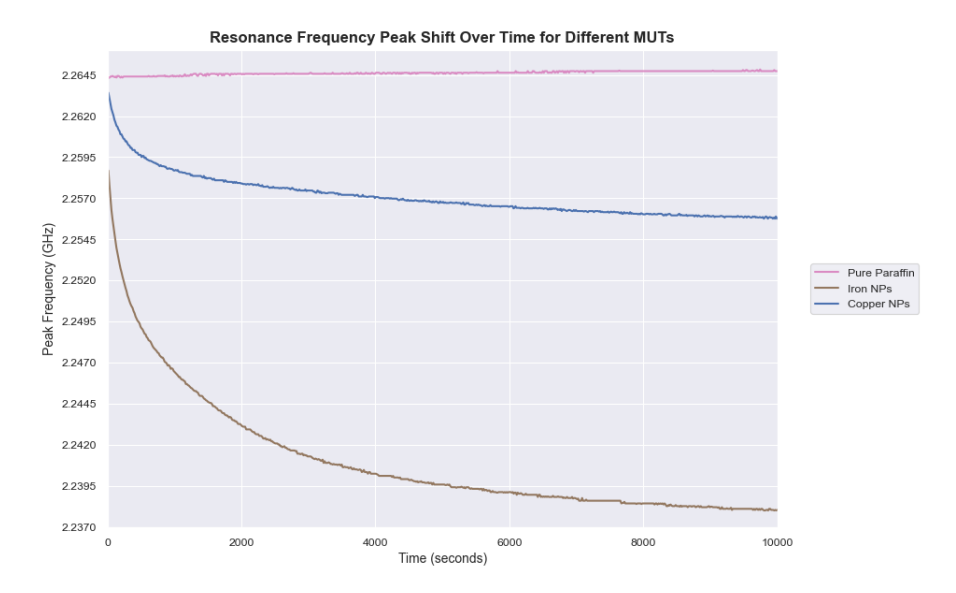
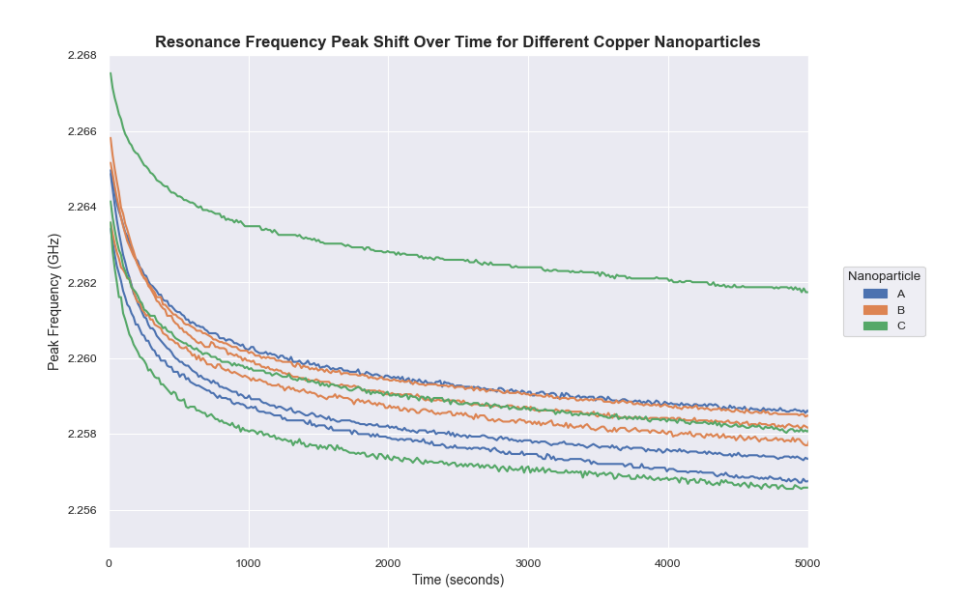


Figure 8. Frecuencia de resonancia según el material bajo prueba (MUT).

Cada material presenta una tendencia exponencial con distinta constante de tiempo, reflejando que factores como la densidad y la permitividad de las partículas afectan la velocidad de sedimentación. Esto demuestra que el sistema sensor puede distinguir distintos materiales de nanopartículas a través de su perfil de sedimentación en un fluido.

#### Diferenciación de distribuciones de tamaño

La Figura 3.8 muestra las curvas de sedimentación (frecuencia resonante en función del tiempo) para las tres muestras de Cu (A, B, C). Todas exhiben el comportamiento típico de decaimiento exponencial, con desplazamientos totales de frecuencia comparables entre muestras. A simple vista las diferencias entre las curvas de A, B y C son sutiles, lo que dificultaría clasificar las muestras únicamente mediante inspección directa de estas curvas brutas.



**Figure 9.** Frecuencia de resonancia pico en función del tiempo para las dispersiones de nanopartículas de cobre A, B y C.

Dado que la sedimentación de NPs en un fluido puede modelarse como la superposición de múltiples procesos exponenciales (cada uno asociado a un rango de tamaños de partícula), se aplicó un análisis matemático de descomposición multi-exponencial para extraer la distribución de constantes de tiempo de sedimentación de cada muestra [8]. Este procedimiento equivale a resolver un problema inverso de transformada de Laplace con regularización (Tikhonov) [8, 9], obteniendo una distribución  $f(\tau)$  que asigna peso a diferentes valores de  $\tau$  (tiempos característicos de sedimentación) presentes en la señal. Intuitivamente,  $\tau$  se relaciona con el tamaño de partícula: partículas más grandes tienden a sedimentar más rápido (menor  $\tau$ ) mientras que partículas más pequeñas sedimentan más lentamente (mayor  $\tau$ ).

En los datos experimentales de Cu, la Figura 4.2 presenta la distribución de constantes de tiempo obtenida para las muestras A, B y C de nanopartículas de cobre.

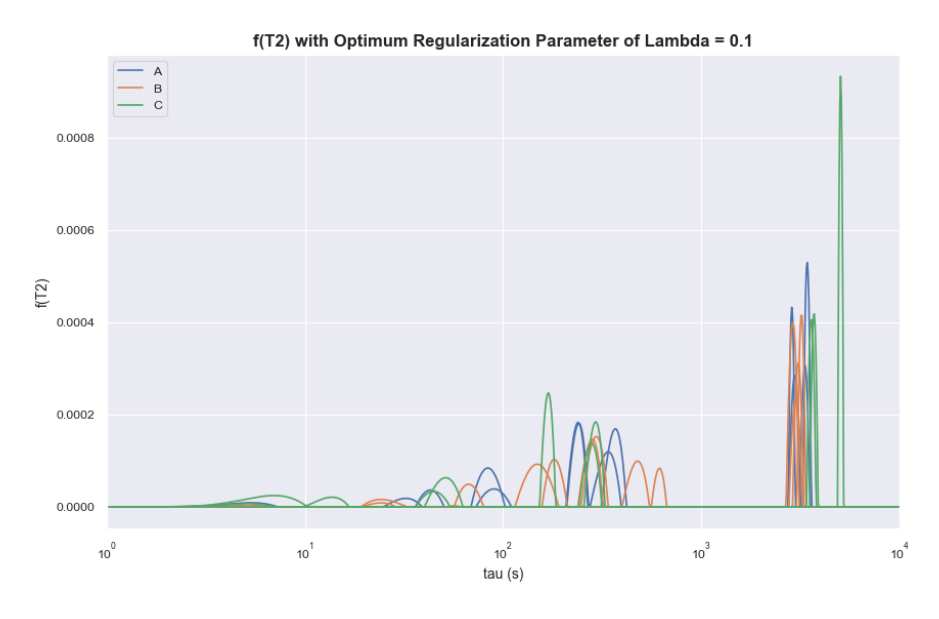
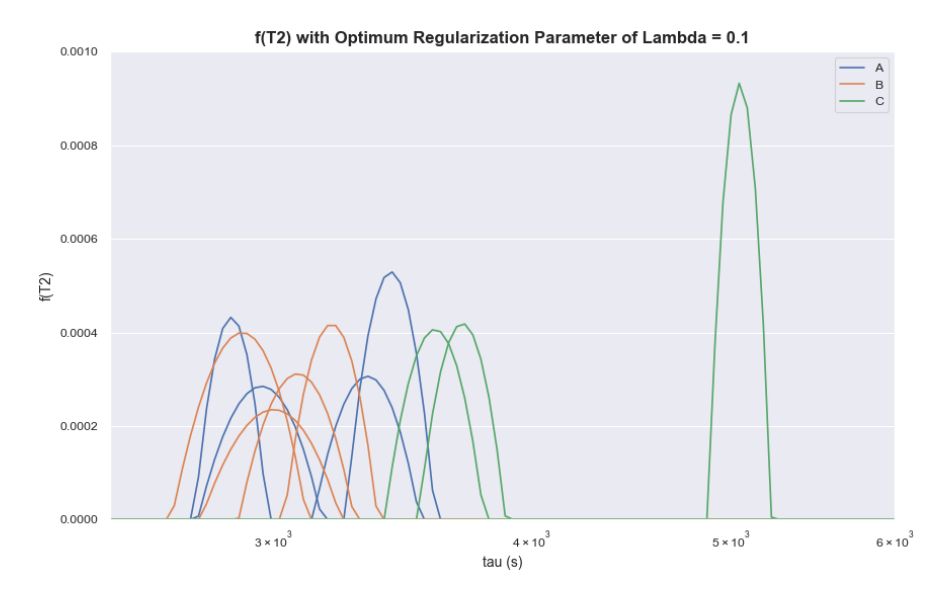


Figure 10. Distribución de constantes de tiempo para las muestras A, B y C de nanopartículas de cobre.

La Figura 4.3 amplía la región principal donde se concentran las contribuciones más significativas.



**Figure 11.** Distribución de constantes de tiempo ampliada en la región principal para las muestras A, B y C de nanopartículas de cobre.

Se observa que las distribuciones de A y B son prácticamente indistinguibles entre sí, solapándose en un mismo rango de  $\tau$ . En contraste, la muestra C exhibe una distribución diferente, con mayor peso en otra zona de constantes de tiempo distinta a la de A/B. Esto indica que la distribución de tamaños en C difiere de la de A/B; por ejemplo, la muestra C podría contener una mayor proporción de partículas de mayor tamaño que las de A y B.

Para corroborar esta interpretación, la Universidad de Pisa realizó una caracterización independiente de las muestras mediante dispersión de luz (DLS). Los resultados, presentados en la Figura 12, mostraron que A y B tienen distribuciones de tamaño muy similares, mientras que la muestra C se distingue por contener una mayor fracción de partículas de mayor tamaño que las presentes en A y B.

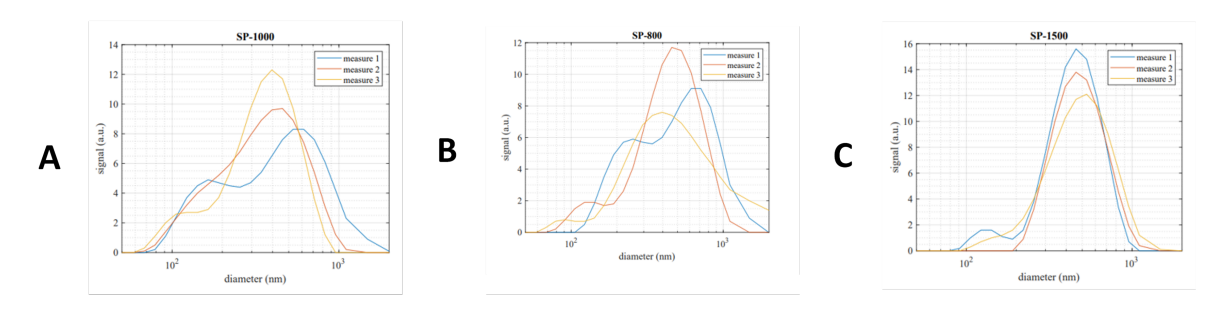


**Figure 12.** Datos del DLS realizado por la Universidad de Pisa en un análisis doble ciego de las nanopartículas.

Esta tendencia cualitativa concuerda con lo inferido a partir del sensor SSR, brindando confianza sobre la validez del método propuesto.

Adicionalmente, se efectuó una prueba mezclando nanopartículas de las muestras B y C en proporciones iguales, para evaluar si el sensor podía discernir una distribución compuesta. La curva de sedimentación de esta mezcla resultó, como era de esperar, intermedia entre las de B y C por separado.

Se demostró que la distribución de constantes de tiempo de la mezcla se ubica entre las correspondientes a B y C, aunque inclinándose más hacia la de C.

Esto sugiere que en la mezcla, las partículas más grandes de C dominan la sedimentación inicial (sedimentando antes), de modo que la contribución de las partículas más pequeñas de B queda en parte enmascarada en el comportamiento global.

#### Extensión a otros materiales

Como se mencionó, el método se probó también con nanopartículas de hierro. Las distribuciones de constantes de tiempo para una muestra de Fe contrastada con las de Cu evidencia diferencias marcadas.

Incluso sin aislar solo la componente principal de  $\tau$ , la distribución completa de Fe se distingue de las de Cu, lo que sugiere que las propiedades particulares del material (mayor densidad del Fe, distinto comportamiento dieléctrico, etc.) influyen en el perfil de sedimentación de forma detectable. Por lo tanto, la técnica podría extenderse para clasificar nanopartículas de distintos materiales, no solo para diferencias de tamaño dentro del mismo material.

#### Conclusiones

Se presentó y validó un sistema sensor novedoso basado en un resonador electromagnético planar tipo espiral cuadrada para la caracterización rápida de nanopartículas metálicas. Mediante el monitoreo en tiempo real de la sedimentación de NPs en un fluido, el sensor proporciona una "firma" o huella digital de cada muestra, permitiendo distinguir tanto diferencias en tamaño de partícula como diferencias de material de las NPs.

Los experimentos demostraron que el sensor SSR, combinado con un analizador de redes y técnicas de inversión numérica, puede diferenciar entre muestras de nanopartículas de Cu con distribuciones de tamaño distintas, alineándose con los resultados obtenidos por métodos tradicionales (SEM/TEM, DLS) pero en una fracción del tiempo y esfuerzo. Asimismo, se verificó que la respuesta resonante distingue nanopartículas de diferente composición (Cu vs Fe) bajo las mismas condiciones de dispersión, lo que sugiere aplicaciones versátiles en la clasificación de nanomateriales.

Entre las ventajas de este enfoque destacan su rapidez (resultados en minutos u horas en lugar de días), la sencillez en la preparación de las muestras (basta con dispersarlas en un líquido) y la factibilidad de automatizar el proceso para monitoreo en línea de la producción de NPs [4]. No obstante, existen limitaciones: el método brinda información relativa y requiere calibración con muestras de referencia para traducir los parámetros medidos (p.ej., constantes de tiempo) a valores absolutos de tamaño o concentración. La resolución para distinguir diferencias muy sutiles en tamaños cercanos puede verse limitada por el ruido de medición y por la superposición de señales cuando las distribuciones son muy similares (como ocurrió entre A y B). Adicionalmente, para nanopartículas de dimensiones muy pequeñas (mucho menores de 100 nm), la sedimentación gravitacional es muy lenta, lo que podría dificultar su caracterización en tiempos razonables o requerir aceleración (p.ej., mediante centrifugación).

En conclusión, el sensor basado en resonador planar demostró ser una herramienta prometedora para la caracterización expedita de nanopartículas, complementando las técnicas existentes. Con desarrollos futuros, como calibraciones más robustas, diseños de resonadores con mayor sensibilidad o el empleo de algoritmos de análisis más sofisticados, esta metodología podría integrarse en entornos industriales para control de calidad y clasificación de nanomateriales en tiempo real.

1

## State of the Art

#### 1.1. Introduction

Nanotechnology refers to the branch of science and engineering which studies structures less than 100 nanometers in length. Nanotechnology has many applications in revolutionary fields such as electronics, biotechnology and medicine.[1] The demand for low-cost sensors in all industries is increasing. Particles ranging from 1 nm to 100 nm are usually referred to as nanoparticles (NPs). These powders show easy bonding with the contact materials, have a large surface area, low melting point and peculiar electromagnetic and optical characteristics[2].

Characterizing nanoparticles is the first step to guaranteeing they behave the way they should. Evaluating the outcome of the production processes is important in order to readjust the production parameters to obtain the desired output in a closed loop. Measuring some properties, including particle size, size distribution, surface charge, or shape is generally not an easy task [10]. Key size parameters are commonly obtained using microscopy techniques, mainly Scanning Electron Microscopy (SEM) and Transmission Electron Microscopy (TEM). These methods are used alongside visual measurements, since they output images of the particles, enabling the assessment of dimensional distributions.

These characterization methods often require a time-consuming process with complex instrumentation and many manual interventions, causing huge delays in the fabrication process and verification of the experiments while making them quite expensive. The development of new, faster and cheaper fabrication processes is key in the development and integration of nanotechnology and nanoparticles into industrial processes[2].

### 1.2. Nano-particles: What are they?

Due to their unique properties, nanoparticles and nanomaterials are used in a variety of applications, ranging from water treatment, medicine, agriculture to energy storage [11]. There are two main factors which lead to the different behaviour of NPs in contrast to the same materials at larger dimensions: surface effects and quantum effects. These factors make nanomaterials exhibit enhanced or novel mechanical, thermal, magnetic, electronic, optical, and catalytic properties [12].

Nanomaterials have different surface effects compared to the bulk materials mainly due to their high surface area to mass ratio and the number of direct neighbours of surface atoms [12]. As a consequence of this, nanomaterial properties change regarding their bulk counterpart. For example, having fewer direct neighbor atoms for the atoms situated at the surface results in lowering the binding energy per atom for nanomaterials. This changes the melting point of the material following the Gibbs-Thomson equation (equation 1.1):

$$\Delta T_m(d) = T_{mB} - T_m(d) = T_{mB} \frac{4\sigma_{sl}}{H_f \rho_s d}$$
(1.1)

where [13]:

- $T_{mB}$  = bulk melting temperature
- $\sigma_{sl}$  = solid–liquid interface energy (per unit area)
- $H_f$  = bulk enthalpy of fusion (per gram of material)
- $\rho_s$  = density of solid
- d = nanoparticle size

Therefore, following this equation, the melting point of a 2.5 mm gold NP is 407 degrees lower than the melting point of bulk gold [14].

#### 1.2.1. Classification Criteria

#### 1.2.1.1. Nanomaterial classification

Nanomaterials are fundamental to the field of nanotechnology. These materials are uniquely defined by having at least one of their dimensions within the nanoscale range, which typically means they measure less than 100 nanometers.

Nanomaterials can be categorized into four primary types based on their dimensional characteristics:

- 1. **Zero-dimensional (0D) nanomaterials**: In this category, all three spatial dimensions are confined to the nanoscale. These materials are essentially nanoscale in every direction. Common examples include quantum dots, fullerenes, and spherical nanoparticles.
- 2. **One-dimensional (1D) nanomaterials**: These materials have two dimensions within the nanoscale, while the third extends beyond it. They typically have a high aspect ratio and are elongated in one direction. Examples include nanowires, nanotubes, nanorods, nanofibers, and nanohorns.
- 3. **Two-dimensional (2D) nanomaterials**: In this group, only one dimension remains at the nanoscale, while the other two dimensions are larger. These materials often appear as

thin films or sheets and include structures like graphene layers, nanosheets, nanofilms, and nanolayers.

4. Three-dimensional (3D) nanomaterials or bulk nanostructured materials: These materials are not restricted to the nanoscale in any of their dimensions. However, they still contain nanoscale features within their overall structure. This category includes bulk powders, nanocomposites, dispersed nanoparticle systems, and assemblies of nanowires or nanotubes.

Each class of nanomaterial offers unique properties and potential applications, making their classification an important step in understanding and leveraging their capabilities in fields such as electronics, medicine, energy, and materials science.

#### 1.2.1.2. Nanoparticle classification

drug delivery [15] and cancer therapy.

#### Composition based classification:

Based on their composition, NPs are generally classified into three classes [15]:

- *Organic Nanoparticles*: Organic nanoparticles (NPs) are composed of organic compounds such as proteins, carbohydrates, lipids, and polymers [16]. Common examples include dendrimers, liposomes, micelles, and protein complexes like ferritin.

  These NPs are typically biodegradable, non-toxic, and, in some cases, such as liposomes, may have a hollow core. They are sensitive to heat and light [15] due to their organic nature and are generally stabilized through non-covalent interactions, making them less structurally rigid but allowing for easier breakdown and elimination from the body. Their functionality depends on factors such as composition, surface morphology, and stability. Currently, organic NPs are widely used in biomedicine, especially for targeted
- *Carbon-based Nanoparticles*: This class includes nanoparticles composed exclusively of carbon atoms [15]. Notable examples are fullerenes, carbon black, and carbon quantum dots
  - Fullerenes, such as C<sub>60</sub>, have a closed-cage structure resembling a soccer ball [17]. Carbon black consists of aggregates of fused carbon particles, while carbon quantum dots are sub-10 nm spherical particles with distinct optical and electronic properties [14]. Carbon-based NPs are applied in fields like drug delivery, energy storage, bioimaging, photovoltaics, and environmental sensing. More complex carbon forms such as nanodiamonds and carbon nano-onions also show promise, particularly due to their low toxicity and high biocompatibility, making them suitable for drug delivery and tissue engineering [14].
- *Inorganic Nanoparticles*: Inorganic NPs are those not derived from carbon-based or organic sources. They include metal, semiconductor, and ceramic nanoparticles. Metal NPs, which can be monometallic, bimetallic, or polymetallic, exhibit unique optical, thermal, electrical, and magnetic properties due to phenomena like localized surface plasmon resonance [18].
  - Their synthesis can be finely tuned to control size, shape, and surface characteristics, which is crucial for advanced technological applications [19].
  - Semiconductor NPs, made from materials with intermediate conductivity, show tunable bandgap properties that differ significantly from their bulk forms. This makes them valuable in photocatalysis and optoelectronic devices. Ceramic NPs, composed of inorganic

compounds such as oxides, carbides, and phosphates, are usually formed through high-temperature processes.

Found in various structural forms, they are notable for their high stability and loading capacity, making them useful in both medical applications and industrial areas like catalysis, dye degradation, and photonics [14].

#### 1.2.2. Nanoparticle Production Methods

Synthesis methods for NPs are often classified into top-down and bottom-up approaches, each with their advantages and limitations regarding particle size distribution, morphology, cost, scalability and environmental impact.

#### 1.2.2.1. Top-Down Approaches

Top-down methods begin with bulk materials, reducing them to nano-scale dimensions through physical or mechanical processes. Relevant techniques within this approach include mechanical milling, laser ablation and wire explosion.

*Mechanical milling* involves the grinding of bulk materials in high-energy ball mills, where particle size is reduced through repeated impact and abrasion. This method is widely used for large-scale production due to its cost-effectiveness and ability to yield high-purity particles. However, mechanical milling poses challenges such as potential contamination from the milling media and often requires extended processing to achieve smaller particle sizes. It is used to blend metals like aluminium with magnesium to modify their combustion properties [6].

*Laser ablation* is useful for generating highly pure particles with narrow size distributions. This technique is particularly advantageous for generating highly pure particles with narrow size distributions. Nonetheless, laser ablation is energy-intensive and may experience reduced efficiency over time as particles accumulate and obstruct the laser path. Laser ablation is used to produce NPs such as Al2O3 and silicon when high purity and controlled particle size are critical [6].

Wire Explosion (WE), which consists of a metal wire undergoing explosive fragmentation when subjected to a high-current pulse, presents unique benefits for NP synthesis. During the WE process, the wire material is rapidly ejected in the form of metal droplets and vapour, forming NPs in a surrounding medium. This method proves particularly efficient and environmentally favourable, especially in underwater applications, where energy loss is minimized as water prevents plasma formation along the wire surface and efficiently transfers the electrical energy to the wire for disintegration. While challenging to characterize due to broad and multi-modal size distributions, WE is highly reproducible for specific applications requiring stable, high-quality NPs [20].

#### 1.2.2.2. Bottom-Up Approaches

In contrast to top-down methods, bottom-up approaches synthesize nanoparticles from atomic or molecular precursors, assembling them into nanoscale structures. Bottom-up methods include chemical reduction, sol-gel synthesis, and chemical vapour deposition (CVD), each offering advantages for applications requiring specific particle shapes or material compositions.

*Chemical reduction* is a widely employed technique in which metal ions are reduced in a solution to yield NPs. This method offers substantial control over particle size and shape and is a relatively low-cost option. However, chemical reduction requires stabilized agents, which may introduce contaminants. It is frequently used to synthesize gold and silver NPs, particularly in biomedical applications where particle stability and uniformity are essential [6].

*Chemical vapour deposition (CVD)* involves vaporizing metal precursors and depositing them onto a substrate, where they decompose to form NPs. This technique is extensively applied in electronics and solar cells, as it produces high-purity NPs with controlled morphology. While CVD is scalable and effective for high-purity NP production, it requires expensive equipment and poses hazards due to the use of toxic precursors and high operating temperatures [21].

#### 1.2.2.3. Wire Explosion as a Nanoparticle Production Method

As discussed previously, the WE method presents a robust and environmentally favourable alternative for NP synthesis, offering the potential for high-quality, stable NP production suitable for various scientific and industrial applications. The method's unique capabilities make it well-suited for fields that demand consistent, high-quality NP production [6].

Copper and Iron nanoparticles are produced at the University of Pisa using the wire-explosion method. These NP's characteristics are assessed using the above-mentioned SEM techniques. These NPs are produced by flowing  $1\cdot 10^7\,\text{A/m}^2\,$  to  $1\cdot 10^9\,\text{A/m}^2\,$  through a cylindrical copper or iron wire with a diameter of 1 mm and with a length of 30 mm. As shown in Figure 1.1, the circuit which provides the current consists of a 765  $\mu\text{F}$  with a voltage limit of 10 kV loaded through a High Voltage (HV) power supply. Voltage is monitured using a 1:1000 voltage probe and current using a Rogowski coil, connected to an oscilloscope. In order to collect the resulting NPs from the fabrication process, distilled water was used as a medium surrounding the exploding wire.

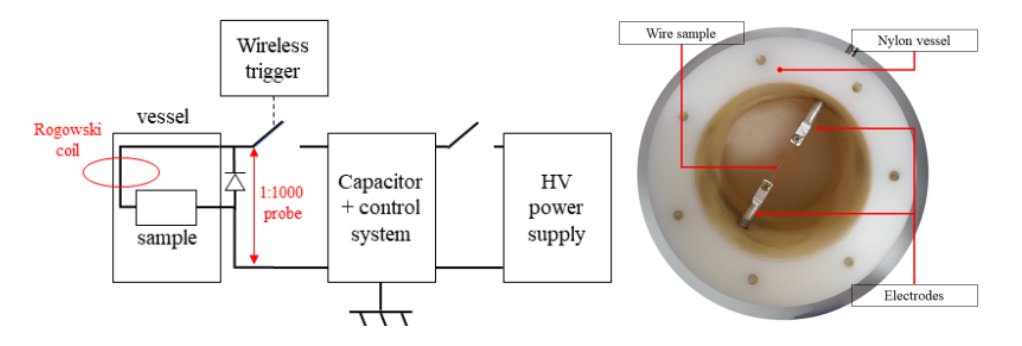


**Figure 1.1.** To the left, circuit for the wire-explosion fabrication process. To the right, vessel with a loaded wire sample used for the wire-explosion fabrication process.

#### 1.2.3. Properties of Nanoparticles

#### 1.2.3.1. Physicochemical Properties of Nanoparticles

Nanoparticles (NPs) exhibit unique physiochemical properties that significantly differ from their bulk counterparts due to quantum effects and surface phenomena. These differences become pronounced at the nano-scale and include mechanical, thermal, magnetic, electronic, optical, and catalytic characteristics [22, 23, 24, 25]. These unique properties arise primarily from enhanced surface effects and quantum confinement, which considerably alter the chemical reactivity, melting temperature, electrical conductivity, and optical behaviours, providing nanoparticles with mixed functionalities that are applicable in diverse scientific and technological fields.

#### 1.2.3.2. Mechanical Properties

The mechanical properties of nanoparticles merge attributes such as brittleness, toughness, hardness, elasticity, ductility, and rigidity. At the nano-scale, nanoparticles typically demonstrate mechanical behaviours distinct from their bulk equivalents. For instance, *FeAl* alloy powders exhibit superior ductility and plasticity when their dimensions are reduced to nano-scale sizes.

These improved mechanical characteristics are largely due to intensified surface forces, including *Van der Waals* forces, electrostatic interactions, and hydration forces. Moreover, prominent theories such as DLVO (Derjaguin–Landau–Verwey–Overbeek), JKR (Johnson–Kendall–Roberts), and DMT (Derjaguin–Muller–Toporov) have been developed and utilized to better understand and predict the behaviour of nanoparticles in different mechanical contexts, especially focusing on surface adhesion and deformation behaviours [26, 27, 28, 29, 30].

#### 1.2.3.3. Thermal Properties

The thermal characteristics of nanoparticles, including thermal conductivity, thermoelectric power, heat capacity, and thermal stability, are mainly affected by their reduced sizes. The thermal conductivity of nanoparticles tends to increase as their size decreases, primarily due to an elevated surface-to-volume ratio, allowing greater electron-mediated heat conduction. For example, suspensions containing copper nanoparticles in ethylene glycol exhibit substantial improvements in thermal conductivity compared to pure ethylene glycol. Furthermore, nanoparticles possess significantly lowered melting points compared to their bulk materials, an effect attributable to their elevated surface free energy and reduced binding energies. These unique thermal behaviors ease their applications in advanced thermal management systems and energy storage solutions [31, 32, 33, 34].

#### 1.2.3.4. Magnetic Properties

Nanoparticles frequently exhibit magnetic properties such as *superparamagnetism*, characterized by zero residual magnetization once the external magnetic field is removed. This phenomenon occurs due to the decreased magnetic anisotropy energy in nanoparticles as their size is reduced below certain thresholds. The magnetic coercivity of nanoparticles also strongly depends on their dimensions, transitioning from *superparamagnetic* to *ferromagnetic* behaviours as particle size increases beyond critical radii. Moreover, the magnetic properties of nanoparticles are significantly affected by their shape, composition, and crystal structure, with alloy nanoparticles often showing enhanced magnetic characteristics compared to their single-metal examples. These magnetic attributes are essential for numerous applications, including magnetic resonance imaging (MRI) contrast agents, targeted drug delivery systems, and magnetic data storage technologies [35, 36, 37].

#### 1.2.3.5. Electronic and Optical Properties

Nanoparticles display distinctive electronic and optical properties primarily attributed to quantum confinement and localized surface plasmon resonance (LSPR). Quantum confinement effects become significant when nanoparticles approach the exciton Bohr radius, altering their electronic energy levels hence influencing their optical properties. LSPR emerges prominently in metallic nanoparticles when photon frequencies resonate with collective oscillations of conduction electrons, resulting in notable optical absorption and scattering phenomena. These effects are dependent on nanoparticle size, shape, and the dielectric properties of their environment. Also, noble metal nanoparticles like silver and gold are widely investigated due to their pronounced plasmonic characteristics, enabling their application in fields such as biosensing, photovoltaic cells, and photocatalysis [38, 39, 40].

#### 1.2.3.6. Catalytic Properties

Nanoparticles are highly advantageous in catalysis due to their significant surface-to-volume ratios, providing abundant reactive sites that enhance their catalytic efficiency and selectivity. At reduced dimensions, nanoparticles exhibit altered electronic structures, facilitating reaction mechanisms by lowering activation energy barriers. Catalytic properties of nanoparticles are strongly influenced by their size, shape, composition, oxidation states, and support materials. Bimetallic or alloy nanoparticles frequently exhibit superior catalytic performance,

demonstrating enhanced reaction rates, greater selectivity, and improved resistance to catalyst poisoning compared to monometallic nanoparticles. Such attributes are critical in industrial catalytic processes, environmental remediation, and energy conversion technologies [41, 42, 43].

#### 1.2.3.7. Characterization Techniques

Characterizing the physiochemical properties of nanoparticles involves employing sophisticated methodologies, including electron microscopy techniques such as SEM and TEM. These techniques provide detailed insights into the size, morphology, crystallinity, and structural composition of nanoparticles. Dynamic light scattering (DLS) and nanoparticle tracking analysis (NTA) offer complementary approaches to measuring nanoparticle size distribution and aggregation states. Additionally, spectroscopic techniques like X-ray diffraction (XRD), energy-dispersive X-ray spectroscopy (EDX), X-ray photo-electron spectroscopy (XPS), and Fourier-transform infrared spectroscopy (FTIR) enable comprehensive characterization of chemical composition, oxidation states, surface charge, and functional groups. These detailed characterizations are indispensable for correlating nanoparticle properties with their specific applications [44, 45, 46, 47].

#### 1.2.4. Applications

#### 1.2.4.1. Industrial Applications

Nanoparticles have already found a wide array of uses across electronics, healthcare, chemical, cosmetics, composites and energy sectors. [48] Their size- and structure-dependent properties enable lighter, stronger and multifunctional materials, often delivering performance unattainable with their bulk counterparts [49]. Key industrial applications include:

#### 1.2.4.1.1. Surface coatings and corrosion protection.

Engineered nanoparticle-enhanced epoxy coatings resist biofouling, salt-water corrosion and temperature cycling on ships and offshore platforms. By functionalising ZnO or SiO<sub>2</sub> nanoparticles for compatibility with epoxy resins, AIMPLAS demonstrated coatings that after 45 days in simulated seawater showed virtually no algal attachment or pitting, versus severe degradation on uncoated controls [50].

#### 1.2.4.1.2. Smart textiles and heating elements.

Multi-walled carbon nanotubes (MWCNTs) dispersed in acrylic binders deposit evenly on polyester–cotton substrates to yield flexible, homogeneous heating elements. CTAG's prototype auto-heating seat reaches a 30 °C rise under safe voltages, with no loss of fabric comfort or rigidity [51].

#### 1.2.4.1.3. Water treatment via photocatalysis.

Nano-TiO $_2$  provides highly efficient photocatalytic degradation of textile azo-dyes, achieving 100 % decolourization and up to 75 % TOC (Total Organic Carbon) removal under UV (and even sunlight) within 2 hours. A decrease in TOC indicates the effective breakdown of organic contaminants during treatments such as photocatalysis [52].

#### 1.2.4.1.4. De-icing and thermal management.

Conductive polymer–nanoparticle paints (e.g. polyaniline-based) can be spray-applied to aircraft leading edges. Joule heating under mild voltages melts ice at -15 °C ambient within minutes, with surface temperatures approaching +15 °C, all without heavy wiring harnesses [53].

#### 1.2.4.1.5. Micro-cavity tooling and wear resistance.

Hot-filament CVD of nanocrystalline diamond (100 nm grains) onto CrN-interlayered steel inserts yields coatings with extreme hardness, low friction and excellent thermal conductivity. In micro-injection moulding these coatings buffer heat-transfer spikes and reduce tool wear, improving both part fidelity and tool life [54].

#### 1.2.4.2. Biomedical and Biological Applications

Biological systems operate at dimensions comparable to nanoparticles (5-100 nm), unlocking uses in imaging, therapy, diagnostics and tissue engineering [55, 56]. Major application areas include:

#### 1.2.4.2.1. Fluorescent biological labels.

Semiconductor quantum dots (QDs) provide size-tunable, narrow-band emission far more photostable than organic dyes [57, 58, 59]. By controlling QD size and surface coatings, multiplexed imaging across six distinct colours and ten intensity levels permits over 10<sup>6</sup> unique optical barcodes for high-throughput assays.

#### 1.2.4.2.2. Drug and gene delivery.

Polymeric and lipid nanoparticles are engineered to carry therapeutic payloads across biological barriers. For example, poly(butylcyanoacrylate) NPs coated with surfactants cross the blood-brain barrier for CNS drug delivery [60, 61].

#### 1.2.4.2.3. Pathogen and protein detection.

Magnetic nanoparticle-antibody conjugates enable rapid immunomagnetic separation of bacteria and cells [62], while gold-oligonucleotide-Raman dye probes amplify protein detection via surface-enhanced Raman scattering with no cross-reactivity [63].

#### 1.2.4.2.4. DNA probing and structural studies.

CdTe QD luminescence reports oligonucleotide conformation (straight, bent, kinked) at singlemolecule resolution, offering new insights into DNA mechanics [64].

#### 1.2.4.2.5. Tissue engineering and implants.

Nano-textured surfaces (60-100 nm features) on hip and dental implants stimulate osteoblast adhesion and growth, reducing fibrous encapsulation and improving osseointegration [65, 661.

#### 1.2.4.2.6. Cancer therapy and hyperthermia.

Porous Ormosil nanoparticles encapsulate photosensitisers for photodynamic therapy, preventing off-target dye migration while allowing oxygen diffusion for efficient tumour cell killing [67]. Magnetic liposome-nanoparticles generate local hyperthermia under alternating fields for selective tumour ablation [68].

#### 1.2.4.2.7. Separation, purification and MRI contrast enhancement.

Dextran-coated ultrasmall superparamagnetic iron oxides (USPIOs) enhance MRI contrast [69], while ferromagnetic iron-dextran beads enable high-purity cell isolation in microfluidic platforms [62].

#### 1.2.4.2.8. Phagokinetic and cell motility studies.

Quantum-dot imaging of phagokinetic tracks elucidates metastatic potential and cell motility patterns on biomaterial surfaces [70].

# 1.3. Nano-particle Characterization and Classification Techniques

#### 1.3.1. Nano-particle Characterization and Classification Techniques

Nanoparticle characterization is critical to understanding the physicochemical properties that dictate functionality in applications ranging from catalysis to biomedicine. Metallic nanoparticles (MNPs), in particular gold, silver, and platinum nanosystems, exhibit size-, shape-, and composition-dependent optical, electronic, and catalytic behaviors [71, 72].

However, a comprehensive characterization strategy often requires combining multiple techniques to capture complementary information on morphology, size distribution, surface chemistry, and crystallinity [73].

This subsection reviews the principal techniques for nanoparticle analysis, with emphasis on metallic systems while also covering broader nanoparticle classes. We discuss the operating principles, experimental workflows, analytical outputs, and practical considerations including capital and operating costs.

#### 1.3.1.1. Imaging Techniques

#### 1.3.1.1.1 Transmission Electron Microscopy (TEM)

TEM provides high-resolution images ( $< 0.1 \,\mathrm{nm}$ ) by transmitting an electron beam through an ultrathin sample [74]. Sample preparation involves drop-casting a dilute nanoparticle suspension on a carbon-coated copper grid, followed by solvent evaporation.

Contrast arises from differences in electron scattering cross-sections, allowing direct visualization of shape anisotropy in crystalline MNPs [74]. However, TEM suffers from limited statistical sampling (tens to hundreds of particles per image) and potential beam-induced damage in sensitive materials. Capital cost for a modern field-emission TEM is in the range of  $800\,000\,\mbox{e}-1\,500\,000\,\mbox{e}$ , with annual maintenance and operation costs around  $50\,000\,\mbox{e}-1\,00\,000\,\mbox{e}$  [75].

#### 1.3.1.1.2. Scanning Electron Microscopy (SEM)

SEM images surface topography by scanning a focused electron beam and detecting secondary electrons. While resolution ( $\sim 1\,\mathrm{nm} - 5\,\mathrm{nm}$ ) is lower than TEM, SEM excels at bulk imaging over larger fields of view (tens of microns) and 3D-like contrast [76]. Conductive coating or low-voltage operation is necessary to mitigate charging in non-metallic nanoparticles.

Modern field-emission SEM instruments cost approximately  $300\,000$  € $-600\,000$  €, with annual operating costs around  $30\,000$  € [76]. SEM cannot directly resolve internal crystallinity or lattice defects.

#### 1.3.1.1.3. Atomic Force Microscopy (AFM)

AFM probes surface topography by rastering a sharp tip over the sample, measuring cantilever deflection to generate height profiles with  $\sim 0.1\,\mathrm{nm}$  vertical resolution [77]. AFM can characterize nanoparticles on insulating substrates without vacuum, enabling in-liquid imaging for biological NPs.

Limitations include tip convolution effects that distort lateral dimensions and slow scan rates ( $\sim$  minutes per image) [77]. AFM systems cost approximately 200 000  $\in$ , with moderate annual costs (around 10 000  $\in$ ) for tips and maintenance.

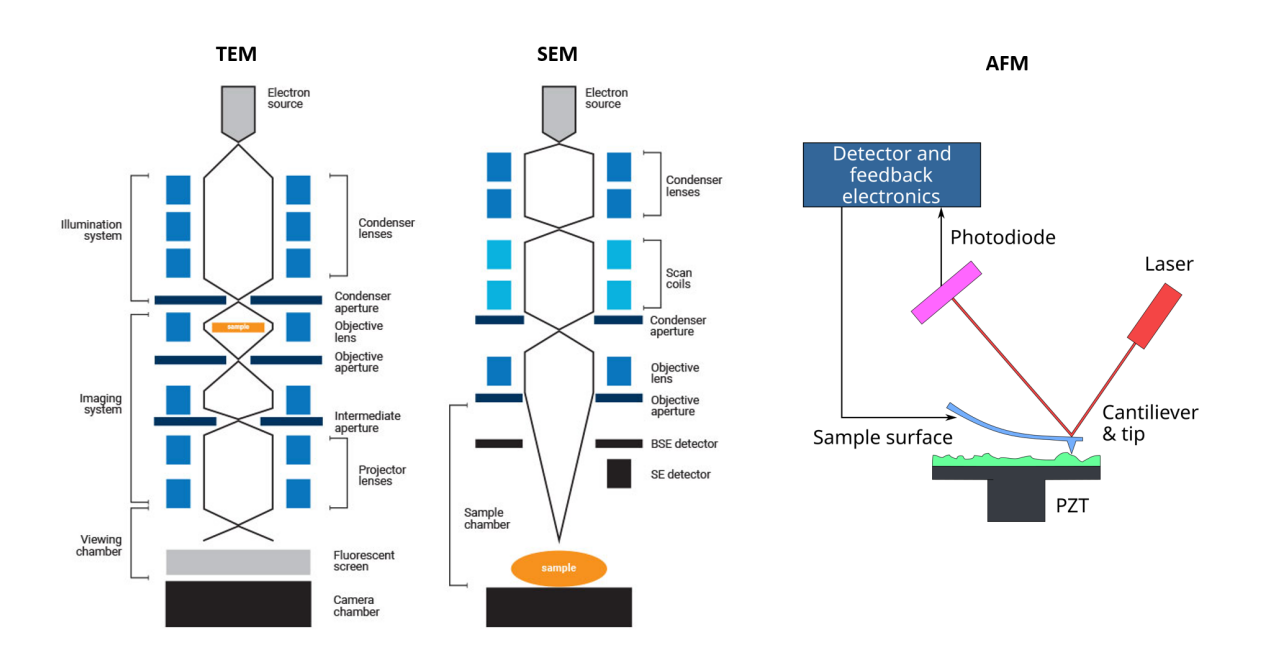


Figure 1.2. Imaging Techniques.

#### 1.3.1.2. Spectroscopic and Scattering Techniques

#### 1.3.1.2.1. Dynamic Light Scattering (DLS)

DLS measures the temporal fluctuations of scattered light intensity due to Brownian motion, yielding hydrodynamic diameter distributions [73]. It provides ensemble-averaged size with high throughput (measurements in minutes) but assumes spherical geometry and is sensitive to aggregates and polydispersity [73]. DLS instruments range from  $30\,000\,\mbox{e}-70\,000\,\mbox{e}$ , with minimal consumables.

#### 1.3.1.2.2. UV-Visible Spectroscopy

Localized surface plasmon resonance (LSPR) peaks of metallic nanoparticles produce size-and composition-dependent absorption bands (e.g., gold NPs at  $\sim 520\,\mathrm{nm}$ ) [78]. UV–Vis spectrophotometers (10 000  $\in$  –30 000  $\in$ ) offer rapid, non-destructive assays, but spectral deconvolution is required for polydisperse or complex mixtures. Organic and dielectric NPs lack plasmonic signals and thus require complementary methods.

#### 1.3.1.2.3. X-ray Diffraction (XRD)

XRD analyzes crystalline structure by measuring Bragg diffraction of X-rays from lattice planes. Scherrer analysis provides average crystallite size, while phase identification confirms composition [79]. XRD is ensemble-based (mg-scale samples), with capital costs around  $150\,000 \in -300\,000 \in$  and operating costs mainly for X-ray tubes and filters (approximately  $5000 \in /$ year). Limited sensitivity to amorphous coatings and small ( $< 3\,\mathrm{nm}$ ) particles reduces applicability to ultrasmall NPs.

#### 1.3.1.2.4. Raman and Fourier-Transform Infrared Spectroscopy (FTIR)

Surface-enhanced Raman scattering (SERS) on metallic NPs yields molecular fingerprinting of surface ligands with high sensitivity [80], while FTIR characterizes functional groups on nanoparticle surfaces [81]. Both techniques cost  $50\,000\,\mbox{\leqslant}-100\,000\,\mbox{\leqslant}$ , with consumables (IR cells, substrates) around  $2000\,\mbox{\leqslant}/\mbox{year}$ . SERS requires careful substrate preparation and reproducibility challenges.

#### 1.3.1.2.5. Energy-Dispersive X-ray Spectroscopy (EDX)

Coupled to TEM/SEM, EDX provides elemental composition mapping via characteristic X-ray emission [74]. Spatial resolution ranges from  $\sim 1\,\mathrm{nm}$  in TEM to  $\sim 1\,\mu\mathrm{m}$  in SEM. Limitations include detection limits ( $\sim 0.1\,\mathrm{wt}\%$ ) and peak overlap for neighboring elements. No additional capital cost beyond TEM/SEM, but requires detector maintenance (around  $10\,000\,\mathrm{e/year}$ ).

#### 1.3.1.3. Size Distribution and Surface Charge

#### 1.3.1.3.1. Nanoparticle Tracking Analysis (NTA)

NTA tracks individual particles in Brownian motion via optical microscopy, extracting size distributions and concentration [82]. Provides number-based rather than intensity-weighted distributions, but lower throughput and operator bias in threshold settings. Instruments cost approximately  $80\,000\,$  €.

#### 1.3.1.3.2. Zeta Potential Measurements

Electrophoretic light scattering yields zeta potential, reflecting surface charge and colloidal stability [83]. Essential for predicting aggregation behavior in suspension. Instruments (around 40 000 €) require dilute suspensions and assume uniform surface potential.

#### 1.3.1.4. Scanning Electron Microscopy (SEM)

Scanning Electron Microscopy (SEM) is one of the most versatile and widely used techniques for nanoparticle characterization, particularly for metallic systems. By rastering a focused electron beam across a sample and detecting emitted electrons, SEM provides high-resolution topographic, compositional, and crystallographic information over large fields of view [76, 84]. In this section we delve into the principles of operation, instrumentation components, imaging modes, sample preparation workflows, analytical outputs, and practical considerations including throughput, resolution limits, and costs.

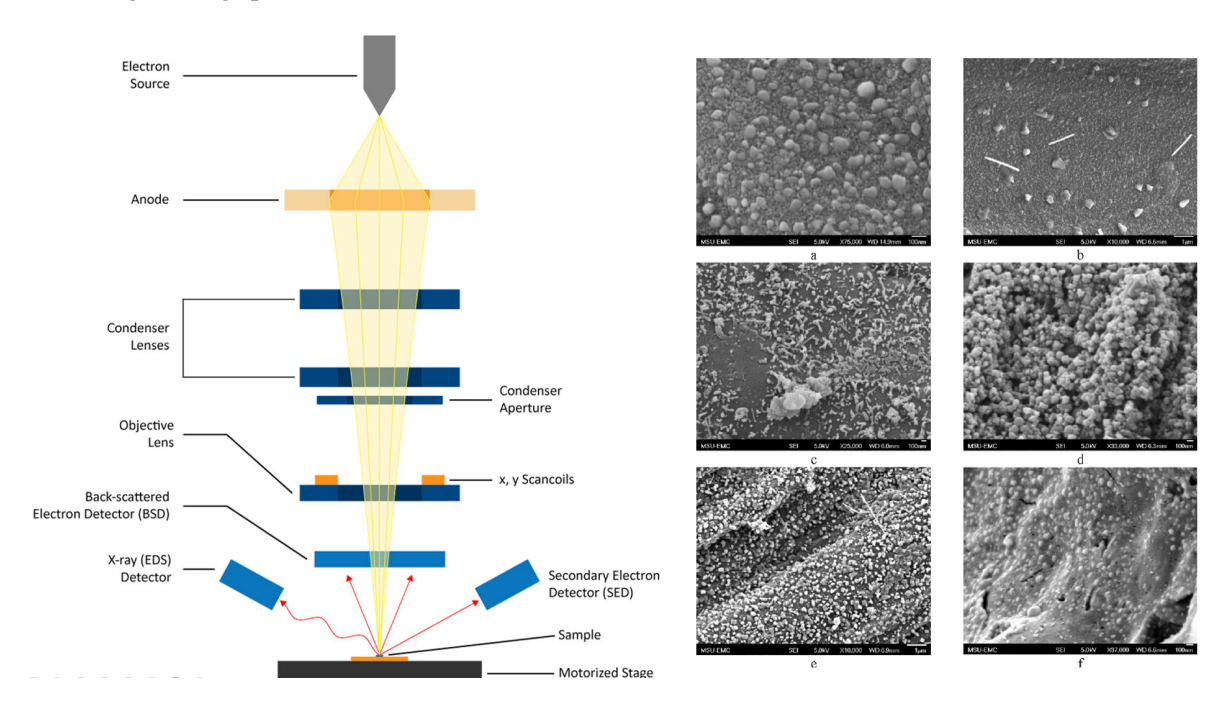


Figure 1.3. (left) Scanning Electron Microscope (right) SEM Image

#### 1.3.1.4.1. Principle of Operation

In SEM, a thermionic or field-emission electron gun provides a beam of electrons accelerated to energies between 0.5 kV–30 kV. The beam is focused by electromagnetic lenses and scanned in a raster pattern over the sample surface. Interactions between primary electrons and the specimen generate several signals:

- **Secondary electrons (SE):** Low-energy (< 50 eV) electrons emitted from the top few nanometers of the surface, providing high-contrast topographic images with lateral resolution down to 1 nm [84].
- Backscattered electrons (BSE): High-energy electrons reflected by elastic scattering; contrast scales with atomic number (*Z*), enabling compositional imaging of metallic nanoparticles against lower-*Z* substrates [76].
- **X-rays (EDS):** Characteristic X-rays emitted upon electron-shell ionization; collected by an energy-dispersive spectrometer for elemental mapping [76].

#### 1.3.1.4.2. Instrumentation and Detectors

Modern SEMs employ a field-emission gun (FEG) for sub-nanometer probe sizes, vacuum chambers adjustable between high ( $< 1 \cdot 10^{-6} \, \mathrm{Pa}$ ) and variable pressure (1 Pa) modes [85]. Key components include aperture and stigmator assemblies for beam shaping, objective lenses for focusing, scan coils for beam deflection, and multiple detectors:

- Everhart–Thornley SE detector: A scintillator-photomultiplier system optimized for SE collection.
- **Solid-state BSE detector:** Semiconductor diode array offering faster signal and compositional contrast.
- **In-column detectors:** Position below the pole piece for high-efficiency SE collection and enhanced resolution in FEG-SEMs [84].
- EDS detector: Silicon drift detector (SDD) with energy resolution  $\sim 130\,\mathrm{eV}$ , enabling rapid elemental mapping.

Capital investment for a state-of-the-art FEG-SEM with EDS and variable-pressure capability ranges from  $300\,000$  € $-700\,000$  €. Annual service contracts, cryo-pumps, detectors' maintenance, and consumables (stubs, carbon/tungsten tape, conductive coatings) add approximately  $25\,000$  € $-40\,000$  € to operating costs.

#### 1.3.1.4.3. Sample Preparation

Accurate imaging of metallic nanoparticles demands meticulous preparation:

- 1. **Deposition:** Drop-cast or spin-coat a dilute NP suspension on conductive substrates (carbon-coated stubs, silicon wafers).
- 2. **Drying:** Gentle drying under inert gas or vacuum to prevent aggregation and coffee-ring effects.
- 3. **Coating (if needed):** For non-conductive matrices or biological samples, sputter-coat with a 2 nm–5 nm layer of gold or platinum to mitigate charging; may obscure sub-5 nm features [76].
- 4. **Low-vacuum/Variable-pressure mode:** For uncoated samples, operate at 10 Pa–50 Pa water vapor or nitrogen to neutralize charge without coating [85].

#### 1.3.1.4.4. Imaging Modes and Analytical Workflows

Plan-view imaging is performed using standard SE imaging at 5 kV-15 kV to measure particle size, shape distributions, and surface assemblies (Fig. ??). Tilted-view and stereo-pair approaches involve dual-axis tilting to reconstruct the three-dimensional morphology of anisotropic nanoparticles [84]. BSE mapping provides qualitative information on alloy composition or core-shell contrast in bimetallic NPs (e.g., Au@Ag core-shell) when operated

at 20 kV–30 kV. Finally, EDS spectral imaging entails automated mapping across regions of interest with a pixel dwell time of approximately 1 ms to quantify elemental distribution and detect trace impurities (< 0.1 wt%).

#### 1.3.1.4.5. Resolution, Throughput, and Limitations

Spatial resolution can reach down to 1 nm in SE mode (FEG-SEM), though beam–sample interactions (interaction volume  $< 50 \,\mathrm{nm}$  at  $15 \,\mathrm{kV}$ ) and coating layers may degrade true resolution [84]. Throughput is limited by typical raster scans ( $1024 \times 768$  pixels), which require  $30 \,\mathrm{s}{-}120 \,\mathrm{s}$  per frame; automated stage and gallery loading can increase sample throughput but necessitate scripting [76]. Prolonged exposure can induce carbon buildup and sintering in metallic nanoparticles; using low-kV imaging ( $< 5 \,\mathrm{kV}$ ) and intermittent beam blanking helps mitigate beam damage and contamination [85]. In terms of cost, although SEM operating expenses are lower than TEM, the total cost per hour of instrument time (including amortization and staffing) is approximately 50 €-100 €, depending on regional and facility overhead [76].

#### 1.3.1.4.6. Summary of Advantages and Limitations for Metallic Nanoparticles

SEM offers high-resolution surface imaging over large fields (µm–mm scale) and provides compositional contrast via BSE and EDS without destructive sectioning. It also supports flexible sample environments, including high-vacuum, variable pressure, and cryo-SEM modes. However, true sub-nanometer resolution is limited by electron–sample interactions and coating layers, and non-conductive samples may exhibit charging artifacts that require coating or environmental SEM modes. Additionally, throughput is moderate, and quantitative image analysis demands operator expertise. Overall, SEM remains a cornerstone technique for the morphological and compositional characterization of metallic nanoparticles; when combined with complementary TEM, AFM, and spectroscopic methods, it yields critical insights into nanoparticle synthesis, assembly, and functional performance.

Technique	Advantages	Limitations / Costs
TEM	Atomic-scale resolution, direct	Low throughput; sample damage;
	morphology/crystallinity	800 000 €-1 500 000 € + 50 000 €-
		100 000 € per year
SEM	Large-area imaging; 3D-like	Lower resolution; surface only; 300 000 €–
	contrast	600 000 € + 30 000 € per year
AFM	In-liquid imaging; vertical	Tip convolution; slow; 200 000 € +
	resolution 0.1 nm	10 000 € per year
DLS	Rapid size distributions; en-	Assumes spherical; sensitive to aggregates;
	semble average	30 000 €-70 000 €
UV–Vis	Non-destructive; low cost;	Limited to plasmonic NPs; overlap in
	plasmonic sensing	peaks; 10 000 €–30 000 €
XRD	Phase identification; crystal-	Ensemble average; low for < 3 nm;
	lite size	150 000 €-300 000 €
Raman/SERS	Molecular fingerprint; high	Substrate prep; reproducibility; 50 000 €–
	sensitivity	100 000 €
EDX	Elemental mapping	Detection limits $\sim 0.1  \mathrm{wt}\%$ ; peak overlap;
		maintenance 10 000 € per year
NTA	Number-based size	Low throughput; operator bias; 80 000 €
Zeta Poten-	Surface charge; stability pre-	Assumes uniform surface; 40 000 €
tial	diction	

**Table 1.1.** Comparison of nanoparticle characterization techniques.

In summary, no single technique suffices for complete nanoparticle characterization. Metallic nanoparticles often require high-resolution imaging (TEM/SEM) combined with ensemble spectroscopic (UV-Vis, DLS) and crystallographic (XRD) analyses to fully resolve size, shape, composition, and surface properties. Emerging classification algorithms and machine learning further enhance throughput and objectivity but necessitate extensive datasets and computational infrastructure.

### 1.4. Electromagnetic Meta-materials and Resonator-based Sensors

#### 1.4.1. Introduction to Metamaterials

Metamaterials are artificially structured materials engineered to exhibit electromagnetic properties not observed in natural materials. They consist of sub-wavelength periodic inclusions (e.g., metallic resonators) that give rise to an effective medium with designed permittivity  $\epsilon_{\rm eff}$ and permeability  $\mu_{\rm eff}$  [86]. By appropriate design, metamaterials can achieve exotic phenomena such as negative refractive indices, leading to backward wave propagation and reversed Doppler or Cherenkov effects [86].

Metamaterials are typically composed of periodic unit cells much smaller than the operating wavelength. This allows them to be treated as an effective medium described by bulk parameters. For example, a metamaterial's effective refractive index can be defined as:

$$n_{\rm eff} = \sqrt{\epsilon_{\rm eff} \times \mu_{\rm eff}}$$
 (1.2)

Where  $\epsilon_{\rm eff}$  and  $\mu_{\rm eff}$  are the effective permittivity and permeability arising from the structured inclusions. By tailoring the geometry of these inclusions,  $\epsilon_{\rm eff}$  and  $\mu_{\rm eff}$  can be made to attain values not found in natural materials (including negative values) over a certain frequency band [86].

A key feature is the strong localization and enhancement of electromagnetic fields within meta-material unit cells. This field confinement provides novel opportunities to significantly boost the sensitivity and resolution of sensors [87]. As a result, metamaterials have emerged as a promising platform for next-generation sensors with high performance. Indeed, metamaterial-based sensors have demonstrated enhanced sensitivity, expanded detection range, and even new functionalities (e.g., electromagnetic "stealth" sensing) beyond the capabilities of traditional sensors [88].

Initial works in metamaterials demonstrated that arrays of metallic wires and split-ring resonators could achieve simultaneous  $\epsilon_{\rm eff} < 0$  and  $\mu_{\rm eff} < 0$ , enabling a negative index of refraction [86]. Such engineered media can bend light or other electromagnetic waves "backwards" (as seen on Figure 1.4 and realize phenomena like perfect lensing and cloaking, which sparked tremendous interest in the field.

Early meta-material research focused on novel electromagnetic capabilities (e.g., superlenses and invisibility cloaks). More recently, attention has expanded to practical applications, notably in sensing and detection. Metamaterials operate across a broad range of frequencies, from radio-frequency and microwave up to terahertz (THz) and optical regimes.

In all cases, the sub-wavelength structuring allows metamaterials to manipulate incident waves in unconventional ways, concentrating electromagnetic energy in tiny volumes (e.g.,

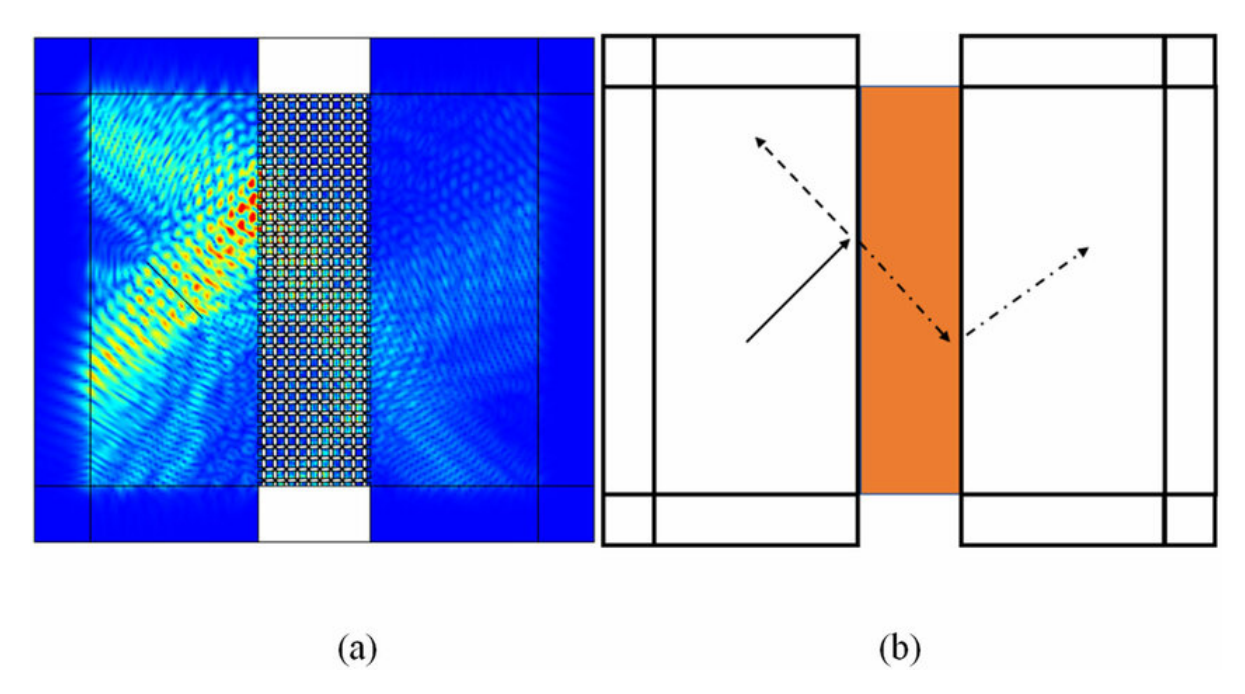


Figure 1.4. Light bending "backwards".

nanogaps) and producing high Q factor resonances. These attributes are extremely useful for sensing: a localized high field intensifies light-matter interaction, and a sharp resonance makes even small perturbations detectable as frequency or amplitude changes [87]. Therefore, metamaterial sensors can achieve greater sensitivities than traditional sensor designs.

Metamaterials and their two-dimensional counterparts, metasurfaces, have gained increasing attention as sensor platforms. Metasurfaces (ultrathin layers of patterned meta-atoms) provide similar electromagnetic control in a planar form factor, making it easier to integrate into devices. Both 3D metamaterials and 2D metasurfaces can be engineered for specific sensing tasks. They support a variety of resonant modes (electric, magnetic, or plasmonic) that respond to changes in the environment.

Figure 1.4 shows an example metamaterial structure: a periodic array of split-ring resonators on a substrate, as seen in a scanning electron microscope (SEM) image. Such resonant elements form the building blocks of many metamaterial sensors.

In summary, metamaterials offer never-before seen control over electromagnetic fields through sub-wavelength design. Features such as negative-index response, strong field confinement, and high  ${\cal Q}$  resonances make them attractive for sensor applications. Researchers have demonstrated metamaterial-based sensors for a wide range of uses, from determining material properties to detecting chemical and biological substances.

#### 1.4.2. Physical Principles of Metamaterial-Based Sensing

The operation of metamaterial sensors relies on the interaction between resonant electromagnetic modes of the metamaterial and the external stimulus (analyte, or physical quantity to be measured). In essence, a metamaterial sensor transduces a change in its environment into a measurable shift in its electromagnetic response. This typically occurs through a resonance frequency shift or a change in amplitude of a resonance.

The physical principles can be understood by modeling metamaterial elements as resonant LC circuits or antennas that are perturbed by the presence of an analyte. Considering a simple splitring resonator (SRR) which behaves like an LC resonant circuit, it has an effective inductance L

(from the current loop) and capacitance C (across the gap). An example of an approximate equivalent circuit can be seen on Figure ??. The resonant frequency  $f_0$  of this metamaterial resonator is approximately:

$$f_0 = \frac{1}{2\pi\sqrt{L_{SR}\,C_{SR}}}\,, (1.3)$$

where  $L_{SR}$  and  $C_{SR}$  are functions of the device geometry and the surrounding dielectric. When the SRR is exposed to an analyte or a change in the ambient medium, the effective capacitance  $C_{SR}$  (and possibly  $L_{SR}$ ) is modified due to the analyte's permittivity or permeability. This in turn shifts the resonance frequency to a new value  $f_0 + \Delta f$ . The sensing principle is that  $\Delta f$  correlates with the property of interest (e.g., analyte concentration or refractive index).

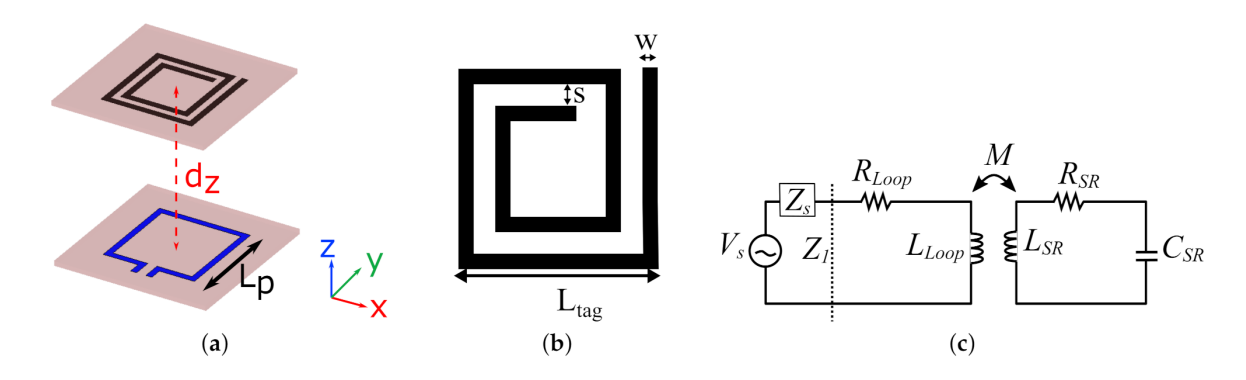


Figure 1.5. Diagram and equivalent circuit of a Square Spiral Resonator[89].

A key performance metric is the refractive index sensitivity. For resonance-based sensors, the sensitivity S is defined as the change in resonance frequency per unit change in refractive index of the surrounding medium:

$$S = \frac{\Delta f}{\Delta n},\tag{1.4}$$

often reported in units such as GHz/RIU (refractive index unit) or nm/RIU for optical wavelengths. A high S means that even a small refractive index variation (due, for example, to a thin film of analyte on the sensor) produces a large frequency shift, making it easier to detect. In practice, one measures the transmission or reflection spectrum of the metamaterial sensor (using, e.g., a network analyzer for microwaves/THz or a spectrometer for optical frequencies) and observes the resonant dip or peak shifting as the analyte is introduced.

The sensitivity of metamaterial sensors is fundamentally linked to their field distribution. Metamaterials are great at concentrating electromagnetic fields in sub-wavelength volumes. This field enhancement means that a small perturbation (a tiny volume of analyte) can induce a relatively large change in the response.

To maximize sensitivity, designers often create structures with hot spots of intense electric field where the analyte attaches. For instance, adding sharp tips or narrow gaps in a resonator concentrates the field in those regions, dramatically increasing the interaction with any dielectric loading there [87]. In essence, the more the electromagnetic field "feels" the analyte, the greater the sensor response.

Another important consideration is the quality factor (Q) of the resonance. A high-Q resonance (narrow linewidth) makes it easier to detect small frequency shifts, since the spectral feature is sharp. Metamaterial absorbers, for example, can exhibit high-Q resonance dips in transmission. By matching impedance and minimizing radiation loss, Q-factors in the tens or hundreds are achievable even in THz or optical metamaterials. However, there is an inconvenience: extremely high-Q resonances can become very narrowband and weakly coupled, potentially limiting the magnitude of the shift or requiring fine spectral resolution to detect. In practice, designers balance sensitivity and Q by evaluating the figure of merit (FOM), often defined by Equation 1.5(sensitivity divided by resonance linewidth, or similar equations) [90].

$$FOM = \frac{S}{FWHM} \tag{1.5}$$

where  $S=\Delta f/\Delta n$  quantifies the sensitivity (the frequency shift per refractive-index unit) and FWHM denotes the full-width at half-maximum of the resonance. This dimensionless ratio elegantly balances the sensor's ability to detect small refractive-index changes against its spectral linewidth, such that a higher FOM corresponds to both large signal shifts and narrow resonance features, thereby indicating higher sensing performance.

A high FOM indicates a sensor that is both sensitive and has a sharp resonance. Maximizing FOM is an ongoing design challenge, as improving S (e.g., stronger field overlap with analyte) can sometimes come at the cost of a broader linewidth (lower Q) due to increased loss or radiation.

# 1.4.3. Key Applications in Chemical, Biological, and Physical Sensing

Metamaterial sensors have been developed for a wide range of applications in the chemical, biological, and physical domains. They appear in contexts as diverse as industrial gas sensing, biomedical diagnostics, environmental monitoring, and material characterization. In all cases, the advantage of metamaterials lies in their high sensitivity and the ability to tailor them to specific sensing targets or conditions. Metamaterial-based sensors are now found in areas such as biomedical analysis, chemical processing, food quality testing, and agriculture [91]. They can operate from microwave frequencies up through the optical regime, enabling detection of phenomena across the electromagnetic spectrum [92].

In fact, the operational frequency can be chosen to suit the application: gigahertz-range metamaterials are effective for bulk material sensing (and can penetrate opaque media), terahertz metamaterials can probe molecular vibrational modes (useful for chemical identification), and optical metasurfaces offer extremely fine detection of biomolecular interactions [92].

#### 1.4.3.1. Chemical Sensing

Metamaterials have shown great promise for detecting chemical substances, including gases, liquids, and explosive or hazardous compounds. One approach is to exploit the spectral fingerprint of molecules (many chemicals have characteristic absorption lines or resonances at THz and infrared frequencies). A metamaterial sensor can be designed to enhance and detect this absorption [90].

Such sensors have been demonstrated for gases like ammonia, where an array of metamaterial resonators coated with a reactive film showed a clear THz resonance shift upon

gas exposure. In another example, a metasurface with functionalized gold resonators was used to detect volatile organic compounds via wavelength shifts in the mid-IR, corresponding to each compound's absorption features. Metamaterial chemical sensors often achieve detection limits far below the parts-per-million (ppm) level, since the strong field confinement effectively increases the interaction path length for the analyte.

They can also be made selective by tailoring the surface chemistry: for instance, coating metamaterial resonators with a thin layer that selectively absorbs a target chemical (like a certain gas) will cause a resonance shift only for that analyte. This combination of electromagnetic selectivity (via frequency targeting) and chemical selectivity (via surface functionalization) leads to powerful sensors for environmental monitoring and industrial safety.

#### 1.4.3.2. Biological Sensing

One of the most active areas for metamaterial sensors is in biology and medicine. Label-free biosensors that can detect biomolecules (DNA, proteins, viruses, etc.) in real time are of great interest. Metamaterial and plasmonic metasurface sensors perform well here by providing high sensitivity in compact, planar formats.

A common example is the plasmonic metasurface biosensor: an array of metallic nanostructures on a chip that supports surface plasmon resonances. When target biomolecules bind to the sensor surface (which is usually functionalized with a biorecognition element like an antibody or aptamer), the local refractive index near the metasurface changes, shifting the resonance condition. This can be observed as a wavelength shift or intensity change in the reflected light.

In practical biosensing setups, metamaterial chips are often integrated with microfluidic sample delivery and measured with optical methods (e.g., measuring the resonance wavelength shift with an imaging spectrometer). The label-free, real-time nature of these sensors and their compatibility with small sample volumes are major advantages for biomedical diagnostics[55].

#### 1.4.3.3. Physical Sensing

In addition to chemical and biological targets, metamaterials are employed to measure an array of physical parameters. These include temperature, pressure, strain, and the electromagnetic properties of materials. Metamaterial absorbers have been reported as high-performance sensors for temperature and pressure changes: because the resonance condition can depend on the dielectric properties of substrates or on thermal expansion, a change in temperature can produce a shift in the metamaterial's resonance frequency or a change in its absorption amplitude [91].

For instance, deformable metamaterials have been used as strain sensors: if a substrate supporting a metasurface is bent or stretched, the periodic geometry alters (changing L and C values in Equation 1.3), which can be tracked via the resonance shift. These metamaterial strain gauges can be extremely compact and can even be made stretchable for attachment to surfaces or structures.

Another important category is material characterization sensors. Here, the goal is to determine unknown properties (like permittivity, permeability or thickness) of a material under test by using the metamaterial sensor as a probe. One example is a microwave metamaterial sensor for thin-film characterization: an X-band SRR array is placed near a dielectric film, and the resonant frequency shift (or splitting) is measured to extract the film's dielectric constant and thickness. Because the metamaterial's field is strongly confined and sensitive to the presence

of the film, this approach allows nondestructive testing of films much thinner than the free-space wavelength [93].

In general, metamaterial-inspired resonators (including complementary split-ring resonators etched in waveguides or coaxial lines) have been widely used to measure the dielectric constant of liquids, powders, or solids placed in proximity. They offer high accuracy and require only a small sample volume. For instance, a microwave metamaterial sensor could distinguish different powder materials by signature shifts in an array of resonant peaks.

In all physical sensing examples, the common theme is that metamaterials provide a resonant transducer that converts a physical change into an electromagnetic signal (frequency or amplitude) that can be remotely sensed with high precision.

#### 1.4.4. Advances and Challenges

Research in metamaterial sensing has progressed rapidly in recent years. Between 2020 and 2024, significant advancements have been made both in sensor design and in integrating metamaterials into practical devices. A major trend is the shift from bulk 3D metamaterials to planar 2D metasurfaces. These ultra-thin structures can be fabricated using standard lithographic processes over large areas, making them well-suited for scalable, commercial sensors. Recent metasurface sensors use sub-wavelength nanoantennas to replicate the effects of bulk metamaterials while offering a compact form factor.

One notable development is the integration of metasurfaces with microfluidic channels, creating on-chip chemical sensors. In these devices, a small liquid sample flows over the metasurface and is analyzed in real time. Since 2020, high-sensitivity metasurface sensors have emerged that are more easily integrated with optical or electronic systems than earlier designs. This shift towards chip-scale platforms is bridging the gap between lab-based prototypes and real-world sensing technologies [92].

Another key advancement lies in tunable and reconfigurable metamaterial sensors. Traditional sensors are passive, with fixed responses defined during fabrication. Modern designs incorporate tunable elements (such as graphene, liquid crystals, or phase-change materials) to enable dynamic control. Graphene-based sensors are particularly promising: graphene supports tunable plasmonic modes in the mid-IR and THz regimes. By applying a voltage, the resonance frequency can be modified according to the user's needs [92]. This allows for active reconfiguration (such as scanning through multiple resonances to detect different analytes or compensating for baseline drift). These tunable designs introduce an additional degree of freedom: not only do they sense environmental changes, but their spectral properties can also be actively controlled. This enables multi-parameter sensing and in-situ calibration. A 2021 example includes a dualmode sensor that switches between two resonance frequencies via electrical tuning, allowing simultaneous measurement of refractive index and temperature.

Despite these advances, several challenges persist:

• Scalability: Metamaterials operating at optical frequencies require precise nanoscale features over large areas. Techniques like electron-beam lithography offer high resolution but are slow and costly, limiting scalability. Alternative methods like nanoimprint lithography and roll-to-roll printing show promise, but issues such as yield and uniformity remain. Additionally, the use of expensive noble metals (e.g., gold, silver) poses cost barriers for disposable sensors.

- **Reproducibility:** Even minor fabrication variations can shift resonance frequencies or degrade Q-factors, complicating sensor calibration. Reliable manufacturing processes or built-in calibration schemes are needed to ensure consistency across sensor batches.
- Narrow bandwidth: This is inherent to resonant metamaterials. While this allows for high sensitivity, it restricts each sensor to a specific frequency or analyte.

# 2 Sensing

### 2.1. Sensor Design Motivation and Context

Nanoparticles (NPs) exhibit unique properties that make them valuable in applications ranging from sensor coatings to biochemical detection. However, characterizing NP size and distribution typically requires time-consuming and complex instrumentation.

Traditional methods such as electron microscopy (scanning or transmission) provide direct imaging of particle dimensions but involve lengthy sample preparation and analysis [94]. Other techniques like dynamic light scattering rely on Brownian motion to infer particle size distributions, yet they often demand elaborate setups and still face limitations in throughput [94, 4]. An alternative approach is to analyze NP sedimentation behavior in a fluid, since the mix of gravity and diffusion during sedimentation is influenced by particle size and density. By monitoring how NPs settle over time (their sedimentation profile), one can potentially estimate these characteristics when combined with appropriate modeling [4]. Unfortunately, many conventional characterization protocols require significant manual intervention and long wait times between fabrication and measurement steps. This creates a need for faster, analysis techniques that minimize sample usage and accelerate feedback in nanoparticle production [4].

Honrrubia et al.'s work [95] addresses that need by introducing a microwave planar resonator sensor designed to continuously monitor NP sedimentation. Microwave resonator sensors (particularly those based on split-ring resonators (SRRs) and related structures) offer a flexible, method to characterize materials through their dielectric properties [3]. The general principle is that the resonator acts as an LC circuit with a high Q-factor; when a material is brought into the near field of the resonator, it modifies the effective capacitance and therefore shifts the resonant frequency [3]. The magnitude of the frequency shift depends on the permittivity and volume of the material interacting with the sensor: materials with higher dielectric constant cause larger downward shifts in the resonance frequency [3]. By designing the resonator appropriately, one can target a specific frequency range and tailor the sensitivity for a given application [7]. Spiral resonator designs are especially attractive because they achieve a longer resonant path within a compact area, yielding potentially higher Q-factor and sensitivity [5]. Planar resonator sensors have already shown promise for thin-film dielectric measurements, since miniaturized resonators confine electromagnetic fields in a small volume near the sensor surface [96].

In this context, a square spiral resonator (SSR) sensor is proposed to monitor nanoparticle sedimentation profiles in real time. The idea is that as NPs dispersed in a fluid settle onto the sensor surface, they form an accumulating layer in the sensor's sensing volume (the region of the electromagnetic near-field above the resonator).

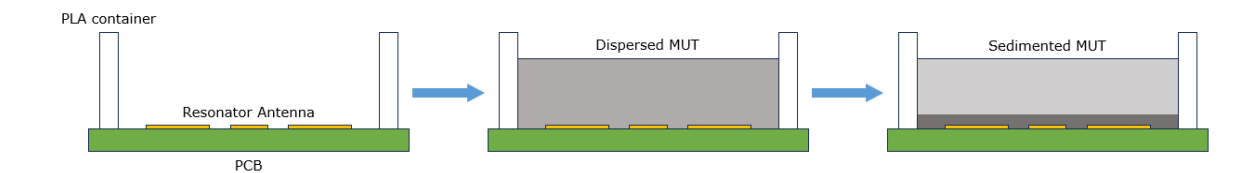


**Figure 2.1.** Diagram showing the measurement process of the MUT. First (left) the SSR and container are cleaned and all liquid and solid residues are removed, leaving the container and the PCB with the resonator antenna ready for measurement; Second (center), the dispersed MUT is poured inside the PLA container; Lastly (right), as time passes, the dispersed NPs will sediment over the PCB, leading to a measurable shift in the resonance frequency of the MUT.

This progressive deposition leads to a continuous change in the sensor's effective capacitance and hence a time-dependent shift in its resonance frequency[1]. The process is illustrated conceptually in Figure 2.1. Initially, the resonator is exposed to the NP dispersion (with particles distributed throughout the fluid). Over time, gravity causes NPs to migrate and concentrate near the bottom, eventually forming a uniform layer on the sensor. Once a significant layer has formed and the local NP concentration in the sensing region reaches an equilibrium, the resonance frequency stabilizes at a new value. The difference between the initial and final resonance frequencies (and the time taken to reach equilibrium) provides a "sedimentation profile" characteristic of the nanoparticle type and concentration. For a theoretical description of this phenomenon, one can employ the Mason–Weaver equation to model the NP concentration c(x,t) along the vertical direction x over time t [97]. This model combines diffusion (Brownian motion) and gravitational drift in one dimension:

$$\frac{\partial c}{\partial t} = D \frac{\partial^2 c}{\partial x^2} + v \frac{\partial c}{\partial x},\tag{2.1}$$

where D is the diffusion coefficient and v is the settling velocity. These parameters depend on particle characteristics (e.g.,  $D=k_BT/F$  relates to thermal energy and friction, while v is proportional to the buoyant mass of the particle) [97]. The Mason–Weaver model predicts that the particle concentration at the bottom (on the sensor surface) will asymptotically approach a steady value, often in an exponential-like fashion with a characteristic time constant. By capturing the sensor's resonant frequency as a function of time, we essentially measure the integral effect of this concentration build-up in the sensor's near field.

The result is a sedimentation profile curve that can be analyzed to extract meaningful parameters (such as the time constant of sedimentation and the final frequency shift) which correlate with NP properties. Thus, the SSR sensor provides a novel route to rapidly characterize nanoparticles via their sedimentation dynamics, using a simple electrical measurement instead of elaborate microscopy or optical methods[2].

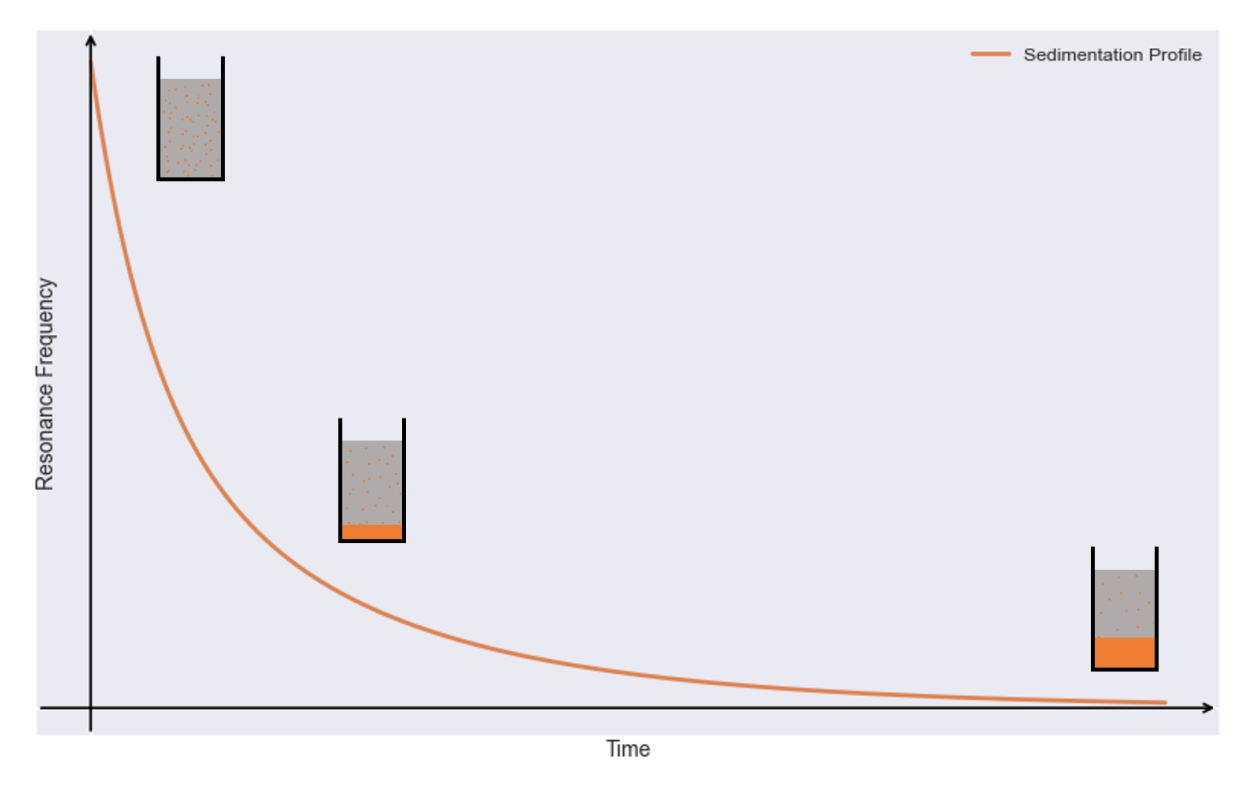


**Figure 2.2.** Conceptual diagram of the sedimentation process as sensed by the SSR sensor. Nanoparticles initially dispersed in the fluid (top) gradually settle under gravity and form a layer on the sensor surface (bottom). x-axis represents time while y-axis represent the peak of the resonance frequency measured by the VNA.

## 2.2. Electromagnetic Modeling and Design Methodology

The sedimentation sensor is based on a planar Square Spiral Resonator structure that is electromagnetically coupled to a feed transmission line. The SSR geometry was chosen to achieve a target resonant frequency in the microwave range (on the order of a few gigahertz) while maintaining a compact footprint. The resonator consists of a square spiral trace etched in copper on a dielectric substrate, forming a planar inductor-capacitor (LC) circuit. Each turn of the spiral contributes inductance, while the gaps between adjacent turns and between the spiral and ground plane contribute distributed capacitance. For the design, as discussed in [95], a standard FR4 printed circuit board (PCB) was used as the substrate due to its low cost and ease of fabrication. The substrate has a thickness of 1.5 mm and a relative permittivity of approximately 4.5, which influences the electromagnetic field distribution and the base resonant frequency of the spiral. A microstrip transmission line (TL) on the same PCB layer is used to excite the resonator: the TL runs adjacent to the spiral and serves as a feed that inductively (magnetically) couples energy into the spiral resonator. When the device is connected to a vector network analyzer (VNA) in reflection mode, the spirals produce a notch (dip) in the reflected signal ( $S_{11}$ ) at their resonant frequency.

To optimize the sensor design, electromagnetic (EM) simulations were carried out using a full-wave solver. The layout was modeled with two identical square spiral resonators placed symmetrically on either side of a central microstrip line. This dual-resonator configuration was adopted because it produces a more pronounced resonance (a deeper notch in  $S_{11}$ ) compared to a single resonator [98]. Each spiral in the final design has an outer side length of  $l_{\rm sp}=5.06$  mm and a trace width  $w_{\rm sp}$  equal to the gap between turns (also 5.06 mm overall outer size with a single-turn gap of d=0.44 mm).

These dimensions were tuned such that, in simulation, the resonant frequency in absence of any nanoparticles (with the spirals in air above the substrate) is approximately 2.44 GHz. The microstrip feed line is 2.82 mm wide, chosen to match a 50  $\Omega$  characteristic impedance on FR4. It traverses the PCB and passes between the two spiral resonators, with a small gap of d=0.44 mm separating the line from each spiral's inner end. This gap distance controls the coupling strength between the line and the resonators; matching it to the spiral gap ensured symmetric coupling and helped achieve a good impedance match at the resonant frequency. The PCB ground plane on the back side provides the return path for the microstrip and forms the reference for the spiral's capacitance.

Using the EM solver, the sensor's frequency response was simulated under various conditions to validate the design and understand its sensing behavior. Figure 2.3 shows the top-view layout of the SSR sensor as implemented. In simulation, the device exhibits a clear reflection notch around 2.44 GHz when the spirals are in vacuum (or air). The electromagnetic fields are strongly confined around the spiral traces and in the gap regions. Notably, a significant portion of the electric field extends a short distance above the PCB in the vicinity of the spirals — this is the sensing volume where the presence of any material (with dielectric constant different from air) will perturb the resonant frequency. To demonstrate this principle, a simulation was performed with a dielectric overlayer on the sensor to mimic the effect of deposited nanoparticles. In one scenario, a homogeneous material layer (representing, for instance, a liquid or solid covering) with relative permittivity  $\varepsilon_r \approx 2.13$  (comparable to a hydrocarbon oil or a low-permittivity NP layer) was applied over the spirals.

The result was a downward shift in the resonant frequency from about 2.444 GHz to about 2.247 GHz, confirming that the sensor is indeed sensitive to dielectric loading as expected. In essence, the resonator's inductance is relatively fixed by its geometry, while the capacitance increases when a higher-permittivity material occupies the space near the spiral, thus reducing the frequency  $f_0 \approx \frac{1}{2\pi\sqrt{LC}}$ . This simulation outcome aligns with theoretical expectations and provides a baseline for the magnitude of frequency shift one might observe for a complete coverage of the sensor with a low- $\varepsilon$  material. Higher-permittivity or higher-volume loading would induce larger shifts, potentially at the cost of damping the resonance if the material is lossy.

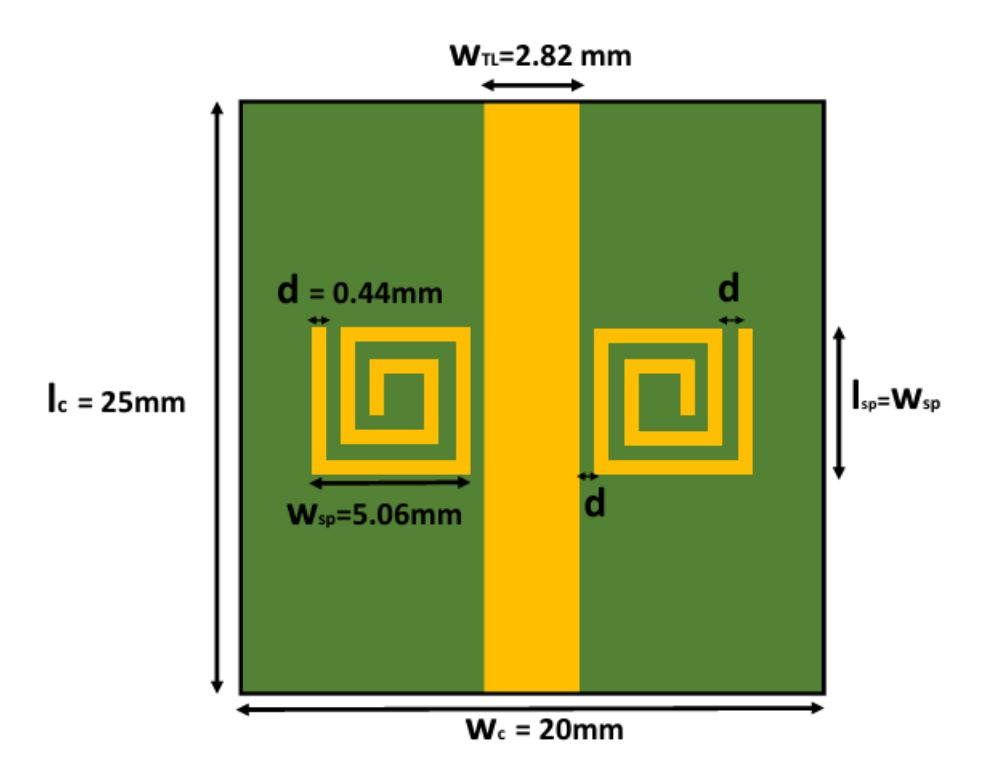


Figure 2.3. Layout of the fabricated SSR sensor.

The sensor model can be understood not only through full-wave simulations but also via an equivalent circuit representation. Each spiral resonator can be approximated as an LC tank with a certain inductance (proportional to the length of the spiral trace and the PCB's inductive coupling to ground) and capacitance (stemming from the inter-trace gaps and the capacitance to the ground plane). The two coupled spirals and the feed line form a resonant network that manifests as a notch in the reflection coefficient when measured from the feed line port. Key performance parameters such as the resonant frequency  $f_0$  and quality factor Q can be extracted either from simulation or from this circuit analogy. A high Q implies a narrow and deep resonance, which is beneficial for sensing since even small shifts in frequency can be resolved. However, one must also consider that introducing a lossy sample (e.g., conductive or polar nanoparticles) will reduce the Q by absorbing energy, which could broaden the resonance and slightly reduce sensitivity. Therefore, the design aimed to maximize Q in the unloaded state to have headroom for any Q degradation once the NPs are introduced.

Another outcome of the EM modeling was insight into the spatial distribution of the sensor's sensitivity. The simulations confirm that the electric field (and thus dielectric sensitivity) is concentrated in the immediate vicinity of the spirals—roughly within a few millimeters above the PCB surface. This defines the effective sensing volume. Nanoparticles that settle into this volume will have the strongest impact on the resonant frequency, whereas particles remaining farther away (e.g., still suspended higher in the fluid) have a negligible effect. This aspect justifies the assumption in our sensing approach that the resonant frequency change over time directly corresponds to the amount of nanoparticles that have settled onto or near the sensor surface.

### 2.3. Resonator Tuning and Material Considerations

Designing the SSR sensor required careful tuning of both geometry and material parameters to meet the desired performance. The primary design goal was to place the resonant frequency in a convenient range for measurement (around 2–3 GHz) and to ensure a high sensitivity to dielectric changes due to nanoparticle deposition. Starting from initial estimates based on analytical formulas for spirals and transmission lines, the design was iteratively refined using the EM simulations described above.

The spiral side length and number of turns were the dominant factors controlling the resonance frequency: a larger spiral (longer total conductor length) lowers  $f_0$ , while a smaller spiral raises it. Likewise, the inter-turn spacing and the gap to the feed line influence the coupling and effective capacitance. A square spiral with a single turn was chosen (essentially a loop with a spiral shape) primarily for simplicity and because it allowed us to achieve the target frequency with the given substrate. More turns could increase the inductance further, but would also introduce more capacitance and potentially more loss; thus a balance was found with the one-turn square spiral of 5 mm side, which yielded  $f_0 \approx 2.4$  GHz on FR4.

Material considerations extend beyond the substrate to the nanoparticles and the dispersion medium. In our design, the medium in which NPs are dispersed is a non-polar liquid (paraffin oil) with a low relative permittivity ( $\varepsilon_{par}\approx 2.13$ ). This choice is deliberate: a low-permittivity, non-conductive host fluid has minimal initial impact on the sensor (so the baseline resonance with just the liquid is still near the designed frequency) and it ensures that the NPs do not experience any significant electrostatic stabilization (since paraffin is non-polar and does not induce surface charges on the particles). Thus, gravity is the dominant force driving sedimentation, consistent with the assumptions of the model [4].

If a polar or high- $\varepsilon$  liquid (like water) were used, the resonant frequency would shift considerably just from the liquid, and the high dielectric loading could dampen the resonance severely. Additionally, water or polar solvents often impart surface charges to particles and can lead to phenomena like electrical double layers, which would slow down or alter sedimentation behavior. By using paraffin oil, we avoid these complications. Nanoparticles in the oil essentially behave as solid particles settling due to gravity, without additional forces, which simplifies both the modeling and the interpretation of results.

Another material consideration is the construction of a physical container for the liquid sample. A small well or container is needed to hold the NP dispersion over the flat sensor during the experiment. We employed a 3D-printed rectangular container made of polylactic acid (PLA) attached to the PCB around the spirals to serve as a fluid reservoir. PLA was chosen for its chemical inertness and low microwave loss; however, it does have a moderate dielectric constant (on the order of 3).

While this container was not included in the simulation model, it introduces a slight perturbation in the experimental device. In practice, the presence of the PLA ring and the adhesive used to attach it (cyanoacrylate) can cause a small additional shift in the baseline resonance frequency (a few MHz) and a minor reduction in Q. These effects were accounted for by calibrating the measurement baseline with the container in place before adding any nanoparticles. The key point is that all fixed structures (substrate, container, etc.) remain constant between measurements, so their influence can be treated as part of the sensor's inherent baseline. The dynamic changes we observe are then purely due to the nanoparticles' sedimentation.

### 2.4. Fabrication Process and Expected Performance

The SSR sensor was fabricated using standard PCB manufacturing techniques. The design pattern (two spirals and the feed line) was transferred onto a copper-clad FR4 board and etched to define the conductive traces. The board dimensions are approximately 25 mm  $\times$  20 mm, providing ample area to include the resonators and an edge-mounted connector. A SubMiniature-A (SMA) coaxial connector was soldered to the end of the microstrip line to interface the sensor with external instrumentation (e.g., a VNA). After fabrication, the two copper spiral resonators and the microstrip line are clearly visible on the top surface, with the bottom surface being a continuous ground plane.

The fabrication tolerances (etching precision, substrate dielectric tolerance, etc.) can lead to slight deviations in the resonant frequency (on the order of a few tens of MHz). Indeed, when the sensor was first tested with no sample, its resonance in air was observed to be within a few percent of the 2.44 GHz design target, which was acceptable. Any small discrepancy can be attributed to the FR4 dielectric constant tolerance and the presence of the SMA connector and PLA container, none of which were perfectly represented in simulations. Nonetheless, the device functioned as expected, showing a sharp reflection notch in the Sparameter measurement.

After verifying the baseline operation, the next step was to integrate the sample container. A rectangular PLA well was bonded onto the PCB, centered over the spiral resonator area using a cyanoacrylate-based adhesive. The well was created by 3D printing to ensure it fit snugly and was leak-proof when glued. Once attached, the sensor could securely hold a small volume of liquid (0.1 mL–0.2 mL of dispersion) covering both spirals uniformly. This volume was sufficient to submerge the resonator area while being minimal enough to qualify as a "low-volume" test, consistent with the goal of conserving the precious nanoparticle samples.

With the complete sensor assembly, we evaluated its expected performance metrics. One important metric is the sensitivity, which in this context can be thought of as the change in resonant frequency per quantity of nanoparticles deposited. While it is challenging to express this analytically (since it depends on the complex permittivity of a growing porous NP layer), we can gauge sensitivity from the experimental results and simulations. The full coverage simulation (with a uniform dielectric layer  $\varepsilon_r\approx 2.1$  mimicking a dense layer of NPs or oil) produced a frequency shift of nearly  $\Delta f\approx 197\,\mathrm{MHz}$  (from 2.444 GHz–2.247 GHz). In practice, the final frequency shifts observed in experiments were somewhat smaller, because the nanoparticle layer that forms is not a continuous high-permittivity film but rather a layer of particles with oil filling the interstices (thus the effective permittivity of the layer is closer to that of oil plus a small increment). Nevertheless, a substantial frequency shifts were recorded on the order of tens to over a hundred MHz, depending on NP concentration. This is well

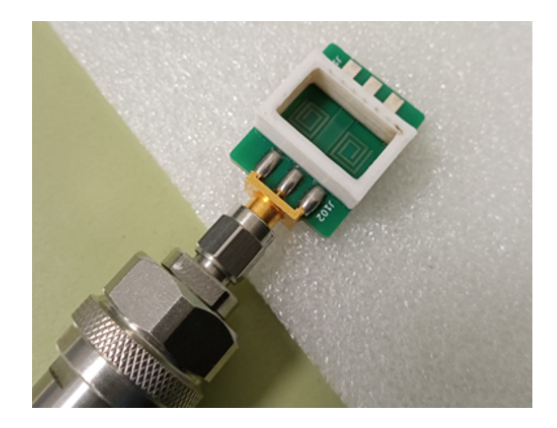
above the sensor's frequency resolution limit: the VNA measurement setup had a frequency resolution better than 1 MHz, and baseline drifts of only 3 MHz over hours were observed (due to temperature and instrument drift) [5]. Therefore, even the smallest shifts due to sedimentation were discernible above the noise floor.

Another performance parameter is the quality factor Q of the resonance during sensing. As nanoparticles accumulate, they can introduce losses (for instance, conductive losses from metallic particles or increased dielectric loss if the particles form a lossy composite). Correspondingly, we noticed a slight reduction in the depth of the  $S_{11}$  notch over time, alongside the frequency shift. However, the notch remained clearly trackable throughout the experiment, indicating the sensor maintained sufficient Q to allow frequency determination at each time point.

An expected outcome of the sedimentation experiment was that the resonant frequency would approach a stable value once sedimentation effectively completed. Indeed, across various tests, the resonance frequency versus time curves leveled off after a certain duration (on the order of a few hours). For example, in all trials the resonance stopped shifting appreciably after roughly 3 hours, implying that by that time a quasi-static NP layer had formed on the sensor surface [4].

The final frequency shift (difference between the starting frequency and the plateau frequency) correlated with the initial concentration of NPs in the dispersion. Higher concentrations produced larger shifts, as expected since more particles ultimately settled to form a thicker or denser layer. Likewise, the time required to reach the plateau (which we can associate with a sedimentation time constant) varied with particle properties: in qualitative agreement with sedimentation theory, larger or heavier particles settled faster, yielding quicker frequency decay, whereas smaller or lighter particles took longer. The ability to measure these differences is a strong validation of the sensor's effectiveness. It shows that the SSR sensor can not only detect the presence of nanoparticles but can also resolve dynamic differences in how they settle.

To further characterize the sensor's performance, we also examined its repeatability and reproducibility. Multiple runs with the same type of nanoparticles and concentration showed that the frequency vs. time profile could be reproduced with only minor variation, especially when experimental conditions (temperature, initial dispersion method, etc.) were carefully controlled. This repeatability is crucial if the sensor is to be used as a characterization tool, as it means the extracted parameters (time constant, final frequency shift) are reliable and characteristic for a given sample. Additionally, since the sensor operates in the microwave regime, the measurements are relatively immune to optical turbidity or sample opacity (an advantage over optical monitoring of sedimentation).



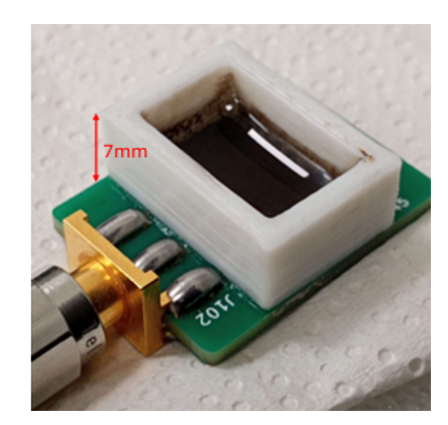


Figure 2.4. Sensor + PLA container.

## 2.5. Measurement Protocol for Sedimentation Profiling

To experimentally utilize the SSR sensor for sedimentation profiling, a well-defined measurement protocol was followed.

First, the VNA (Vector Network Analyzer), particularly, the Anritsu Shockline MS46122B, was calibrated over the frequency range of interest (2.23 GHz–2.46 GHz in our case) using a one-port calibration at the SMA connector. This calibration ensures that the subsequent reflection measurements ( $S_{11}$ ) accurately represent the sensor's response, free from systematic errors of cables and connectors. The sensor (with the empty PLA container attached) was measured to record a baseline resonance frequency. The calibration consists of four phases, which are kept standard thanks to the calibration kit by Anritsu. Firstly, the VNA is turned on and left to warm-up for 20-30 minutes. Secondly, a no-load measurement is done, later a short circuit measurement and lastly a 50  $\Omega$  load is attached. This calibration procedure guarantees a consistent and comparable output through the different measurements, eliminating any displacement due to external factors.

Once the VNA is calibrated, the nanoparticles are mixed with paraffin creating a 10 mg/mL dispersion (more details provided in Chapter 3.1). These nanoparticles are dispersed through the paraffin using a BRANSON Digital Sonifier (Figure 2.5). This sonifier, equiped with a tip narrow enough to reach the end of the test-tube will sonify the dispersion for 15 minutes. These 15 minutes are distributed in intervals of 15 s with the sonifier ON and 5 s with the sonifier OFF. Therefore, in total the sonication process spands over 20 minutes.

The sonication process is performed with the test tube containing the dispersion submerged in a water-ice bath in order to prevent it from overheating and changing the paraffin's properties. This process can be seen on Figure 2.6.

Once the sonication process is complete,  $10\,\mu L$  of the dispersion are pipetted onto the sensor. The first seconds after the sonication is complete are critical since the sedimentation curve is exponential and the largest nanoparticles will sediment the quickest, therefore, the time between the end of the sonication and the beggining of the measurement is reduced to the minimum possible.

The VNA measurements are started and the temperature of the room is recorded to guarantee that it remains constant through the measurement.



Figure 2.5. BRANSON Digital Sonifier.



**Figure 2.6.** Test tube containing paraffin and nanoparticles submerged in an ice bath with the sonicator probe, ready to start the sonication process.

Three to four hours later, as determined by [95], the measurements are stopped, thus leading to a completed iteration of one measurement.

### Measurements

### 3.1. MUT Preparation

Copper nanoparticles (Cu-NPs) were synthesized using the wire explosion method, a top-down physical fabrication technique well-suited for the production of metallic nanopowders (see Chapter 1.2.2). This method relies on the rapid vaporization of a metal conductor by the discharge of a high-voltage capacitor, leading to nanoparticle formation upon condensation in a surrounding medium.

In this study, the Cu-NPs were fabricated at the University of Pisa. The experimental setup involved cylindrical copper wires with a diameter of 1 mm and a length of 30 mm. A high-current density, ranging from  $1\cdot 10^7\,\text{A/m}^2$  to  $1\cdot 10^9\,\text{A/m}^2$ , was applied by discharging a 765  $\mu\text{F}$  capacitor charged up to 10 kV. This intense current caused adiabatic heating of the wire, leading to its explosive vaporization. The vaporized copper then condensed into nanoparticles upon interaction with a surrounding medium of distilled water, which also served to contain and collect the resulting product.

The explosion process was monitored using a dedicated voltage probe (1:1000), a calibrated Rogowski coil, and a high-bandwidth oscilloscope, ensuring precise characterization of the electrical parameters during the event. The entire environment was optimized to minimize contamination: post-explosion, the vessel and electrodes were carefully cleaned with deionized water before repeating the procedure.

To ensure reproducibility and sufficient material yield, the explosion cycle was iterated ten times. The collected suspensions were subsequently subjected to a low-temperature evaporation process to isolate the dry nanopowder. The obtained Cu-NPs were then re-dispersed in deionized water, deposited onto substrates, and analyzed via scanning and transmission electron microscopy (FEG-SEM and HR FEG-TEM) to evaluate their size distribution and morphology.

This method offers several advantages, including the ability to produce nanoparticles without the use of chemical reagents, the rapid generation of high-purity products, and the potential to fabricate complex or multicomponent nanostructures. However, challenges such as precise control over particle size and shape, as well as the potential for oxidation, remain areas for further optimization.

Following the above-mentioned method, three samples of copper nanoparticles were created. These samples were generated using different parameters, aiming to create different sized distributions of the nanoparticles. The samples (and the names A, B, C chosen for each one) can be seen on Figure 4.9.

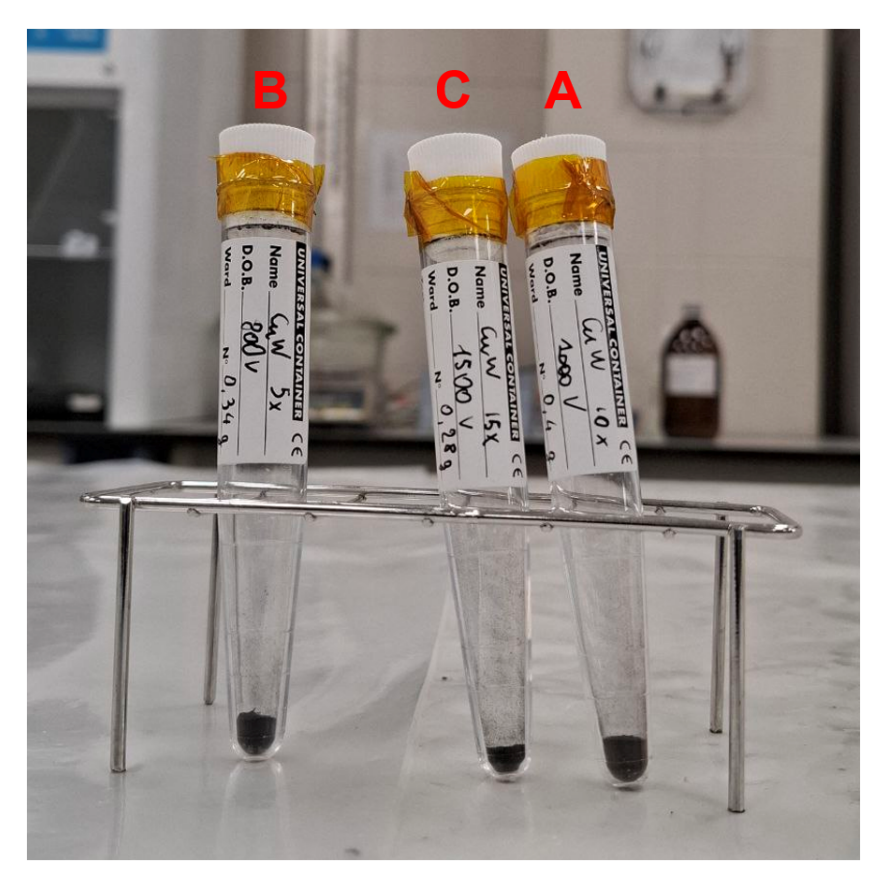


**Figure 3.1.** Three test tubes containing the three different nanoparticles, labeled A, B, C through the rest of the Thesis.

In order to measure the different sedimentation curves of the different nanoparticles, a dispersion has to be made with them. For this, pure paraffin was used as a medium in which to disperse the copper nanoparticles. The same paraffin bottle was used for all the measurements.

A concentration of 10 mg/mL was used in order to create a saturated medium in which the nanoparticles will precipitate due to gravity and sediment at the bottom of the sensor. If a non-saturated concentration was chosen, the sedimentation process would be slower and a higher percentage of nanoparticles would remain in suspension through the medium and never precipitate.

A high precision scale was used to prepare the mix of paraffin and Cu-NPs. The nanoparticles were poured in first into the test tube (Figure 3.2 and then the correct amount of paraffin was pipetted into the test tube to guarantee the desired concentration of 10 mg/mL.

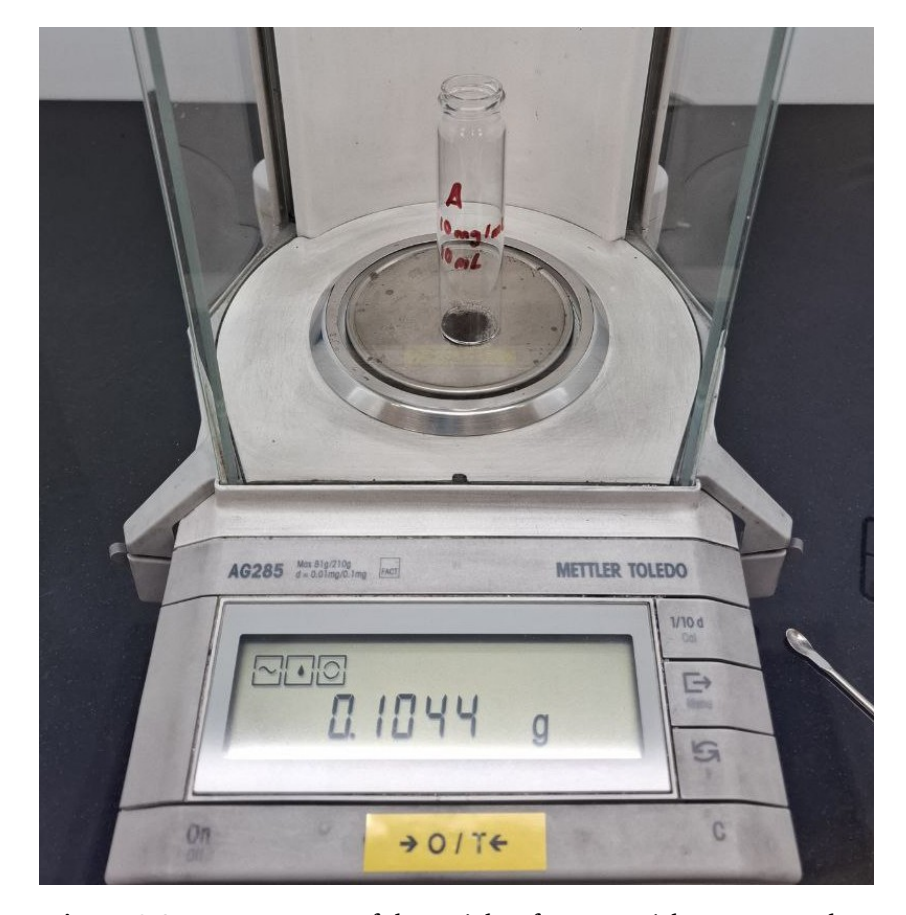


Figure 3.2. Measurement of the weight of nanoparticles per test-tube.

The result before the sonication is that shown in the left side of Figure 4.9. After the process mentioned in Section 2.5, the result should be similar to the one shown on Figure 4.9 left side.





Figure 3.3. Before (left) and after (right) the sonication process.

#### 3.2. Sonication Time Determination

In order to determine a suitable sonication time for the dispersion and avoid sonicating for an unnecessary ammount of time, an experiment was conducted. Samples of the same nanoparticle type (in this case we chose NP A, since it was the one we had more of) would be sonicated for different time intervals and their sedimentation curves would be recorded and compared.

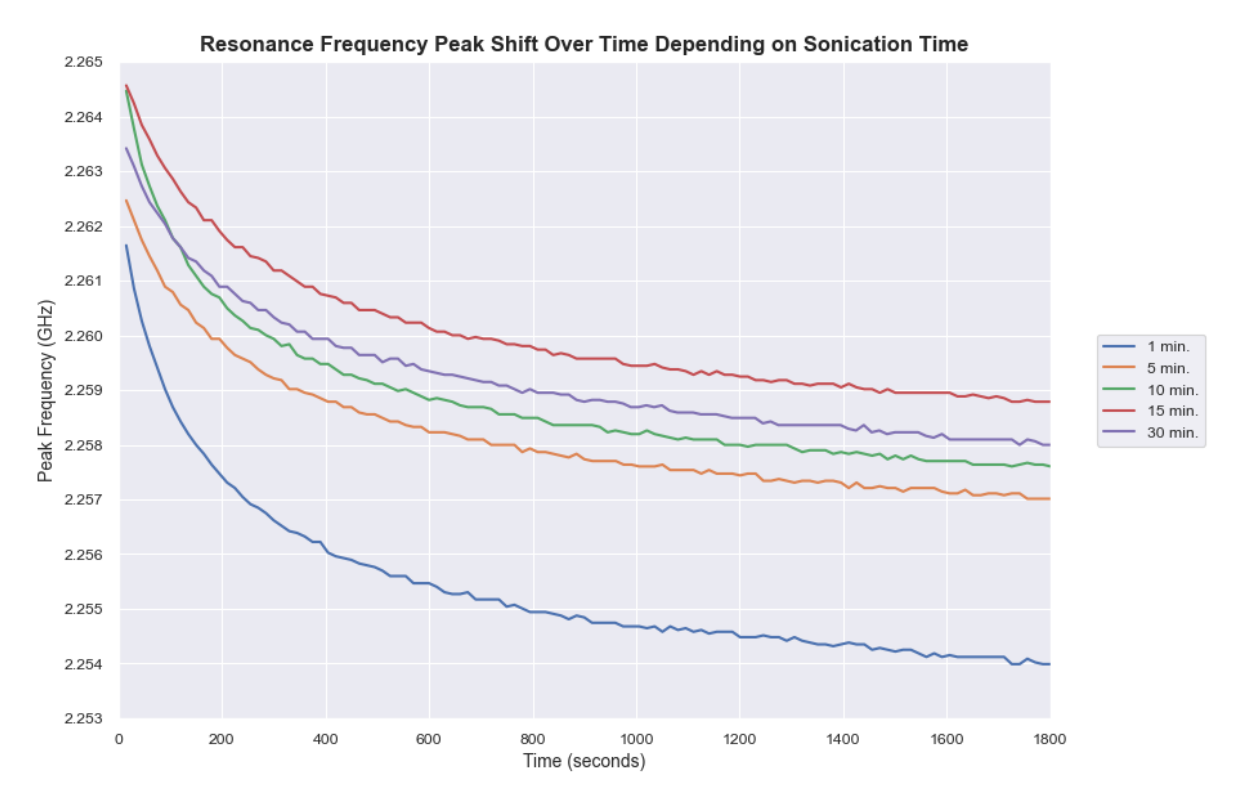


Figure 3.4. Sedimentation curves of the same dispersion during different sonication times.

As seen on Figure 4.9, the sedimentation curves keep having a slower exponential decay the longer they are sonicated until a saturation point is reached at around 15 min–30 min. At this point, the resolution of the measurement is thee key difference since the difference between both measurements (red and purple) is only  $\pm 1$  MHz (in constrast with the 5 MHz in between the 1 min and the 15 min measurements).

With this graph, we can determine that a suitable time to sonicate the dispersion would be 15 minutes, since it grants the same results as the 30 minute one and takes half the time, allowing for faster iterations of measurements.

All of the sonications performed were done in the same conditions. The sonicated test tube would have a minimum of 5 mL and a maximum of 10 mL. The test tube would be submerged inside an ice bath with the probe tip inside the test tube just barely not touching the bottom of the test tube as seen on Figure 4.9.



Figure 3.5. Test tube with nanoparticles submerged into the ice bath with the probe inside.

### 3.3. Material Differentiation

As mentioned in Chapter 1, a difference in a material's properties (permitivity, conductivity and magnetic permeability) lead to distinct shifts in a resonant sensor's response. When a planar resonator is loaded with a MUT, its resonance frequency typically shifts downwards due to the increase in the effective permittivity.

This variation can be seen on Figure 3.6. The main value of interest for this research is the resonance frequency, not so much the magnitude of the peak. We can see that there is a clear distinction between some materials (for example, air and hexane), while some other materials have more similar frequencies.

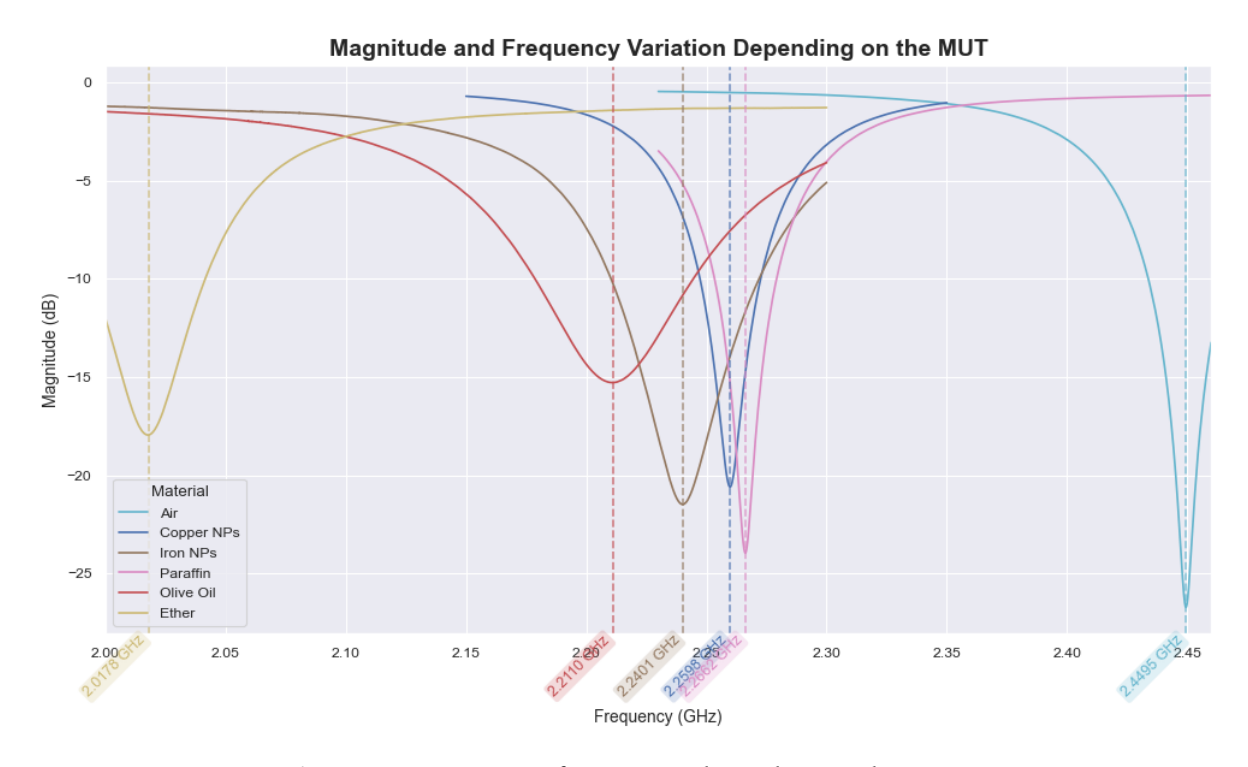


Figure 3.6. Resonance frequencies depending on the MUT.

It is important to note that both the Iron NPs and the Copper NPs are measurements performed in a paraffin dispersion, which is the reason their frequencies are slightly lower than that of the paraffin while still being quite close to it.

With the SSR and the VNA, the resolution of the measurements performed can perceive changes of less than 1 MHz in the resonance frequency, therefore a very viable application of this sensor is to classify different materials depending on their resonance frequency.

Appart from having different resonance frequency peaks at a certain common time after sonication, two dispersions of different material NPs will have different sedimentation curves. These curves depend on many factors, mainly the material, temperature, concentration and sonication times.

If we try and keep the changes to a minimum, we can reach some conclussions. As seen on Figure 3.7, even when sonicating and exposing paraffin to the same conditions as the NP dispersions, the resonance frequency does not shift significantly (the drift observed in the measurement is due to a slight temperature change in the measurement room and due to the inherent measurement error of the VNA measurement device. This error is less than 1 MHz and therefore can be ignored for our analysis.

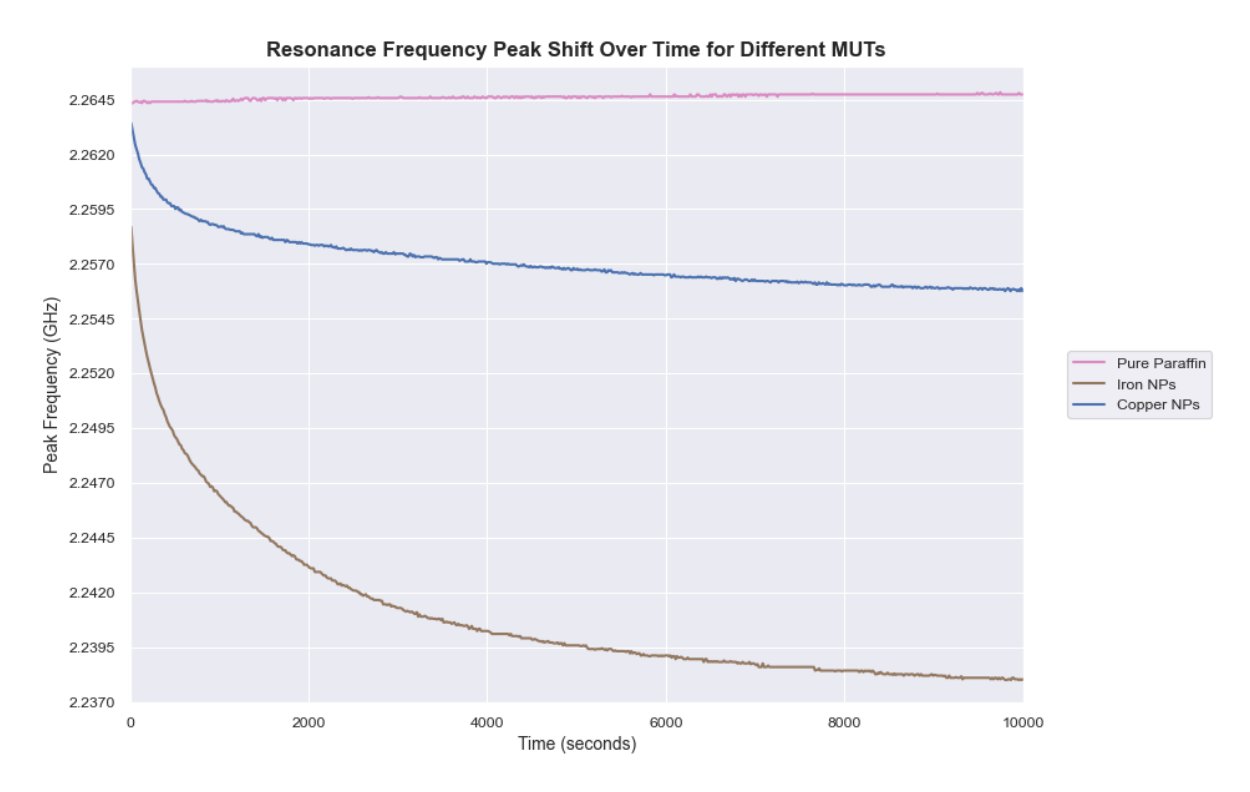


Figure 3.7. Resonance frequencies depending on the MUT.

When considering two types of metallic nanoparticles (in this case Copper and Iron), apart from a difference in any instantaneous resonance frequency peak, both sedimentation curves are different. These two NPs were fabricated following the same method, a Wire Explosion method and both are dispersions in paraffin of the same concentration. Also, it can be seen that the sedimentation process seems to follow an exponential curve. This exponential curve seems to have different time constants depending on the material. Hence, determining this time constant might prove useful for classifying the materials. This will be addressed in Chapter 4.

### 3.4. Size Differentiation

As previously mentioned, the main goal of this Thesis is to determine wether a SSR and a VNA can be used to consistently and correctly classify nanoparticles of the same material with different size distributions.

Three copper samples were provided by the University of Pisa as described in Section 3.1. The main intentios was to generate nanoparticles using three widely different settings during the Wire Explosion in order to try and generate three different size distributions in the nanoparticles.

Once these nanoparticles were shipped to ICAI, we used the VNA alongside the SSR to measure their sedimentation curves.

Three dispersions of nanoparticles were created using a concentration of  $10 \,\mathrm{mg/mL}$ . The medium in which the nanoparticles would be dispersed in is pure paraffin oil, which proves to be a non-polar liquid, cheap, and non-reactive with the nanoparticles.

The sonication times for each one of the measurements was kept constant, as well as the temperature and measurement times. Each sample was sonicated for 15 minutes in intervals of 5 s ON and 10 s OFF (leading to a total of 20 minutes for one sonication), as explained in Section 3.2.

All nanoparticles' sedimentation times were measured multiple times in order to remove any outliers and also to take into account the variability noise inside the measurement can create.

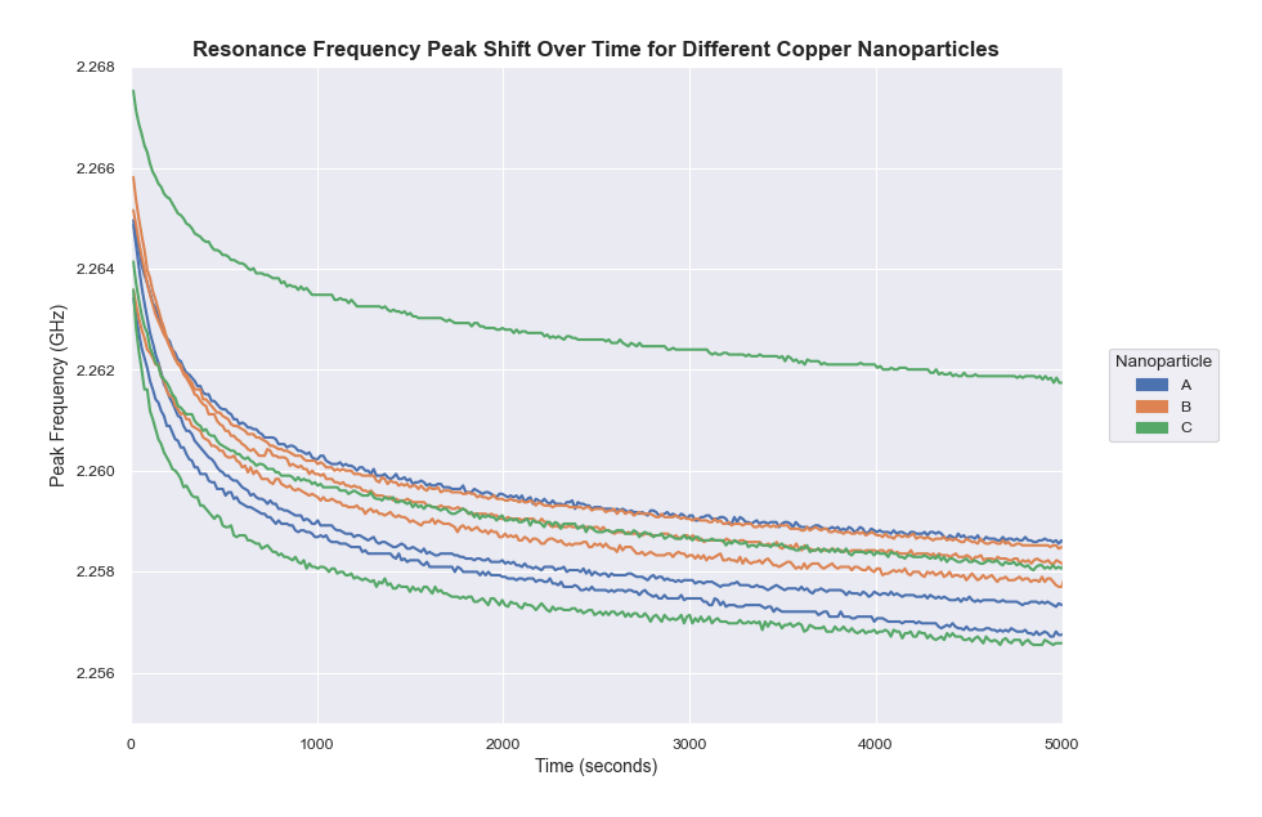


**Figure 3.8.** Peak resonance frequency over time depending on the nanoparticle sample sonicated.

On Figure 3.8, we can observe the sedimentation curves of the different nanoparticles. This graph was obtained measuring the peak resonance frequency of the nanoparticle dispersion using the VNA and the SSR mentioned in this Thesis.

As it can be observed, the curves seem quite similar, all following an exponential-like behaviour, common for sedimentation curves. The bigger nanoparticles will take less time to sediment while the smaller ones will remain a longer time suspended in the paraffin.

With this graph, a clear distinction between the nanoparticles can't be determined easily. All of the measurements seem to be very similar and, at least with a simple visual inspection, if no colors were used in the plot, it would be extremely difficult to differentiate and classify these nanoparticles.

Hence, a method to extract more information from this experiment is required. Since these signals are similar to exponentials, it would be interesting to obtain a time-constant distribution for each signal and see if with that information, classification would be easier. This will be explored in Chapter ??

### **Time Constant Extraction**

### 4.1. Time Constant Extraction Procedure

Exponential decay processes are common in many areas of science and engineering. In a simple exponential decay, a quantity m(t) decreases at a rate proportional to its current value. Equation 4.1 describes this behavior for a single decay component:

$$m(t) = f \exp\left(-\frac{t}{\tau}\right) + g \tag{4.1}$$

where  $\tau$  is the characteristic time constant of the decay, f is the decay amplitude (initial magnitude), and g is a baseline offset [99]. Processes such as radioactive decay, population decline, certain chemical reactions, fluorescence, and magnetic resonance relaxation often follow this single-exponential model [99]. In these cases, the time constant  $\tau$  (or its reciprocal, the rate constant  $1/\tau$ ) is a key parameter that can be obtained from experimental data.

However, not all systems can be characterized by a single time constant. Many complex systems exhibit multi-exponential behavior, meaning the observed decay is a combination of multiple exponential components or even a continuous distribution of time constants. For example, the decay of magnetization in confined media (as in NMR experiments on porous materials) involves multiple decay rates, and the effective "time constant" of such a system is actually a distribution rather than a single value [8]. In these cases, using a single  $\tau$  in Equation 4.1 is insufficient; instead, one must consider multiple exponentials contributing to m(t).

### 4.1.1. Multi-Exponential Formulation

To model systems with more than one decay process, the single-exponential model generalizes to a sum or continuum of exponentials. In the simplest multi-exponential scenario, one might have a discrete sum of two or more exponential terms. For instance, a system with two sequential decay processes could be described (conceptually) by an expression like [99]:

$$m(t_1, t_2) = f_1 \exp\left(-\frac{t_1}{\tau_1}\right) + f_2 \exp\left(-\frac{t_2}{\tau_2}\right) + g$$
 (4.2)

In equation 4.2,  $\tau_1$  and  $\tau_2$  are two distinct time constants for two stages of decay (with  $t_1$  and  $t_2$  being time variables in each stage), and this would yield a bi-exponential decay behavior. While this two-component example illustrates multiple decays, real systems can be even more complex.

In the most general case, the decay signal can be viewed as a *continuous superposition* of many exponential decays with different time constants. Instead of summing a few discrete terms, one can consider a distribution function  $f(\tau)$  that tells us how much contribution comes from decays of characteristic time  $\tau$ . Equation 4.3 expresses the measured signal as an integral (continuous sum) of exponential decays weighted by this distribution:

$$m(t) = \int_0^\infty f(\tau) \, \exp\left(-\frac{t}{\tau}\right) \, d\tau + g \,, \tag{4.3}$$

where  $f(\tau)$  is the *time-constant distribution* (often normalized so that its integral gives the total signal amplitude) and g is again any constant offset [8]. Equation 4.3 generalizes the decay model to account for an entire spectrum of time constants. In practice, g (baseline) can often be measured or assumed zero after appropriate corrections [8], so we will focus on the core integral term.

It is worth noting that the concept extends to higher dimensions as well. For processes involving two independent time variables (e.g. two-step decays or correlation experiments), one can define a two-dimensional distribution  $f(\tau_1,\tau_2)$  and write a double integral analogous to Equation 4.3 [8]. Such formulations allow modeling of even more complex decay behaviors. For simplicity, we will continue our discussion with the one-dimensional case, as the core concepts are similar for higher dimensions.

#### 4.1.2. Inverse Problem and Ill-Posedness

Determining the distribution  $f(\tau)$  from the measured signal m(t), as formulated in Equation 4.3, is a classic inverse problem[100]. This particular inverse problem is essentially an inverse Laplace transform: given the Laplace-transformed data m(t), we aim to recover the original distribution function  $f(\tau)$  [8].

Inverse Laplace transform problems are well-known to be severely ill-posed [8]. An ill-posed problem is one in which small errors or noise in the measured data m(t) can lead to large and unstable variations in the solution  $f(\tau)$ , or worse, the solution may not be unique or may not exist at all in a meaningful way. In practical terms, this means that experimental imperfections or measurement noise make it very difficult to directly compute  $f(\tau)$  with confidence.

This challenge arises because many different distributions of time constants can produce very similar decay curves when integrated together. As a result, distinguishing which distribution is truly responsible for the observed signal requires very accurate data and careful analysis. Simply put, multi-exponential decay analysis is not a straightforward curve-fitting problem—it is a delicate process.

A common and practical approach is to discretize the time constants into a finite set of  $N_{\tau}$ discrete values. Rather than evaluating an integral, the measured signal is approximated as a sum of exponential decays, each associated with a specific time constant  $\tau_i$ :

$$m(t) pprox \sum_{i=1}^{N_{\tau}} f_i \exp\left(-\frac{t}{\tau_i}\right) ,$$
 (4.4)

where  $f_i$  is the weight (or amplitude) of the decay corresponding to  $\tau_i$  [8]. Equation 4.4 serves as a numerical approximation of the continuous model in Equation 4.3, and it is widely used in practical data analysis.

In this discretized form, the problem becomes a system of linear equations. Let A be a matrix of size  $N_t \times N_\tau$ , where  $N_t$  is the number of time samples and  $N_\tau$  is the number of assumed time constants. Each element of *A* is defined as:

$$a_{ij} = \exp\left(-\frac{t_i}{\tau_j}\right) ,$$

so that the system can be written in matrix-vector notation as:

$$Ax \approx b$$
.

where  $x = [f_1, f_2, \dots, f_{N_{ au}}]^T$  is the vector of unknown distribution weights, and b = $[m(t_1), m(t_2), \dots, m(t_{N_t})]^T$  is the vector of measured data [9].

However, due to the nature of exponential functions, the matrix A is typically ill-conditioned or nearly singular, which again reflects the ill-posedness of the problem. Solving such a system directly often yields unstable and oscillatory solutions, especially in the presence of noise. Therefore, to obtain meaningful and interpretable results, we must apply stabilization techniques, which are discussed in the next section.

#### 4.1.3. Regularization and Stabilization of the Solution

To reliably extract the time-constant distribution  $x = \{f_i\}$  from noisy data, it is necessary to apply *regularization techniques*. Regularization introduces additional constraints or penalties that favor reasonable, smooth solutions for  $f(\tau)$  at the expense of exactly fitting the noise.

A common approach is to solve a regularized least-squares optimization instead of a plain least-squares fit. In a regularized formulation, we seek the vector x that balances fitting the data with keeping x "well-behaved." This can be written as an optimization problem:

$$\min_{x \ge 0} \left\{ \|Ax - b\|_2^2 + \lambda^2 \Omega(x) \right\} , \tag{4.5}$$

where the first term  $||Ax - b||_2^2$  is the usual sum of squared errors (ensuring we fit the data closely), and the second term  $\lambda^2 \Omega(x)$  is a regularization penalty that discourages undesirable solutions. The parameter  $\lambda$  controls the trade-off between fidelity to the data and the smoothness or size of the solution. The notation  $x \geq 0$  indicates that we also enforce a non-negativity constraint on the solution (since negative amplitudes  $f_i$  would be non-physical in most decay scenarios).

The choice of the penalty functional  $\Omega(x)$  determines the type of regularization. A very common choice is Tikhonov regularization, which uses:

$$\Omega(x) = ||x||_2^2 \tag{4.6}$$

i.e., the sum of squares of the components of x. In other words, the solution is penalized for having large overall magnitude or many large components. Using  $\Omega(x) = \|x\|_2^2$  (with  $x \ge 0$ ) in Equation 4.5 corresponds to a classical ridge-regression or Tikhonov approach. This tends to produce a smoother, more stable distribution  $f(\tau)$  by filtering out the high-frequency oscillations that typically come from fitting noise. In practical terms, regularization filters out the effects of noise in the solution, at the cost of a slight loss in resolution (e.g., very sharp features in the true distribution might be smoothed out).

The non-negativity constraint  $x \ge 0$  is also important. Since each  $f_i$  represents a contribution to the signal, it makes physical sense that  $f_i$  should be zero or positive (you cannot have a "negative" amount of signal component). Enforcing  $f_i \ge 0$  further stabilizes the solution and avoids unphysical oscillations where positive and negative components cancel out. Many algorithms for this problem use *Non-Negative Least Squares (NNLS)* or similar methods to impose this constraint.

Solving the regularized problem (Equation 4.5) can be done efficiently. One convenient way (as implemented by the authors of the reference study) is to augment the matrix system Ax = b with additional rows corresponding to the regularization term. For example, in the Tikhonov case, one can augment A with  $\lambda I$  (and augment b with a vector of zeros), which turns the minimization of  $\|Ax - b\|_2^2 + \lambda^2 \|x\|_2^2$  into an equivalent extended linear least-squares problem. Standard algorithms can then solve this augmented system, yielding the regularized solution for x.

The end result is a computed distribution  $f(\tau)$  that fits the experimental data within noise limits and avoids excessive oscillation or noise amplification.

### 4.1.4. Implementation

The methodology above might sound involved, but modern tools make it quite accessible. In fact, the authors of the study have provided simple MATLAB and Python scripts to perform this multi-exponential analysis [101]. Thanks to high-level numerical libraries, the entire inversion procedure (with regularization and constraints) can be implemented in only a few lines of code.

In order to test the performance of this tool, we generated a synthetic example by manually building an exponential signal which was the sum of two exponentials. We used Equation 4.7:

$$x(t) = 100e^{-10t} + 30e^{-100t} (4.7)$$

Yielding the results shown on Figure 4.1.

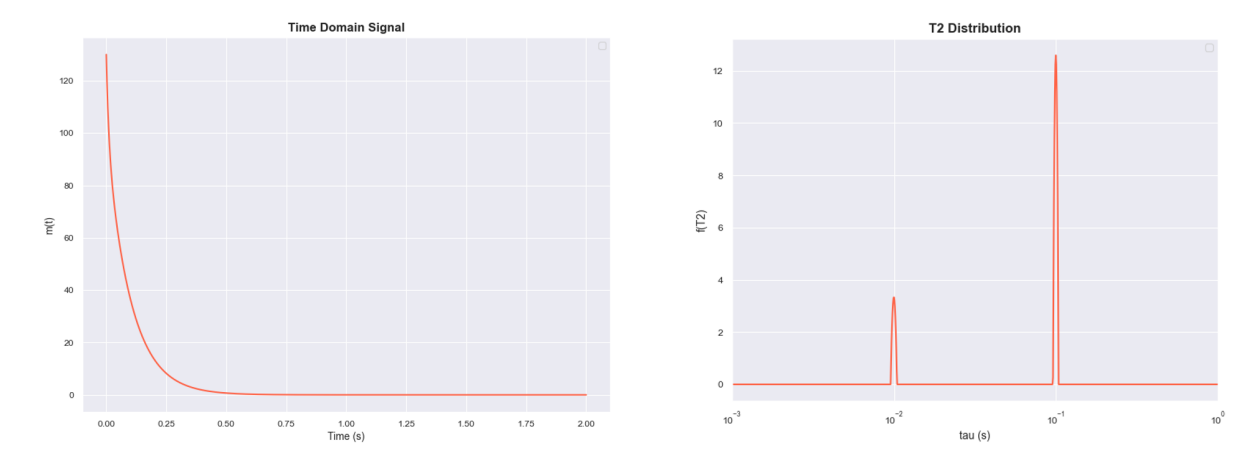


**Figure 4.1.** (left) Synthetic data generated for testing the time constant extraction; (right) results over the data.

As it can be seen on Figure 4.1, the time constants are perfectly determined by this method.

The output of this method is interpreted the same way as the output of a Fourier transform when talking about the sum of sinusoidal signals, but, in this case, they are exponential signals.

# 4.2. Differentiating Between Copper Nanoparticle Samples

The main goal of this Thesis is to try and differentiate in between the three Copper NP Samples fabricated at the University of Pisa. Therefore, the data in Figure 3.8 was input to the Python code and the results were recorded.

If we look at the whole time constant distribution of this dataset, we can see the results shown on Figure 4.2.

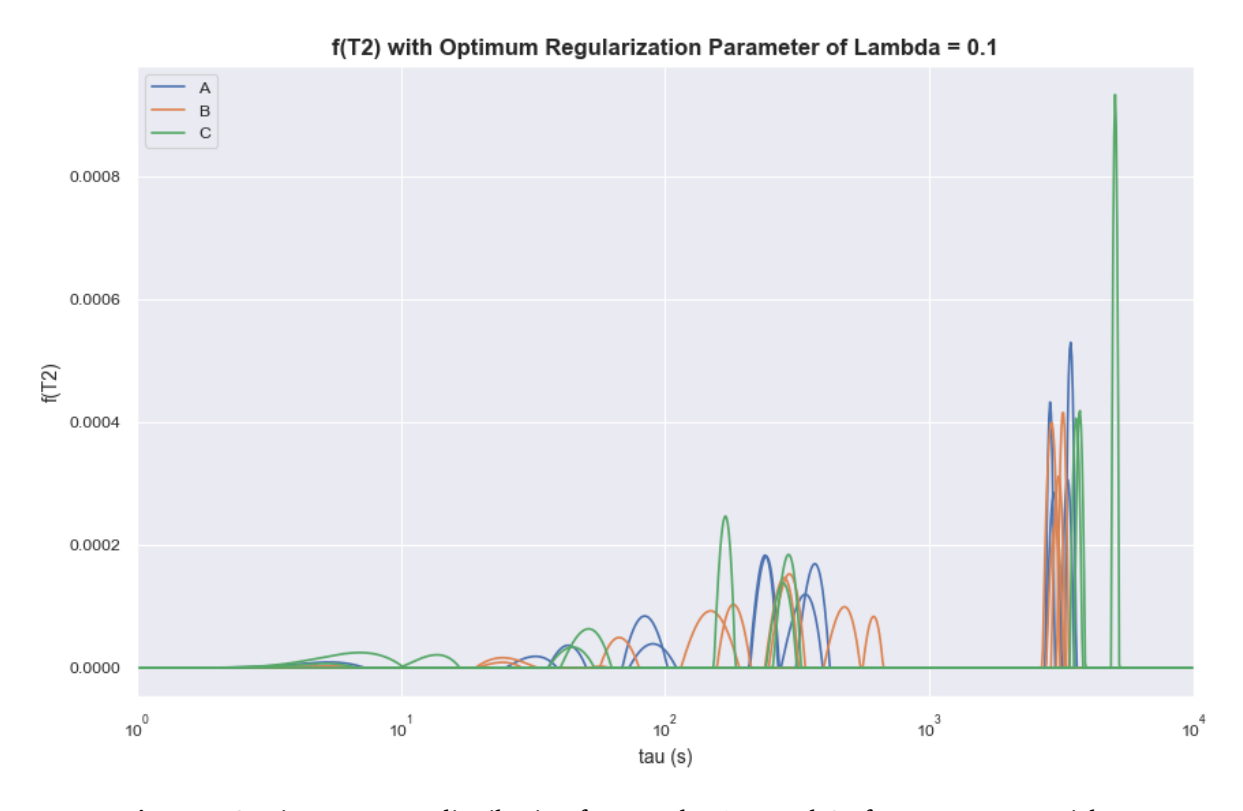
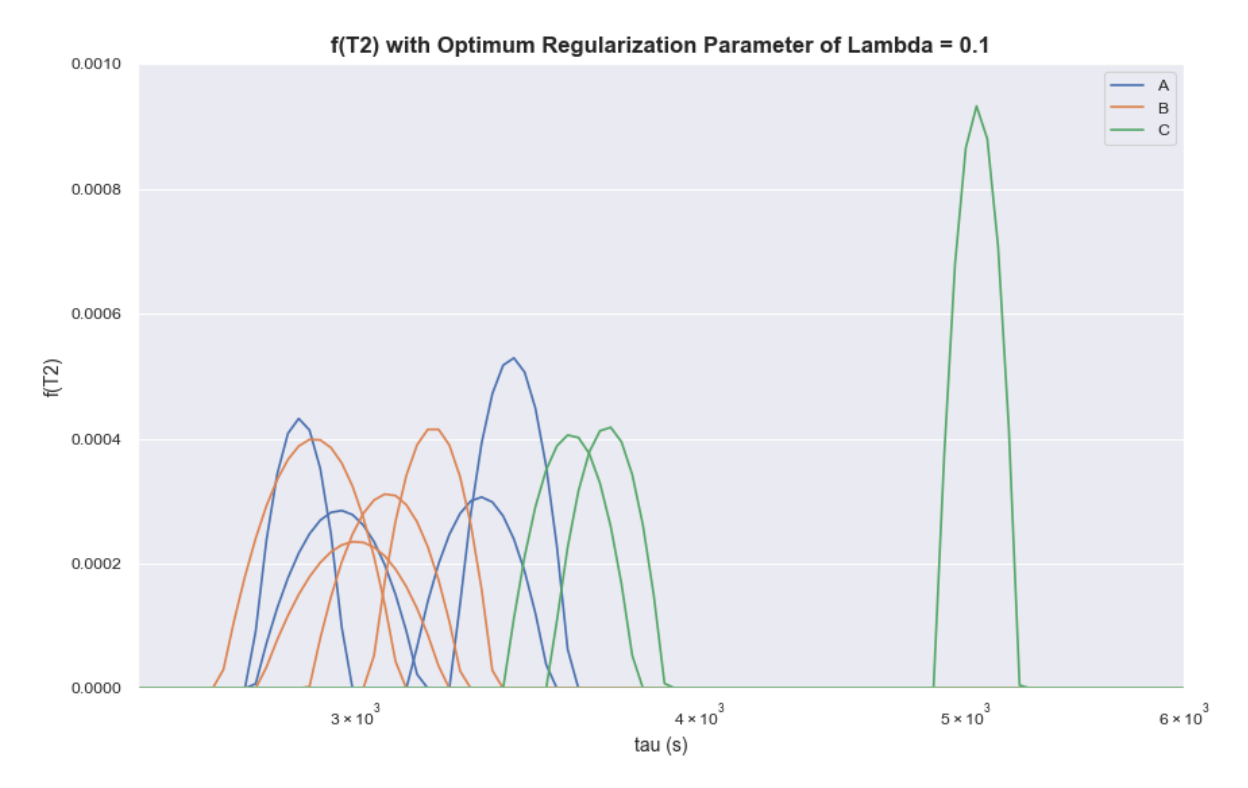


Figure 4.2. Time constant distribution for samples A, B and C of copper nanoparticles.

Looking at this, we see a wide variety of signals and the plot is quite confusing. However, we do see that the principal components are grouped in a single time constant range (between  $10^3$  s and  $10^4$  s). Therefore, we can zoom into this range, which yields the results shown on Figure 4.3.



**Figure 4.3.** Time constant distribution zoomed into the principal components for samples A, B and C of copper nanoparticles.

With this new view of the results, we can clearly see two things. Firstly, nanoparticles A and B seem to be highly intertwined, with their measurements being mostly similar all the time. Secondly, nanoparticle C seems to differ more with one of the results being quite more different than the other two. This right-most result may be due to noise or even some external factors which might have affected the measurement.

Therfore, with these results, we can conclude that nanoparticles A and B will have a very similar size distribution and nanoparticle C will have a different size distribution to the one present in the other two.

### 4.3. Mixing Copper Nanoparticles

Since in the previous section we have determined that nanoparticles B and C are the most different, we designed a new measurement set by mixing two dispersions of nanoparticles B and C, both with the same concentration  $(10\,\text{mg/mL})$  and measuring them to compare and see if this new mix would have intermediate results to those measured in B and C.

The sedimentation curves can be seen on Figure 4.4.

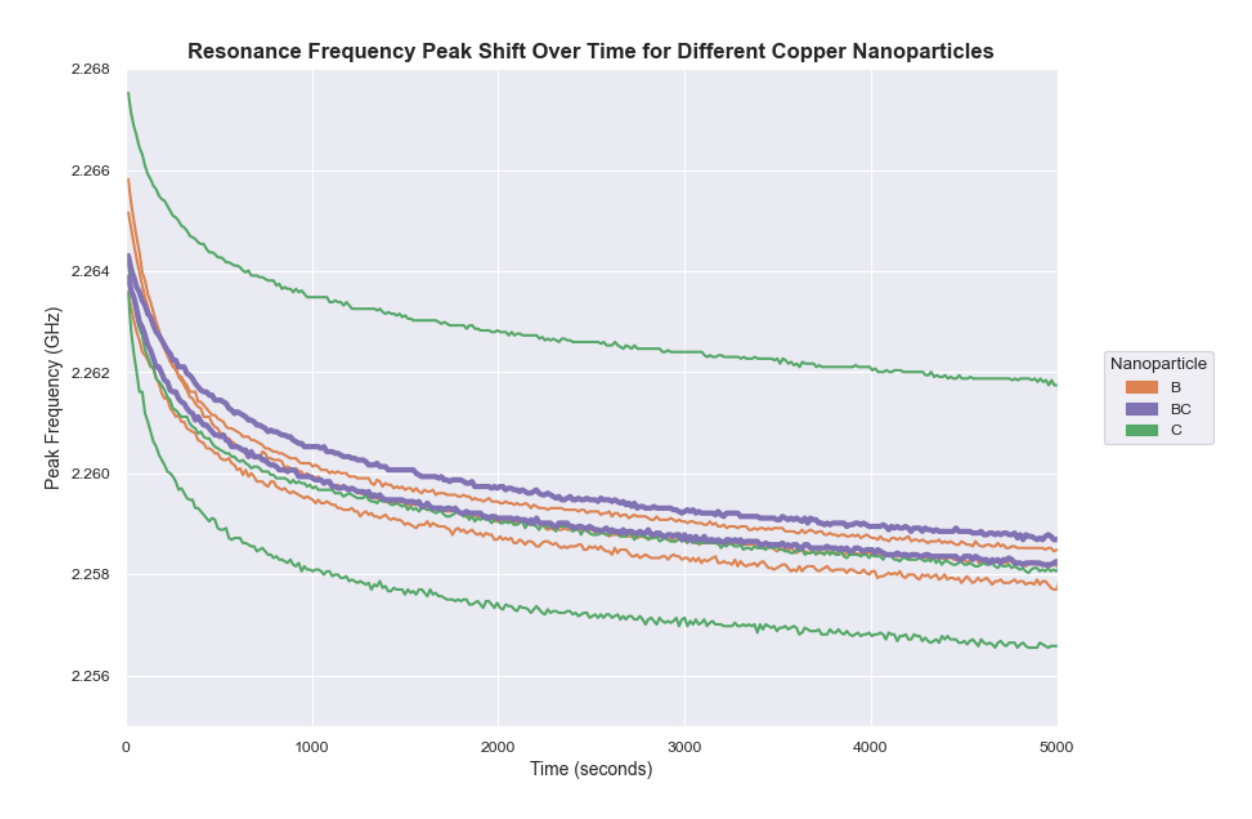


Figure 4.4. Sedimentation curves of copper nanoparticles B and C and the mix of BC nanoparticles.

A good sign is that these measurements are in between the values of both nanoparticles, therefore the results provided by the time constant analysis look promising.

These results can be seen on Figure 4.5. This figure has the same issues than the previous one, therefore, we will only focus on the principal components, which can be seen on Figure 4.6.

As expected the results for the BC mix of nanoparticles lay in between the results for both of the particles separetely. However, we can see that the results are very similar to those of the C nanoparticle. A simple hypothesis would be that sample C has larger nanoparticles and that when mixing nanoparticles B and C, these larger nanoparticles sediment before and therefore the B nanoparticles have a lower impact on the signal.

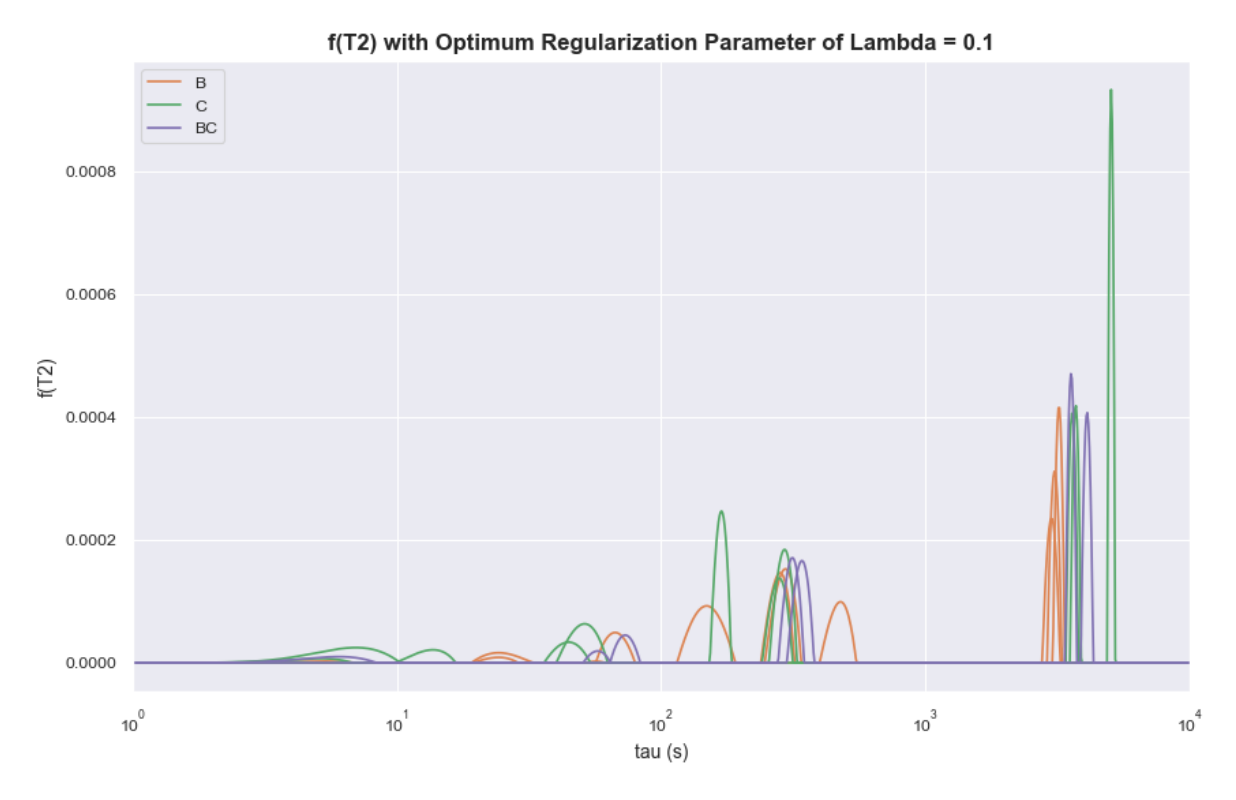
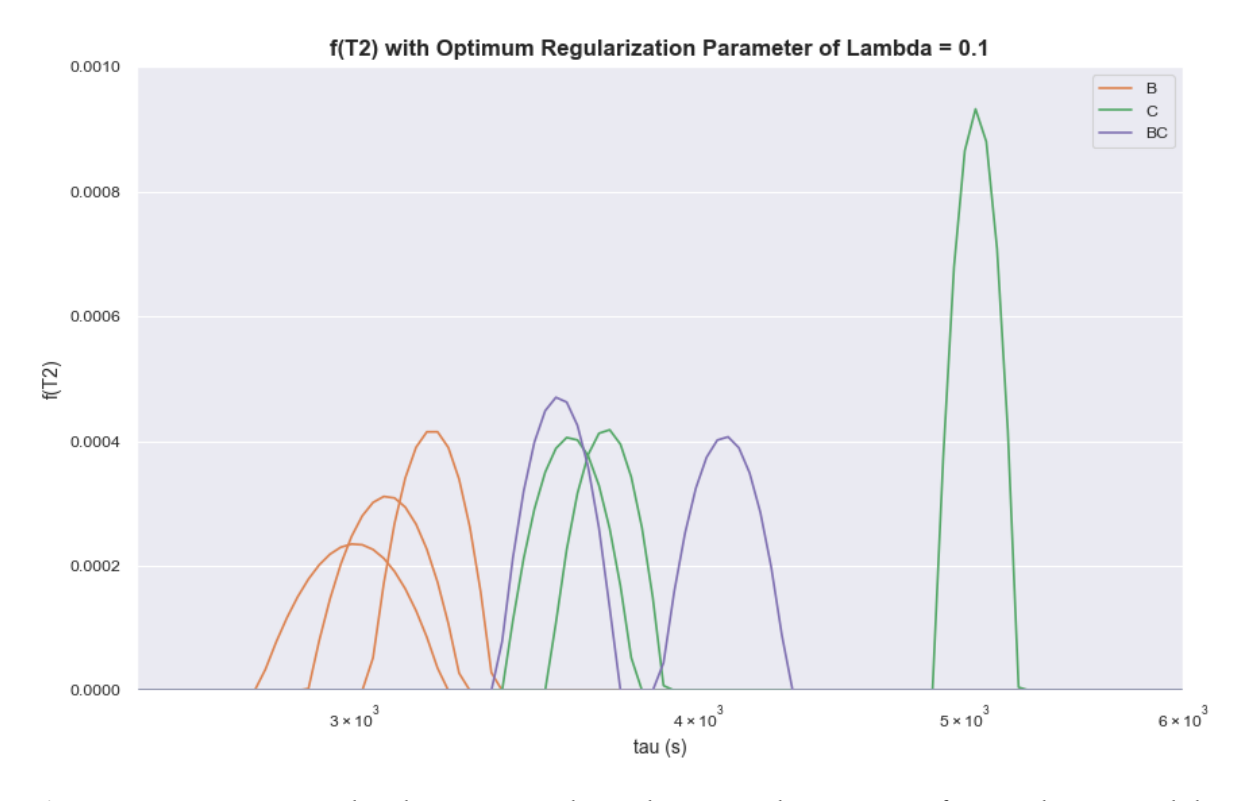


Figure 4.5. Time constant distribution for samples B, C and the BC mix of copper nanoparticles



**Figure 4.6.** Time constant distribution zoomed into the principal components for samples B, C and the BC mix of copper nanoparticles.

# 4.4. Differentiating Between Copper and Iron Nanoparticle Samples

Since we have been able to differentiate between nanoparticle size in the same material, the question as to wether this method can also be used to differentiate nanoparticles of different materials is only natural.

Therfore, we input the data represented in Figure 3.7 and compared it with the nanoparticles A B and C. The results can be seen on Figures 4.7 and 4.8 (close-up into the principal time constant).

These results show that even when not only considering the principal time constant, iron naopaprticles have a different distribution in comparison to the copper nanoparticles. Therefore, this method could potentially also be used to classify different materials.

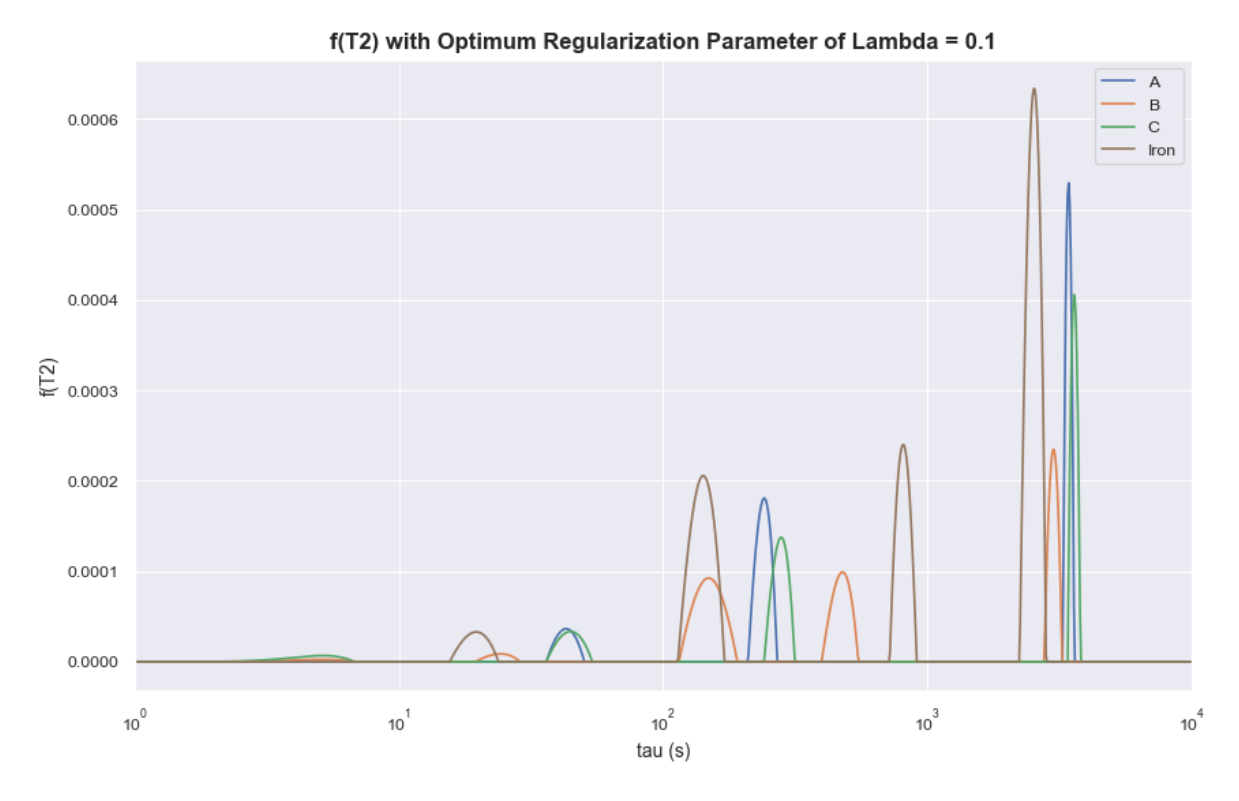


**Figure 4.7.** Time constant distribution for samples A, B and C of copper nanoparticles and one of iron nanoparticles.

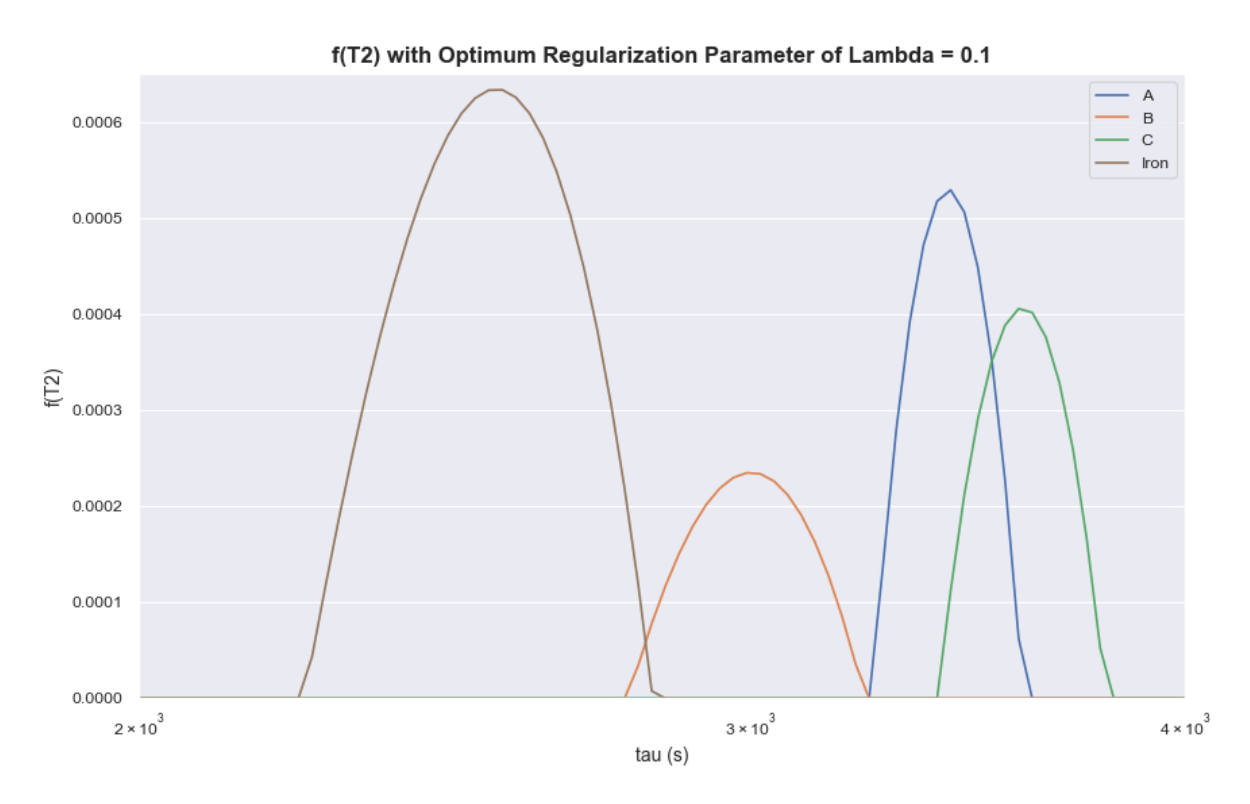


**Figure 4.8.** Time constant distribution zoomed into the principal components for samples A, B and C of copper nanoparticles and one of iron nanoparticles.

### 4.5. Comparison with University of Pisa's Results

During our experiments on the nanoparticles provided by the University of Pisa, they were performing a characterization of the nanoparticles. This characterization was kept independant from our results, and vice-versa, so as to perform a double-blind experiment and not influence the results of both parties.

**Table 4.1.** Largest and smallest particle size depending on the sample.

NP	Large Particles Diameter (nm)	Small Particles Diameter (nm)	
Α	462	164	
В	490	156	
С	483	122	

When looking at the results on Table 4.1, they do not seem to match those obtained by our research since they show that the nanoparticles in C have the smallest nanoparticles and do not have the largest particles. However, when looking at the results in Figure 4.9, we see that indeed nanoparticles A and B have a very similar size distribution, while C has a different size distribution.

Also, we can see that even if C does not have the largest nanoparticles, it does have more quantity of larger nanoparticles that A or B and therefore relates correctly with our results and hypotheses.

Therefore, while these two experiments were performed independently, they yield the same results. This serves as a corroboration of the results obtained in Figure 4.3.

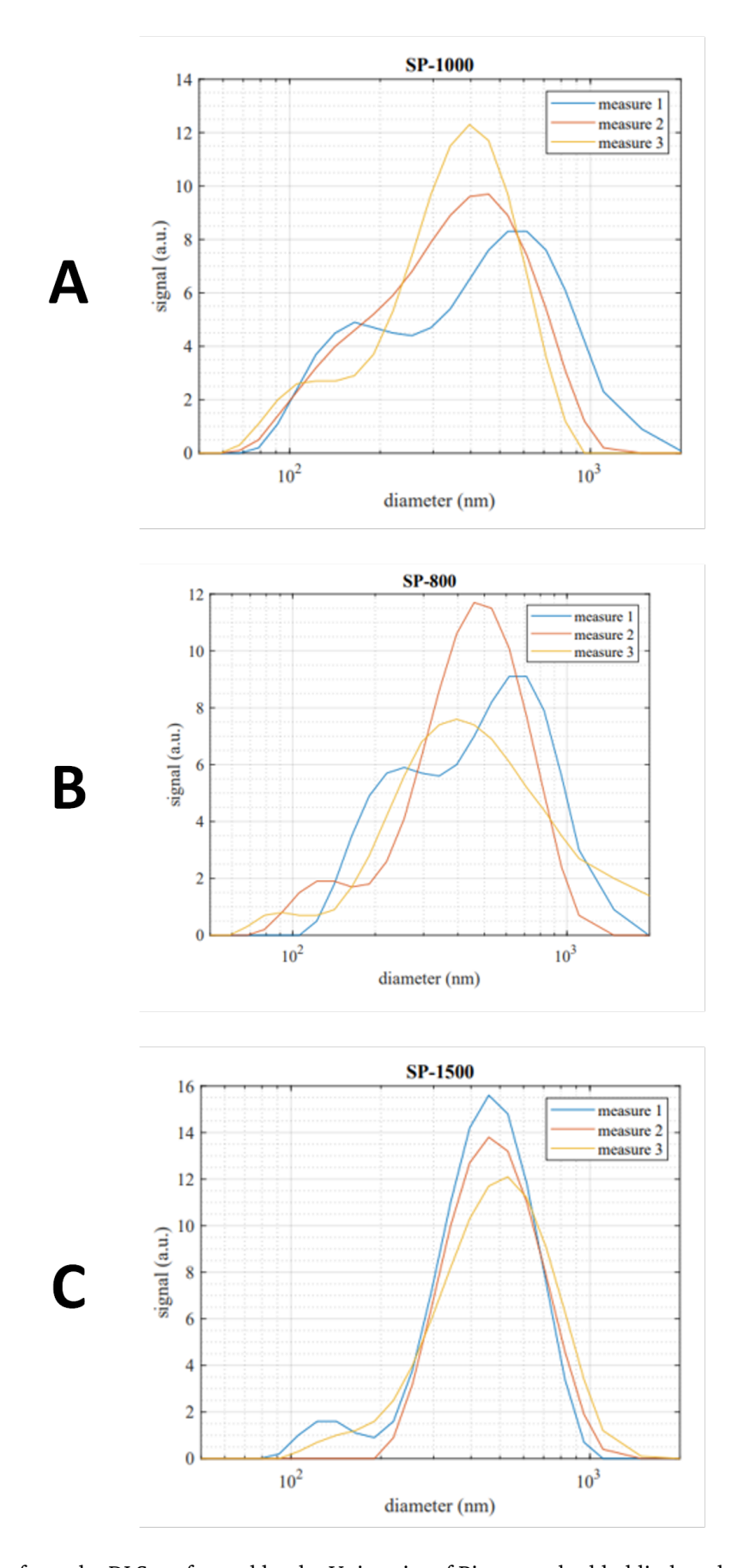


Figure 4.9. Data from the DLS performed by the University of Pisa on a double-blind analysis of the NPs.

# 5

### Conclusion

### 5.1. Overview of the Research and Findings

This thesis has presented the design and validation of a novel sensor system for characterizing metallic nanoparticles, addressing a critical need for faster and more automated nanoparticle analysis in industrial and research settings. The proposed sensor is based on a metamaterial-inspired electromagnetic resonator (specifically, a planar square spiral resonator), which is highly sensitive to the presence and distribution of nanoparticles in its proximity.

By monitoring the real-time response of this resonator when nanoparticle dispersions are introduced, the system can profile the sedimentation of nanoparticles in a fluid and extract meaningful signatures related to their physical characteristics. This approach transforms the traditionally time-consuming task of nanoparticle characterization into an automated process, aligning with modern industry demands for smart, in-line instrumentation. The research performed extensive experimental testing with metallic nanoparticle samples. Through this approach, the thesis demonstrated that the sensor can reliably capture the dynamic sedimentation curves of nanoparticle suspensions and translate them into information about particle size distribution and material composition. In essence, the work bridges the gap between advanced nanomaterials characterization techniques and practical sensing technology, providing a prototype that is both scientifically insightful and practically relevant.

## 5.2. Relevance to Industry 4.0 and Smart Manufacturing

A strong motivation behind this work is the growing demand for advanced sensing solutions in the context of Industry 4.0, the modern paradigm of smart manufacturing and automation.

Industry 4.0 production environments require sensors that can operate in real-time, with minimal human intervention, high precision, and reliability. Traditional nanoparticle characterization methods (such as electron microscopy or laboratory particle analyzers) do not meet these criteria – they are labor-intensive, slow, and cannot be easily integrated into an automated production line.

In contrast, the sensor developed in this thesis is inherently suited for an Industry 4.0 setting. Once deployed, it functions as a real-time monitoring device: it continuously converts the

state of a nanoparticle dispersion (an external environmental condition) into an electrical signal (a resonant frequency shift or amplitude change) that can be automatically recorded and interpreted. No manual sampling and imaging are needed after the initial setup, and the measurement is non-destructive (the sample can remain in the production flow).

This means that manufacturing processes involving nanoparticles could be equipped with this kind of sensor to achieve in-line quality control and feedback. Moreover, metamaterial-based sensors like the one presented offer additional advantages that align with smart factory requirements. They are typically compact, inexpensive to fabricate (the resonator in this work is a simple printed circuit), and potentially capable of wireless or networked operation when connected to appropriate electronics. Research has shown that sensors based on metamaterials can achieve the high sensitivity and low detection limits needed in advanced industrial applications, while also being readily integrable into larger systems.

The ease of system integration is particularly important: it implies such sensors can be embedded in production equipment or pipelines without large footprints or special infrastructure.

Currently, verifying the size and consistency of manufactured nanoparticles might require taking samples to a lab and running lengthy analyses (microscopy, centrifugation, etc.), during which the production might continue unchecked or be paused. Our sensor, on the other hand, gives near-instant feedback on each batch or even continuously during production, thus avoiding the delays associated with off-line analysis. This improves throughput and can prevent batches with out-of-specification nanoparticles from going undetected until much later.

### 5.3. Limitations and Challenges

While the results of this thesis are promising, it is important to acknowledge the limitations and challenges of the developed sensor approach.

One fundamental limitation is that the sensor currently provides a relative or qualitative characterization rather than an absolute one. In other words, while it can tell if one sample's particles are larger on average than another's, it does not directly output the exact particle size distribution or exact material composition without reference to calibration data.

Traditional methods like electron microscopy or Dynamic Light Scattering (DLS) can give absolute measurements (e.g. an average diameter in nanometers, or a full size distribution curve).

In contrast, our resonator sensor measures an electromagnetic response that must be interpreted to infer particle properties. This interpretation typically relies on models or comparisons. For example, we might need to calibrate the sensor with known samples to create a mapping between the "time constant distribution" extracted from the sedimentation curve and actual particle size ranges. Developing a robust calibration for every new type of nanoparticle is a challenge and would be necessary before the sensor could be used as a stand-alone metrology tool.

Another challenge lies in the resolution and overlapping signatures. If two nanoparticle samples have very subtle differences in size distribution, the sensor's ability to distinguish them is constrained by signal noise and the fundamental resolution of the method. In our experiments, Samples A and B were intentionally fairly similar, and indeed the sensor correctly indicated they were alike (which is as expected). However, distinguishing subtle differences

might be difficult if those differences do not produce a sufficiently different sedimentation profile within the time window of observation.

Additionally, the sensor's measurements are governed by physical contrasts (density, permittivity, magnetic permeability) between materials. If those contrasts are small, more sensitive or different resonator designs might be required.

The method's reliance on sedimentation introduces its own limitations. Sedimentation is a process that depends on gravity (or centrifugal force if aided by centrifugation), fluid viscosity, and particle density. Very small nanoparticles (say, much below 100 nm, especially if stabilized in solution) may take a very long time to sediment or might exhibit significant Brownian motion that counteracts sedimentation. In such cases, the "sedimentation profile" might be extremely slow or almost flat over practical timescales, making it hard for the sensor to get a reading within a reasonable time.

In summary, while the sensor provides rich data, making sense of that data in an automated way is non-trivial. We managed it in post-processing for the thesis, but an industrial monitor would need a reliable on-line algorithm. This could be considered a limitation of the current state of the system though it is also an opportunity for improvement.

### 5.4. Alignment with the Sustainable Development Goals (SDGs)

A key strength of the sensor technology developed in this thesis is its clear alignment with several United Nations Sustainable Development Goals:

#### SDG 7: Affordable and Clean Energy

Precise, real-time monitoring of metallic nanoparticles supports the reliable production of nanomaterials used in advanced catalysts, battery electrodes, and photovoltaic coatings, thereby accelerating access to clean energy technologies.

#### • SDG 9: Industry, Innovation and Infrastructure

The low-cost, compact metamaterial sensor fosters resilient and sustainable industrialization by enabling inline quality control, automated process optimization, and smart factory integration without human intervention.

#### • SDG 12: Responsible Consumption and Production

By shortening the feedback loop for detecting deviations in nanoparticle size and composition, the sensor minimizes waste from off-specification batches and reduces the consumption of reagents, promoting more resource-efficient manufacturing.

### References

- [1] V. V. Mody, R. Siwale, A. Singh, and H. R. Mody, "Introduction to metallic nanoparticles," *Journal of Pharmacy and Bioallied Sciences*, Dec. 2010.
- [2] M. M. Honrubia, G. Caposciutti, F. J. Herraiz-Martínez, J. M. Domingo, B. Tellini, and R. Giannetti, "Measuring sedimentation profiles for nanoparticle characterization through a square spiral resonator sensor," *Nanomaterials in Chemical Sensors*, Apr. 2024.
- [3] R. Wojnarowska, J. Polit, D. Broda, M. Gonchar, and E. M. Sheregii, "Surface enhanced raman scattering as a probe of the cholesterol oxidase enzyme," *Applied Physics Letters*, 2015.
- [4] A. Rygula, K. Majzner, K. M. Marzec, A. Kaczor, M. Pilarczyk, and M. Baranska, "Raman spectroscopy of proteins: A review," *Journal of Raman Spectroscopy*, 2013.
- [5] K. Kong, C. Kendall, N. Stone, and I. Notingher, "Raman spectroscopy for medical diagnostics—from in-vitro biofluid assays to in-vivo cancer detection," *Advanced Drug Delivery Reviews*, 2015.
- [6] P. G. Jamkhandea, N. W. Ghuleb, A. H. Bamerc, and M. G. Kalaskard, "Metal nanoparticles synthesis: An overview on methods of preparation, advantages and disadvantages, and applications," *Journal of Drug Delivery Science and Technology*, Jul. 23, 2019.
- [7] Z. Starowicz, R. Wojnarowska-Nowak, P. Ozga, and E. M. Sheregii, "The tuning of the plasmon resonance of the metal nanoparticles in terms of the sers effect," *Colloid and Polymer Science*, 2018
- [8] H. C. Torrey, "Bloch equations with diffusion terms," Physical Review, 1956.
- [9] S. Deoni, "Biophysical and physiological principles of t1 and t2," *Advances in Magnetic Resonance Technology and Applications*, 2020.
- [10] M. Modena, B. Rühle, T. Burg, and S. Wuttke, "Nanoparticle characterization: What to measure?" *Advanced Materials*, May 2019.
- [11] A. Bratovcic, "Different applications of nanomaterials and their impact on the environment," *International Journal of Material Science and Engineering*, 2019.
- [12] E. Roduner, "Size matters: Why nanomaterials are different," Chemical Society Reviews,
- [13] C. A. Johnson, "Generalization of the gibbs-thomson equation," Surface Science, 1965.
- [14] N. Joudeh and D. Linke, "Nanoparticle classification, physicochemical properties, characterization, and applications: a comprehensive review for biologists," *Journal of Nanobiotechnology*, 2022.
- [15] A. M. Ealia and Saravanakumar, "A review on the classification, characterisation, synthesis of nanoparticles and their application," *IOP Conference Series: Materials Science and Engineering*, 2017.
- [16] K. Pan and Q. Zhong, "Organic nanoparticles in foods: Fabrication, characterization, and utilization.," *Annu Rev Food Sci Technol*, 2016.

- [17] C. M. Long, M. A. Nascarella, and P. A. Valberg, "Carbon black vs. black carbon and other airborne materials containing elemental carbon: Physical and chemical distinctions," *Environmental Pollution*, 2013.
- [18] N. Toshima and T. Yonezawa, "Bimetallic nanoparticles—novel materials for chemical and physical applications," *New Journal of Chemistry*, 1998.
- [19] E. C. Dreaden, A. M. Alkilany, X. Huang, C. J. Murphy, and M. A. El-Sayed, "The golden age: Gold nanoparticles for biomedicine," *Chemical Society Reviews*, 2012.
- [20] L. Égerházi and T. Szörényi, "The potential of wire explosion in nanoparticle production interms of reproducibility," *MDPI Materials*, Jun. 12, 2024.
- [21] H. R. Ghorbani, "A review of methods for synthesis of al nanoparticles," *Oriental Journal of Chemistry*, Nov. 20, 2014.
- [22] E. Roduner, "Size matters: Why nanomaterials are different," Chemical Society Reviews, 2006.
- [23] C. Buzea, I. I. Pacheco, and K. Robbie, "Nanomaterials and nanoparticles: Sources and toxicity," *Biointerphases*, 2007.
- [24] M. G. Lines, "Nanomaterials for practical functional uses," *Journal of Alloys and Compounds*, 2008.
- [25] A. Gade, A. Ingle, C. Whiteley, and M. Rai, "Mycogenic metal nanoparticles: Progress and applications," *Biotechnology Letters*, 2010.
- [26] Q. Wu, W. Miao, H. Gao, and D. Hui, "Mechanical properties of nanomaterials: A review," *Nanotechnology Reviews*, 2020.
- [27] Y. B. Pithawalla, M. S. El-Shall, S. C. Deevi, V. Ström, and K. V. Rao, "Synthesis of magnetic intermetallic feal nanoparticles from a non-magnetic bulk alloy," *Journal of Physical Chemistry B*, 2001.
- [28] D. Guo, G. Xie, and J. Luo, "Mechanical properties of nanoparticles: Basics and applications," *Journal of Physics D: Applied Physics*, 2013.
- [29] S. Tan, R. L. Sherman, and W. T. Ford, "Nanoscale compression of polymer microspheres by atomic force microscopy," *Langmuir*, 2004.
- [30] S. Armini, I. U. Vakarelski, C. M. Whelan, K. Maex, and K. Higashitani, "Nanoscale indentation of polymer and composite polymer-silica core-shell submicrometer particles by atomic force microscopy," *Langmuir*, 2007.
- [31] T. Savage and A. M. Rao, "Thermal properties of nanomaterials and nanocomposites," *Thermal Conductivity (Springer)*, 2004.
- [32] R. A. Andrievski, "Review of thermal stability of nanomaterials," *Journal of Materials Science*, 2014.
- [33] L. Qiu, N. Zhu, Y. Feng, E. E. Michaelides, G. Żyła, D. Jing, et al., "A review of recent advances in thermophysical properties at the nanoscale: From solid state to colloids," *Physics Reports*, 2020.
- [34] J. A. Eastman, S. U. S. Choi, S. Li, W. Yu, and L. J. Thompson, "Anomalously increased effective thermal conductivities of ethylene glycol-based nanofluids containing copper nanoparticles," *Applied Physics Letters*, 2001.
- [35] Y. Jun, J. Seo, and J. Cheon, "Nanoscaling laws of magnetic nanoparticles and their applicabilities in biomedical sciences," *Accounts of Chemical Research*, 2008.
- [36] A. G. Kolhatkar, A. C. Jamison, D. Litvinov, R. C. Willson, and T. R. Lee, "Tuning the magnetic properties of nanoparticles," *International Journal of Molecular Sciences*, 2013.
- [37] M. Kalubowilage, K. Janik, and S. H. Bossmann, "Magnetic nanomaterials for magnetically-aided drug delivery and hyperthermia," *Applied Sciences*, 2019.

- [38] P. Kumbhakar, S. S. Ray, and A. L. Stepanov, "Optical properties of nanoparticles and nanocomposites," *Hindawi*, 2014.
- [39] N. G. Khlebtsov and L. A. Dykman, "Optical properties and biomedical applications of plasmonic nanoparticles," *Journal of Quantitative Spectroscopy and Radiative Transfer*, 2010.
- [40] K. L. Kelly, E. Coronado, L. L. Zhao, and G. C. Schatz, "The optical properties of metal nanoparticles: The influence of size, shape, and dielectric environment," *ACS Publications*, 2003.
- [41] B. R. Cuenya, S.-H. Baeck, T. F. Jaramillo, and E. W. McFarland, "Size-and support-dependent electronic and catalytic properties of au0/au3+ nanoparticles synthesized from block copolymer micelles," *Journal of the American Chemical Society*, 2003.
- [42] M. Valden, X. Lai, and D. W. Goodman, "Onset of catalytic activity of gold clusters on titania with the appearance of nonmetallic properties," *Science*, 1998.
- [43] R. Xu, D. Wang, J. Zhang, and Y. Li, "Shape-dependent catalytic activity of silver nanoparticles for the oxidation of styrene," *Chemistry An Asian Journal*, 2006.
- [44] I. Khan, K. Saeed, and I. Khan, "Nanoparticles: Properties, applications and toxicities," *Arabian Journal of Chemistry*, 2019.
- [45] J. Epp, "X-ray diffraction (xrd) techniques for materials characterization," *Materials Characterization Using Nondestructive Evaluation (NDE) Methods, Elsevier*, 2016.
- [46] R. Groarke, R. K. Vijayaraghavan, D. Powell, A. Rennie, and D. Brabazon, "Powder characterization—methods, standards, and state of the art," *Fundamentals of Laser Powder Bed Fusion of Metals, Elsevier*, 2021.
- [47] C. S. Fadley, "X-ray photoelectron spectroscopy: Progress and perspectives," *Journal of Electron Spectroscopy and Related Phenomena*, 2010.
- [48] C. S. C. Santos et al., "Industrial applications of nanoparticles a prospective overview," *Materials Today: Proceedings*, 2015.
- [49] ISO, "Nanotechnologies vocabulary part 1: Core terms," ISO/TS 80004-1, 2010.
- [50] L. D. Chambers, K. R. Stokes, F. C. Walsh, and R. J. K. Wood, "Modern approaches to corrosion protection of aluminium using nanotechnology," *Surface and Coatings Technology*, 2006.
- [51] F. Hassan, "Photochemical treatments of textile industries wastewater," Iraq, 2010.
- [52] D. I. Petkowicz, R. Brambilla, C. Radtke, et al., "Photodegradation of methylene blue by in situ generated titania supported on a naa zeolite," *Applied Catalysis A*, 2009.
- [53] W. H. Ko, "Micro sensors for physical, chemical, and biomedical applications," *Sensors and Actuators A: Physical*, 2007.
- [54] V. F. Neto et al., "Advanced coating systems towards the analysis of polymer flow within microcavities," *PMI 5th International Conference on Polymers and Moulds Innovations*, 2012.
- [55] O. V. Salata, "Applications of nanoparticles in biology and medicine," *Journal of Nanobiotechnology*, 2004.
- [56] T. A. Taton, "Nanostructures as tailored biological probes," Trends in Biotechnology, 2002.
- [57] M. Bruchez, M. Moronne, P. Gin, S. Weiss, and A. P. Alivisatos, "Semiconductor nanocrystals as fluorescent biological labels," *Science*, 1998.
- [58] W. C. W. Chan and S. M. Nie, "Quantum dot bioconjugates for ultrasensitive nonisotopic detection," *Science*, 1998.
- [59] S. Wang, N. Mamedova, N. A. Kotov, W. Chen, and J. Studer, "Antigen/antibody immunocomplex lock," *Nano Letters*, 2002.

- [60] D. Panatattor et al., "Immunization with peptide-functionalized carbon nanotubes enhances virus-specific neutralizing antibody responses," *Chemistry and Biology*, 2003.
- [61] A. de la Isla et al., "Nanohybrid scratch resistant coating for teeth and bone viscoelasticity manifested in tribology," *Materials Research Innovations*, 2003.
- [62] R. S. Molday and D. MacKenzie, "Immunospecific ferromagnetic iron dextran reagents for the labelling and magnetic separation of cells," *Journal of Immunological Methods*, 1982.
- [63] Y. C. Cao, R. Jin, J. M. Nam, C. S. Thaxton, and C. A. Mirkin, "Raman dye-labeled nanoparticle probes for proteins," *Journal of the American Chemical Society*, 2003.
- [64] R. Mahtab, J. P. Rogers, and C. J. Murphy, "Protein-sized quantum dot luminescence can distinguish between "straight," "bent," and "kinked" oligonucleotides," *Journal of the American Chemical Society*, 1995.
- [65] L. G. Gutwein and T. J. Webster, "Affects of alumina and titania nanoparticles on bone cell function," *American Ceramic Society 26th Annual Meeting Conference Proceedings*, 2003.
- [66] J. Ma, H. Wong, L. B. Kong, and K. W. Peng, "Biomimetic processing of nanocrystalline bioactive apatite coating on titanium," *Nanotechnology*, 2003.
- [67] I. Roy et al., "Ceramic-based nanoparticles entrapping water-insoluble photosensitizing anticancer drugs: A novel drug-carrier system for photodynamic therapy," *Journal of the American Chemical Society*, 2003.
- [68] J. Yoshioka and T. Kobayashi, "Intracellular hyperthermia for cancer using magnetic cationic liposomes," *Journal of Magnetism and Magnetic Materials*, 1999.
- [69] R. Weissleder, G. Elizondo, J. Wittenburg, C. A. Rabito, H. H. Bengele, and L. Josephson, "Ultrasmall superparamagnetic iron oxide: Characterization of magnetite and oxidation products," *Radiology*, 1990.
- [70] W. J. Parak et al., "Cell motility and meta-static potential studies based on quantum dot imaging of phagokinetic tracks," *Advanced Materials*, 2002.
- [71] M.-C. Daniel and D. Astruc, "Gold nanoparticles: Assembly, supramolecular chemistry, quantum-size-related properties, and applications toward biology, catalysis, and nanotechnology," *Chemical Reviews*, vol. 104, no. 1, pp. 293–346, 2004.
- [72] V. Amendola and M. Meneghetti, "Size evaluation of gold nanoparticles by uv–vis spectroscopy," *Journal of Physical Chemistry C*, vol. 111, no. 40, pp. 15 021–15 024, 2017.
- [73] S. Bhattacharjee, "Dls and zeta potential what they are and what they are not?" *Journal of Controlled Release*, vol. 235, pp. 337–351, 2016.
- [74] D. B. Williams and C. B. Carter, *Transmission Electron Microscopy: A Textbook for Materials Science*. Springer, 2009.
- [75] R. F. Egerton, "Radiation damage to organic and inorganic specimens in the tem," *Micron*, vol. 42, no. 10, pp. 147–160, 2011.
- [76] J. I. Goldstein, D. E. Newbury, and D. C. Joy, *Scanning Electron Microscopy and X-ray Microanalysis*. Springer, 2017.
- [77] U. Rabe, T. Glatzel, and H. J. Hug, "Scanning probe microscopy: From reactive to non-reactive methods via afm," *Journal of Microscopy*, vol. 239, no. 2, pp. 123–134, 2010.
- [78] A. Henglein, "Physicochemical properties of small metal particles in solution: "microelectrode" reactions, chemisorption, composite metal particles, and the atom-to-metal transition," *Journal of Physical Chemistry B*, vol. 105, no. 48, pp. 10590–10594, 2001.
- [79] B. D. Cullity and S. R. Stock, *Elements of X-ray Diffraction*. Prentice Hall, 2001.

- [80] E. C. Le Ru and P. G. Etchegoin, "Principles of surface-enhanced raman spectroscopy and related plasmonic effects," *Elsevier*, 2009.
- [81] B. C. Smith, "Fundamentals of fourier transform infrared spectroscopy," CRC Press, 2011.
- [82] R. A. Dragovic, C. Gardiner, and A. S. Brooks, "Sizing and phenotyping of cellular vesicles using nanoparticle tracking analysis," *Nanomedicine*, vol. 7, no. 6, pp. 780–788, 2011.
- [83] R. J. Hunter, "Zeta potential in colloid science: Principles and applications," *Academic Press*, 1981.
- [84] L. Reimer, Scanning Electron Microscopy: Physics of Image Formation and Microanalysis. Springer, 1998.
- [85] R. F. Egerton, *Physical Principles of Electron Microscopy: An Introduction to TEM, SEM, and AEM.* Springer, 2005.
- [86] M. I. Hussein, M. J. Leamy, and M. Ruzzene, "Dynamics of phononic materials and structures: Historical origins, recent progress, and future outlook," *Applied Mechanics Reviews*, vol. 66, p. 040 802, 2014.
- [87] T. Chen, S. Li, and H. Sun, "Metamaterials application in sensing," Sensors, 2012.
- [88] R. Guan, H. Xu, Z. Lou, Z. Zhao, and L. Wang, "Metamaterials for high-performance smart sensors," *Applied Physics Reviews*, 2024.
- [89] M. Elgeziry, F. Costa, and S. Genovesi, "Design guidelines for sensors based on spiral resonators," *Sensors*, 2022.
- [90] W. Wang, K. Sun, Y. Xue, J. Lin, et al., "A review of terahertz metamaterial sensors and their applications," *Optics Communications*, 2024.
- [91] D. Prakash and N. Gupta, "Applications of metamaterial sensors: A review," *International Journal of Microwave and Wireless Technologies*, 2022.
- [92] S. Shamim, A. S. M. Mohsin, M. M. Rahman, and M. B. H. Bhuian, "Recent advances in metamaterial and metasurface-based biosensors in the ghz, thz, and optical domains," *Heliyon*, 2024.
- [93] A. Vivek, K. Shambavi, and Z. C. Alex, "A review: Metamaterial sensors for material characterization," *Sensor Review*, 2019.
- [94] M. Naito, T. Yokoyama, K. Hosokawa, and K. Nogi, "Nanoparticle technology handbook," *Nanoparticle Technology Handbook, 3rd ed.*, 2018.
- [95] M. M. Honrubia, "Machine learning techniques to enhancethe capacitive sensing of microwaveresonant structures," Ph.D. dissertation, Universidad Pontifica Comillas ICAI.
- [96] M. Rosh Abarbanel et al., "Thermal response of cuo/polydopamine nanospheres under nir laser irradiation," *Ceramics International*, 2023.
- [97] M. Ding, "The road from mle to em to vae: A brief tutorial," AI Open, 2022.
- [98] O. S. Eyobu and D. Han, "Feature representation and data augmentation for human activity classification based on wearable imu sensor data using a deep lstm neural network," *Sensors*, 2018.
- [99] Y.-Q. Song, L. Venkataramanan, M. D. Hürlimann, M. Flaum, P. Frulla, and C. Straley, "T1–t2 correlation spectra obtained using a fast two-dimensional laplace inversion," *Journal of Magnetic Resonance*, 2002.
- [100] A. Afrough, R. Mokhtari, and K. L. Feilberg, "Simple matlab and python scripts for multi-exponential analysis," *Magnetic Resonance in Chemistry*, 2023.
- [101] L. Arnaut, "Reaction order and rate constants," Chemical Kinetics, 2021.